The Southern Hemisphere Westerlies and the Ocean Carbon Cycle:
The Influence of Climate Model Wind Biases and Human Induced Changes.

by

Neil Cameron Swart
B.Sc., University of Cape Town, 2004
B.Sc. (Hons), University of Cape Town, 2005
M.Sc., University of Cape Town, 2008

A Dissertation Submitted in Partial Fulfillment of the
Requirements for the Degree of

DOCTOR OF PHILOSOPHY

in the School of Earth and Ocean Sciences

The Southern Hemisphere Westerlies and the Ocean Carbon Cycle:
The Influence of Climate Model Wind Biases and Human Induced Changes.

by

Neil Cameron Swart
B.Sc., University of Cape Town, 2004
B.Sc. (Hons), University of Cape Town, 2005
M.Sc., University of Cape Town, 2008

Supervisory Committee

Dr. J.C. Fyfe, Co-Supervisor
(School of Earth and Ocean Sciences)

Dr. A.J. Weaver, Co-Supervisor
(School of Earth and Ocean Sciences)

Dr. J.M. Klymak, Departmental Member
(School of Earth and Ocean Sciences)

Dr. O.A. Saenko, Departmental Member
(School of Earth and Ocean Sciences)

Dr. D. Atkinson, Outside Member
(Department of Geography)

Supervisory Committee

Dr. J.C. Fyfe, Co-Supervisor
(School of Earth and Ocean Sciences)

Dr. A.J. Weaver, Co-Supervisor
(School of Earth and Ocean Sciences)

Dr. J.M. Klymak, Departmental Member
(School of Earth and Ocean Sciences)

Dr. O.A. Saenko, Departmental Member
(School of Earth and Ocean Sciences)

Dr. D. Atkinson, Outside Member
(Department of Geography)

ABSTRACT

The ocean is the largest sink of anthropogenic carbon from the atmosphere and therefore the magnitude of ocean carbon uptake largely determines the airborne fraction of emissions and the ultimate severity of surface climate change. However, climate-feedbacks on ocean carbon uptake over the historical period and in the future are uncertain. In particular, much uncertainty in the ocean carbon response hinges on the influence of wind-driven changes in the Southern Ocean, which is the most significant region of anthropogenic carbon uptake.

Here I show that the Southern Hemisphere westerly winds simulated by the Coupled Model Intercomparison Project Phase 3 (CMIP3) and CMIP5 climate models have significant biases in their pre-industrial and satellite era-climatologies, relative

to observationally based estimates. I also show that the models project the westerlies to intensify and shift poleward under anthropogenic forcing over the 20th and 21st centuries, but that they significantly underestimate the trends over the satellite era.

I then use a novel experimental design, wherein I isolate the influence of the model's pre-industrial wind bias on simulations of ocean carbon uptake and climate. I do this by using the UVic Earth System Climate Model (ESCM) with an ensemble of members, each forced by the winds from an individual CMIP model.

I show here that the climate model pre-industrial wind bias can significantly increase ocean carbon uptake in transient climate change simulations, reducing the airborne fraction and projected climate change. By contrast, the simulated wind-changes over the 20th and 21st centuries reduce ocean carbon uptake, largely through an increase in outgassing from the Southern Ocean. However, I show that this transient-wind effect is i) smaller than the pre-industrial bias effect and ii) does not occur when using a variable formulation for the Gent-McWilliams coefficient of eddy diffusivity in the coarse resolution model, under simulated or observed wind-changes.

I then go on to demonstrate that the simulated transient wind-changes significantly reduce the Antarctic sea-ice area simulated by the UVic ESCM. I also test the influence of fresh water input to the Southern Ocean from dynamic Antarctic Ice Sheet mass loss, which is a forcing absent from the CMIP5 models. The magnitude of the fresh water effect is small and has little influence on the sea-ice area trends simulated by the CMIP5 models over the historical era.

These results have significant implications for previous model-based studies of the ocean carbon cycle, as well as for the quantification of the wind-induced uncertainty in future climate projections by current Earth System Models.

Contents

List of Tables

List of Figures

ACKNOWLEDGEMENTS

I am particularly grateful to my supervisor, Dr John Fyfe, who dedicated many hours of time to discussing the research in this thesis. John's insights guided the work throughout the process, and his thoughtful feedback improved and greatly clarified much of the text. Most importantly though John taught me how to identify and focus on the core scientific message within my results, and to craft the figures to clearly communicate that message in the literature, which is an invaluable skill that I'm sure will buoy my career.

My co-supervisor, Prof. Andrew Weaver, provided me with overall guidance on my thesis, but he also encouraged me to pursue idea's outside of my narrow thesis topic, collaborated with me to produce publishable results, and then guided me through the resulting media maelstrom, for which I am sincerely thankful.

My thesis committee members, including my supervisors and Dr David Atkinson, Dr Jody Klymak and Dr Oleg Saenko provided extremely helpful guidance on constraining my thesis topic, for which I thank them. I would like to thank Dr Oleg Saenko who also provided helpful discussions and guided me in thinking about the dynamics of the Southern Ocean, and he provided me with the original implementation of the variable Gent-McWilliams diffusivity coefficient used in Chapters 5 and 6. I would also like to thank Jim Christian, Jeremy Fyke, Nathan Gillett, Robin Mathews, Bill Merryfield, John Scinocca, Michael Sigmond and Geoff Stanley for helpful comments on the manuscript drafts that comprise this thesis.

The climate lab staff made most of my endeavours possible. I thank Mike Eby for his invaluable help and guidance on using the UVic model, and for very insightful feedback on my work; Ed Wiebe kept the local computational wheels turning with his technical wizardry, and helped to secure the Westgrid resources. Wanda Lewis skillfully guided my matters through the UVic bureaucracy, and kindly shielded me through my media adventure. Many students in the climate lab and throughout the School provided help with the science, but most importantly made the graduate experience a fantastic one.

I am grateful for the financial support from the South African National Research Foundation (NRF) through a *2009 NRF Prestigious Scholarship for Doctoral Studies Abroad*; the Natural Sciences and Engineering Research Council of Canada (NSERC) for funding through the *CREATE Training Program in Interdisciplinary Climate Science at the University of Victoria* and the University of Victoria through a *Dr.*

Arne H. Lane Graduate Fellowship in Marine Sciences, a *Graduate Award* and several *Academic Income Supplements*. The ensemble simulations done in this thesis were only possible because of computing resources generously supplied by Compute-Canada/Westgrid.

My greatest debt of gratitude though belongs to my family. My parents, Allan and Joan, who have selflessly supported and encouraged me for so long and in so many ways are the ones who really got me here. My sister Michelle, and brother-in-law Mike, have been such great friends and confidants and their support has smoothed my way. Most mostly, my partner Jessica who brightens my life, and literally kept me alive during my thesis preparation, always provided support and a willing ear, and skillfully guided me to optimism during the darkest times, without who it would never have come together.

DEDICATION

To my fellow Africans, who will suffer the worst consequences of anthropogenic climate change, while bearing the least responsibility for its cause.

Chapter 1

Introduction

The major aim of this thesis is to evaluate how the global wind fields and in particular the Southern Hemisphere westerly winds influence simulated ocean carbon uptake and our ability to project future climate. There are three main branches of inquiry. The first seeks to evaluate how well modern climate models simulate the climatology and trends in the Southern Hemisphere westerly winds, and how the winds are projected to evolve under future climate change.

The second branch of enquiry seeks to quantify how biases in the models pre-industrial winds influence ocean carbon uptake and projections of future climate change. The third branch of enquiry evaluates how observed and simulated temporal changes in the winds influence the climate system, focusing on ocean carbon uptake and Antarctic sea-ice area. The aim of this chapter is to introduce my key findings and to provide an outline of the thesis.

1.1 Key results

I make *five* claims which my dissertation validates:

1. The Southern Hemisphere westerly winds simulated by the CMIP3 and CMIP5 climate models have systematic and statistically significant biases in their:
   - pre-industrial era climatologies,
   - modern satellite era climatologies, and
   - trends over the 20th century
2. Pre-industrial wind biases significantly redistribute carbon within the simulated pre-industrial ocean, introducing errors into the fields used to initialize transient climate change simulations.
3. Simulated wind changes over the 20th and 21st century have a smaller influence on ocean carbon uptake than the pre-industrial bias effect.
4. The representation of mesoscale eddies in the coarse resolution UVic ESCM significantly influences how the pre-industrial wind biases and transient wind changes affect ocean carbon uptake.
5. Fresh water forcing from recent dynamic mass loss from the Antarctic Ice Sheet significantly increases sea-ice area in simulations with the UVic ESCM, and could shift the CMIP5 sea-ice area trends to be statistically consistent with observations at the 10% significance level.

1.1.1 The significance of this research

The results of this research have direct implications for identifying and reducing the uncertainties in historical and future ocean carbon uptake. In particular

- Reducing uncertainty in observed and simulated pre-industrial winds and their time-evolution over the 20th century is key to accurately quantifying the ocean carbon sink. Indeed, constraining the terrestrial carbon sink also depends on model simulations of ocean carbon uptake [Sarmiento *et al.*, 2010] and therefore our quantification of the global carbon cycle is sensitive to uncertainties in the

wind-forcing.

- Climate models underestimate historical trends in the Southern Hemisphere westerlies and the resulting feedbacks on the ocean carbon cycle, which indicates that significant uncertainty exists in projections of future wind-changes and ocean carbon uptake. Similarly, projected changes in other components of the climate system that are sensitive to wind-forcing, like sea-ice area, are subject to the uncertainty in projected wind changes.

- Ocean-only and climate model simulations must appropriately represent mesoscale eddies to correctly estimate rates of ocean carbon uptake, and in particular the ocean response to changing wind forcing. Previous studies that neglected compensating eddy effects may have overestimated the magnitude of the feedback from historical wind changes on the Southern Ocean carbon sink.

1.2 Outline

The remainder of this thesis is laid out as follows

Chapter 2 describes in detail the ocean carbon cycle, the dynamics of the circulation in the Southern Hemisphere mid-latitude atmosphere and ocean as well as the strategy used for model simulations of historical and future climate.

Chapter 3 assesses the Southern Hemisphere westerly wind climatologies and trends over 1979 to 2010 simulated by the CMIP3 and CMIP5 climate models relative to observations, and also assesses future changes in the winds projected by the models.

Chapter 4 introduces the UVic ESCM based experimental design, and provides an estimate of the influence of the CMIP3 pre-industrial zonal wind-stress biases on ocean carbon uptake.

Chapter 5 updates the wind-bias results from Chapter 4 using the new CMIP5 models, and extends the research to consider different components of the wind, time-evolving winds, and different eddy choices for the eddy diffusivity in the Gent-McWilliams parameterization.

Chapter 6 assesses the influence of ice-sheet derived fresh water forcing on Antarctic sea-ice trends, and the implications of the fresh-water forcing for the sea-ice trends simulated by the CMIP5 models.

Chapter 7 then summarizes the key conclusions of the thesis.

Appendices provide details of the models used, and supplementary information referred to in the main text.

Chapter 2

Southern Hemisphere winds and the climate of the Earth

2.1 Climate and the carbon cycle

2.1.1 Paleoclimate and anthropogenic climate change

Mass-balance and geochemical evidence confirm that the rapid increase in atmospheric CO_2 seen since the industrial revolution is attributable to human activities and principally the combustion of fossil fuels [Keeling *et al.*, 2005; Siegenthaler and Sarmiento, 1993]. This anthropogenic carbon perturbation is already driving measurable climate change which has significant impacts on the biosphere, including human society [Solomon *et al.*, 2007]. An enormous fossil fuel resource base, with an estimated carbon content of 12,500 Gt [Rogner *et al.*, 2012], remains available to drive future climate change well beyond so called "dangerous levels" in the absence of corrective measures from society [Swart and Weaver, 2012]. How will the Earth system respond to humanity's atmospheric CO_2 perturbation?

Changes in atmospheric CO_2 and surface temperature are positively correlated on time-scales spanning several orders of magnitude from decades to hundreds of millions of years [Lüthi *et al.*, 2008; Solomon *et al.*, 2007; Royer *et al.*, 2004], but the sign of the carbon–climate feedback changes. On geological time-scales (millions of years – Ma) it is proposed that the carbon cycle acts as a negative feedback, stabilizing the climate system [Walker *et al.*, 1981], and maintaining the climatic stability necessary for the advent of life and the evolution to multicellular organisms [Archer, 2010; Sagan and Mullen, 1972].

By contrast, over the Quaternary period ice-core records reveal that atmospheric CO_2 changes act to amplify the small but regular oscillations in orbital forcing to produce the pronounced temperature fluctuations of the 100 ka glacial–interglacial cycles [Shakun *et al.*, 2012; Petit *et al.*, 1999]. The change in the sign of the carbon-climate feedback between these paleo-timescales leads to pertinent questions about how the Earth system will respond to the recent anthropogenic CO_2 perturbation [Archer, 2010].

Since the mid 20th century when careful observation began, mass-balance suggests that the ocean and terrestrial biosphere have acted as a net sink, absorbing approximately 55% of anthropogenic carbon emissions [Ballantyne *et al.*, 2012]. This uptake has acted to significantly damp the impact of the human climate perturbation.

There is however significant debate over how the efficiency of the combined land and ocean carbon sink has responded to increasing anthropogenic emissions in the

past, and how they might change in the future (where efficiency refers to the fraction of anthropogenic emissions taken up). Many coupled climate–carbon cycle models show a positive carbon–climate feedback that tends to increase the airborne fraction (A_f) of total emissions, thereby amplifying projected climate warming [Eby *et al.*, 2013; Friedlingstein *et al.*, 2006]. This conclusion is supported by some observation studies [Le Quéré *et al.*, 2009] but disputed by others which fail to find a historical trend in the A_f [Gloor *et al.*, 2010; Knorr, 2009].

Opposing trends in the efficiencies of the land and ocean sink over the historical period can explain the disagreement [Sarmiento *et al.*, 2010]. Multiple independent modelling studies find a decreasing efficiency of the ocean carbon sink, particularly in the Southern Ocean over the historical period [Le Quéré *et al.*, 2010; Le Quéré *et al.*, 2007; Lovenduski *et al.*, 2008; Wetzel *et al.*, 2005], but the future trend is debated [Zickfeld *et al.*, 2008; Le Quéré *et al.*, 2008]. This is significant because the ocean has been the principal sink, removing 30% of anthropogenic CO_2 from the atmosphere over the historical period [Khatiwala *et al.*, 2012; Sabine *et al.*, 2004], and the long-term atmospheric concentration and climate also depends principally on the rate of oceanic uptake [Eby *et al.*, 2009]. Indeed, the response of the carbon cycle is a key uncertainty in projections of future anthropogenic climate change [Friedlingstein *et al.*, 2006; Meehl *et al.*, 2007a]. A clear understanding of the processes influencing the oceanic carbon sink are thus key to accurate projections of future climate change.

2.1.2 The ocean carbon cycle

The pre-industrial ocean carbon cycle

The ocean is the largest rapidly exchanging carbon reservoir on the planet, and on millennial timescales it is the ocean which sets the atmospheric CO_2 concentration [Raven and Falkowski, 1999]. Indeed, the pre-industrial ocean held about 98.5% of the carbon in ocean-atmosphere system. When at equilibrium the ocean holds more carbon than the atmosphere because although carbon enters the ocean mainly as CO_2, it then rapidly dissociates into different chemical species, which together are known as Dissolved Inorganic Carbon (DIC) [Sarmiento and Gruber, 2006]:

$$\begin{aligned} [DIC] &= [CO_2^*] + [HCO_3^-] + [CO_3^{2-}] \\ &= \quad 0.5\% \qquad 88.6\% \qquad 10.9\% \end{aligned} \tag{2.1}$$

Carbon is distributed amongst the DIC species depending on the pH (percentages above are the distribution for the mean sea-surface properties), while the solubility of CO_2 in seawater is also strongly dependent on temperature and salinity [Sarmiento and Gruber, 2006, also note that above $CO_2^* = CO_{2\,(aq)} + H_2CO_3$].

The ocean is able to take up additional carbon from the atmosphere by redistributing DIC from the surface to the deep ocean. Observations show that DIC increases by about 15% from the surface to depth. The vertical DIC gradient is maintained by the *solubility* and the *biological* pumps. Increasing the efficiency of the ocean carbon pump increases the storage of carbon in the deep ocean, and reduces carbon storage in the surface ocean and the atmosphere [Marinov and Sarmiento, 2004]. The strength of these pumps may be affected by changes in the:

- rate of air-sea exchange (e.g. caused by increasing sea-ice cover, or wind-speed) [e.g. Stephens and Keeling, 2000].
- efficiency of the biological pump (e.g. through iron fertilization) [Marinov *et al.*, 2006]
- ocean circulation (or mixing), which redistributes nutrients and carbon [Marinov *et al.*, 2008].
- vertical stratification [Ito and Follows, 2003].

The high latitude oceans exert a disproportionate control on the strength of the carbon pumps relative to their area [Sarmiento and Gruber, 2006; Marinov *et al.*, 2006]. This is because the polar regions serve as the lid to most of the interior volume of ocean, forming the oceans "window" to the atmosphere [Sarmiento and Gruber, 2006]. Additionally inefficient high latitude biology leaves surface nutrients unutilized (so called *preformed nutrients*), the concentration of which measures strength of the biological pump [Marinov *et al.*, 2006].

The Southern Ocean (SO) was by far the most important region for setting the pre-industrial ocean-atmosphere CO_2 balance [Sigman *et al.*, 2010; Sarmiento and Gruber, 2006]. Antarctic zone waters have the highest concentration of preformed nutrients and therefore exert the greatest control over the efficiency of the biological pump [Marinov *et al.*, 2006]. The circumpolar SO also connects the three major ocean basins, which allows a global overturning circulation to exist [e.g. Rintoul *et al.*, 2001]. The Antarctic Bottom Water (AABW) formed there ventilates the single largest fraction of the ocean interior, followed by North Atlantic Deep Water

(NADW) and then Antarctic Intermediate Water (AAIW) and Subantarctic Mode Water (SAMW) [Johnson, 2008; Sloyan and Rintoul, 2001]. These water masses dominate the overturning circulation, which can be schematically represented as an upper and lower overturning cell (see Fig. 2.1).

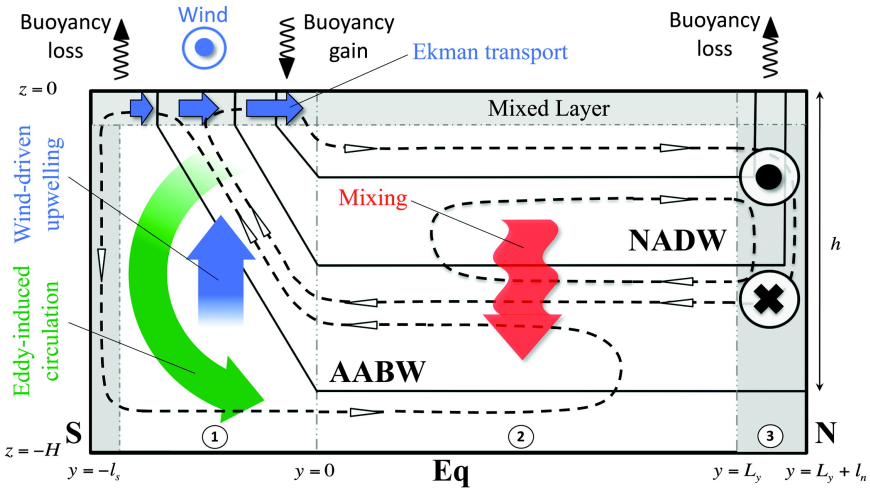

Figure 2.1: Schematic depicting the upper (NADW) and lower (AABW) cells of the MOC. Solid thick lines are isopycnals, dashed lines represent the streamlines of the residual circulation. © 2012 American Meteorological Society, From Nikurashin and Vallis [2012] Fig. 8.

The upwelling of CO_2 rich Circumpolar Deep Water around the Southern Ocean leads to a natural outgassing to the atmosphere in the region south of the Antarctic Polar Front (APF). By contrast, the formation and subduction of SAMW/AAIW driven northward by the winds leads to natural CO_2 uptake in Subantarctic region to the north of the APF [Marinov and Sarmiento, 2004]. Changes in the relative overturning rates of these two cells can influence this situation and have a significant influence on ocean carbon storage [Marinov *et al.*, 2008]. A slowdown in the lower cell, allowing for more accumulation of carbon from the biological rain, and reduced natural outgassing, may have reduced glacial atmospheric CO_2 [Sigman *et al.*, 2010; Toggweiler *et al.*, 2006]. Future changes in these overturning cells, driven by changing winds may also influence the uptake of anthropogenic carbon [Russell *et al.*, 2006b].

Ocean uptake of anthropogenic carbon

The ocean will not absorb 98.5% of the anthropogenic atmospheric carbon perturbation, and therefore the airborne fraction will not remain 1.5%, in keeping with the

pre-industrial equilibrium distribution. Rather the remaining airborne fraction will vary from 7–40%, depending on the timescales and processes involved [Archer *et al.*, 2009; Archer, 2005]. After several thousand years when the mixing of anthropogenic carbon to depth is complete, the airborne fraction will still be between 16 and 40% (depending on the perturbation size) [Archer *et al.*, 2009; Eby *et al.*, 2009]. This decrease in the relative fraction of total carbon stored by the ocean is dictated by changes in the chemical buffering which shift the relative distribution of the DIC constituents towards CO_2, reducing total oceanic uptake [Sarmiento and Gruber, 2006]. On longer timescales between 10 and 100 ka, carbonate and silicate weathering will increase oceanic uptake and further reduce the airborne fraction [Archer, 2005], but these scales are beyond our interest here.

The immediate invasion of CO_2 into the ocean is controlled by surface gas exchange and the rate of ocean ventilation, which can be approximated by a sum of exponential functions (see Section 2.2.2 for a simple example). The ventilation e-folding times increase from 1 year for the mixed layer, 10 years for the thermocline, 60 years for intermediate water to 350+ years for the overturning of the deep ocean [Marinov and Sarmiento, 2004]. On the timescales of immediate human interest, ocean carbon uptake, the atmospheric airborne fraction and the amount of climate change are determined by the processes which ventilate the intermediate and deep ocean.

The Southern Ocean dominates the uptake of anthropogenic CO_2 [Khatiwala *et al.*, 2012; Gruber *et al.*, 2009]. The ventilation of AAIW/SAMW draws anthropogenic CO_2 from the atmosphere through the air-sea interface in the Subantarctic, after which the waters subduct along isopycnals and move north, leading to carbon storage in the subtropical gyres [Khatiwala *et al.*, 2012; Gruber *et al.*, 2009]. The North Atlantic Deep Water formation region is the next most significant sink, and the only region where deep injection of anthropogenic CO_2 occurs [Sabine *et al.*, 2004]. A variety of other thermocline waters in the Pacific and Indian Ocean also sequester anthropogenic CO_2 [Gruber *et al.*, 2009]. Climate change can affect the ability of the ocean to sequester anthropogenic CO_2.

Climate feedbacks on ocean carbon uptake

Changes in climate feedback on the ability of the ocean to sequester carbon, with positive feedbacks decreasing ocean carbon uptake and increasing atmospheric CO_2. Namely, changes in chemical buffering decrease uptake, ocean warming decreases CO_2

solubility and ocean biology is sensitive to changes in various ways which are poorly understood [Marinov and Sarmiento, 2004].

Further feedbacks result from climate induced changes to the physical ocean circulation, mixing and stratification. Over the recent decades the Southern Ocean has had a near zero net CO_2 flux, the result of the large ingassing of anthropogenic CO_2 compensating the large natural outgassing. The net oceanic uptake is sensitive to potential climate feedbacks which alter the large compensating Southern Ocean fluxes [Gruber *et al.*, 2009]. It is proposed that a saturation of the Southern Ocean carbon sink has been caused by increasing westerly winds that speed up the overturning circulation, leading to an increased outgassing of natural CO_2, yet leaving anthropogenic CO_2 uptake relatively unchanged [Lovenduski *et al.*, 2008; Le Quéré *et al.*, 2010; Le Quéré *et al.*, 2007]. To understand this connection requires a fuller understanding of the dynamics governing the Southern Ocean and the global ocean circulation.

2.1.3 Dynamics of the oceanic overturning circulation

The ocean interior

The steady-state Transformed Eulerian Mean (TEM) form of the momentum and buoyancy equations (see Appendix A.1 for a derivation; here I follow Vallis [2006] and Nikurashin and Vallis [2011]) can be written as

$$-fv^\dagger = -\frac{\Delta p}{L_x} + \overline{v'q'} + \frac{\partial \overline{\tau}}{\partial z} \tag{2.2}$$

$$v^\dagger \partial_y \overline{b} + w^\dagger \partial_z \overline{b} = \overline{S} \tag{2.3}$$

where $\overline{b}$ is the Eulerian zonal mean buoyancy ($b = -g(\rho - \rho_0)/\rho_0$ where ρ is density, and g is the gravitational acceleration); $v^\dagger$ and $w^\dagger$ are residual velocities and f is the Coriolis frequency. The eddy terms have been collected together in the momentum equation, and are given by the potential vorticity flux $\overline{v'q'}$, where eddies are defined as a deviation from the Eulerian zonal mean. Also Δp is the zonal pressure difference across the basin of width L_x (unspecified here); $\overline{\tau}$ denotes frictional stress, and $\overline{S}$ is a buoyancy source (diabatic term).

Over most of the global ocean, governed by Sverdrup dynamics, the steady state motion is governed by a frictional-geostrophic balance, and the eddy terms are of

second order. Here the influence of the winds is restricted to the upper several hundred meters [Vallis, 2006]. The presence of stratification and circulation below these levels must be maintained by different processes.

Removal of buoyancy at high latitudes (e.g. North Atlantic) causes convection and deep water formation. The return of these heavy deep waters to the surface requires mechanical energy, the source of which is still debated [Kuhlbrodt *et al.*, 2007]. Classically, turbulent mixing is invoked to mix heat downwards [diabatic heating, representing by $\overline{S}$ in (2.3)], which reduces the density of deep waters and allows them to rise under buoyancy forcing [Stommel, 1958; Munk, 1966; Munk and Wunsch, 1998]. This is expressed from the steady form of (2.3) as the advective diffusive balance over the ocean basin

$$\frac{\partial \overline{b}}{\partial z} w = \kappa_v \frac{\partial^2 \overline{b}}{\partial z^2} \tag{2.4}$$

The upwelling of deep waters is driven by turbulent mixing, here shown as the constant diffusivity κ_v and through continuity the upwelling drives a meridional velocity in the abyssal ocean [Stommel, 1958; Stommel and Arons, 1960]. Yet the level of mixing observed appears to be an order of magnitude too low to drive the meridional overturning circulation, at least in the interior away from topography [Kuhlbrodt *et al.*, 2007]. The emerging picture of the circulation is of a deep water return path through the Southern Ocean, governed by winds and eddies [Marshall and Speer, 2012].

Dynamics of a circumpolar channel

The eddy terms in equation (2.2) play a leading order role in the dynamical balances of the Southern Hemisphere mid-latitude ocean and atmosphere. The eddy effects, collected under the potential vorticity flux ($\overline{v'q'}$), are given by the divergence of the Eliassen-Palm vector:

$$\overline{v'q'} = -\frac{\partial}{\partial y}\left(\overline{u'v'}\right) + f\frac{\partial}{\partial z}\left(\frac{\overline{v'b'}}{\partial_z \overline{b}}\right) \tag{2.5}$$

where $\overline{u'v'}$ and $\overline{v'b'}$ are the meridional eddy momentum and buoyancy flux respectively. In the Southern Ocean, scaling arguments can be used to show that the potential vorticity flux, (2.5), is governed by the buoyancy term [Vallis, 2006], so the eddy momentum flux can be neglected. Additionally, in the circumpolar latitudes of Drake Passage the pressure term, Δp, in (2.2) must disappear at levels above the ridges. Substituting in the eddy buoyancy flux from (2.5) and removing the pressure term

we can thus re-write (2.2) as

$$f v^\dagger = -\frac{\partial \overline{\tau}}{\partial z} - f \frac{\partial}{\partial z}\left(\frac{\overline{v'b'}}{\partial_z \overline{b}}\right) \tag{2.6}$$

The absence of the pressure term here means that the meridional flow is purely ageostrophic. This feature makes the dynamics of the the circumpolar channel unique in the ocean. It allows the influence of the winds to penetrate the interior and drive a deep upwelling in a process known as the Drake passage effect [Toggweiler and Samuels, 1995]. Similarly, in the absence of meridional geostrophic flows, buoyancy losses south of the channel can only be balanced by an eddy-induced transport [De Szoeke and Levine, 1981]. Aspects of the channel circulation have been described theoretically in the TEM framework by Nikurashin and Vallis [2012]; Marshall and Radko [2003]; Johnson and Bryden [1989].

The residual velocities can be expressed as a streamfunction

$$(v^\dagger, w^\dagger) = \left(-\frac{\partial \overline{\Psi}^\dagger}{\partial z}, \frac{\partial \overline{\Psi}^\dagger}{\partial y}\right) \tag{2.7}$$

In the TEM framework, we solve for the residual circulation, which is the sum of the Eulerian mean and eddy induced circulations

$$\Psi^\dagger = \overline{\Psi} + \Psi^* \tag{2.8}$$

Now if we assume that the interior flow is adiabatic, the eddies may be parameterized following Gent and McWilliams [1990] as

$$\overline{v'b'} = -K_{\text{GM}} \partial_y \overline{b} \tag{2.9}$$

where K_{GM} is an eddy diffusivity. The eddy-induced streamfunction is now given by

$$\Psi^* = \frac{\overline{v'b'}}{\partial_z \overline{b}} = -K_{\text{GM}} \frac{\partial_y \overline{b}}{\partial_z \overline{b}} = K_{\text{GM}}\, S_b \tag{2.10}$$

where S_b is the mean slope of buoyancy surfaces (i.e. isopycnals). There are various choices for the exact form of K_{GM}, which affect the circulation as will be discussed more in Chapter 5.

Using (2.8) and (2.10) equation (2.6) can be integrated from below the base of the

mixed layer where the stress τ is assumed to vanish, to the ocean surface where τ is equal to the zonal surface wind stress τ_x, to obtain

$$\Psi^\dagger = -\frac{\tau_x}{f} + K_{\rm GM}\, S_b \tag{2.11}$$

This is a statement that the residual overturning circulation in the channel is the sum of the Eulerian mean circulation driven by the wind-stress, and the eddy induced circulation. Physically, the westerly winds drive a northward Ekman transport at the surface which drives a deep upwelling and tends to incline the isopycnals, and form a meridional buoyancy gradient (or front). The eddies work to release the potential energy stored in the front, and return the isopycnals to the horizontal [Marshall and Radko, 2003].

Sometimes the compensation between the wind and eddy driven circulations is assumed to be nearly complete, leaving a near zero residual overturning circulation. But for our choice of eddy parameterization, and typical parameter values for the Southern Ocean, the Eulerian mean circulation greatly exceeds the eddy-induced circulation, leaving a significant net residual overturning circulation [Nikurashin and Vallis, 2012], which is in good agreement with high resolution models and the observed density structure [Wolfe and Cessi, 2010].

From the perspective of the momentum budget, the westerly winds deposit momentum at the ocean surface through the wind-stress. The eddy buoyancy term transfers the momentum downward through the water column through interfacial form-stress to the ocean bottom where it can be dissipated by bottom form drag [Johnson and Bryden, 1989; Vallis, 2006].

The upper limb of the overturning circulation

Gnanadesikan [1999] and Nikurashin and Vallis [2012] developed scaling theories for the upper limb of the overturning circulation [the NADW cell in Fig. 2.1], where northern deep-water formation is balanced by diffusion through the thermocline (2.4) in the ocean basin and wind-driven upwelling in the Southern Ocean channel (2.11). The observed low rates of diffusivity over the mid-depth ocean suggest that deep-water formed in the north is upwelled almost exclusively in the Southern Ocean. In the limit of weak-diffusivity, the strength of the circulation is essentially determined by the wind-driven Ekman transport in the Southern Ocean, to which the rest of the ocean is forced to adjust [Nikurashin and Vallis, 2012; Gnanadesikan and Hallberg, 2000].

The winds together with buoyancy fluxes produce light waters (SAMW/AAIW) which ventilate the thermocline. Stronger winds form more thermocline waters, deepening the thermocline.

In the north, the depth of the thermocline is proportional to the pressure difference between the low and high latitude ocean. The pressure difference drives a northward frictional flow on the western ocean boundary, and it is commonly assumed that this northward flow is equal to the volume flux of northern deep water formation [Gnanadesikan, 1999]. Thus, deep-water formation in the north is often represented as proportional to the thermocline depth, is thus forced to adjust to the southern wind-driving. Northern deep-water formation is of course dependent on the local surface buoyancy forcing, and its true form is more complicated than implied here. Nonetheless, in the limit of weak diffusivity, the southern winds and eddies largely determine the strength of the circulation, consistent with eddy resolving simulations [Wolfe and Cessi, 2010; Hallberg and Gnanadesikan, 2006].

The lower limb of the overturning circulation

Ito and Marshall [2008] and Nikurashin and Vallis [2011] describe similar scaling theories for the lower limb of the overturning circulation, which is in general less well studied [the AABW cell in Fig. 2.1]. Antarctic Bottom Waters lie directly above the rough ocean bottom where turbulent mixing is elevated, and as such diapycnal mixing cannot be neglected. In the scaling of Nikurashin and Vallis [2011], the isopycnal slope in the channel and stratification throughout the deep ocean basin are set in the channel by the balance between the winds and eddies, consistent with eddy resolving simulations [Wolfe and Cessi, 2010]. The overturning circulation meanwhile scales proportionally to the diapycnal diffusivity, κ_v, in the basin north of the channel, but varies inversely with the wind-stress, in the limit of low diffusivity or high winds [Nikurashin and Vallis, 2011]. Alternatively, if the diffusivity in the basin is at least partly determined by the Southern Ocean winds (i.e. through internal waves, generated by eddies on rough topography that propagate into the basin and break) the strength of the lower-limb of the circulation could still be directly proportional to the strength of the winds [Stanley and Saenko, 2013; Nikurashin *et al.*, 2013], which we now explore.

2.1.4 Dynamics of the westerly winds

The mid-latitude atmospheric circulation is dominated by the westerlies, which drive the ocean circulation and are the focus of this study. In particular we are interested in what processes dictate that westerly winds should occur at the surface at all, and how these may change over time. The TEM form of the momentum equation applies here too [Vallis, 2006]. Integrating (2.2) from the surface to the top of the atmosphere where frictional and buoyancy fluxes are zero (and noting that the pressure term Δp, is zero in the atmosphere) gives:

$$\tau_x = \int \overline{v'q'}\, \partial z + f \frac{\overline{v'b'}(0)}{\partial_z \bar{b}} \tag{2.12}$$

where the (0) indicates the surface [Vallis, 2006]. We can now see that the surface wind-stress is determined by vertically integrated potential vorticity fluxes and surface buoyancy fluxes. As before the potential vorticity flux is given by the divergence of the Eliassen-Palm vector, but in the atmosphere we cannot neglect the eddy momentum fluxes, so we have

$$\overline{v'q'} = -\frac{\partial}{\partial y}\left(\overline{u'v'}\right) + f\frac{\partial}{\partial z}\left(\frac{\overline{v'b'}}{\partial_z \bar{b}}\right) \tag{2.13}$$

We can interpret the first term on the right of (2.13) as the convergence of momentum related to the meridional propagation of Rossby waves initiated by baroclinic instability, while the second term relates to the meridional transport of buoyancy. The westerly winds are driven by the convergence of eastward momentum in the mid-latitudes, which is achieved through the eddy momentum fluxes. The buoyancy term works to extract momentum from aloft, and transfer it downwards to the surface, where it can be balanced by the surface wind-stress τ_x.

These dynamics describe the so-called eddy driven jet, and it occurs at latitudes that are a net source of eddies (sources - sinks > 0) [Kidston *et al.*, 2010b]. The eddies themselves are produced by large-scale baroclinic instability, which converts the available potential energy associated with the meridional temperature gradient into eddy kinetic energy [Kidston *et al.*, 2010b; Vallis, 2006]. The upper level-winds are to a good approximation in thermal-wind balance, which is to say the westerly winds increase with height, in proportion to the meridional temperature gradient along isobaric surfaces [Gill, 1982].

2.1.5 Synthesis of the SH ocean-atmosphere dynamics

The atmosphere-ocean system of the Southern Hemisphere mid-latitudes that we have described displays a beautiful and unique symmetry. The westerly winds are driven by the large-scale meridional temperature structure and the convergence of eastward eddy momentum. Eddy buoyancy fluxes transfer momentum downwards from the jet-stream aloft to the ocean surface where it is taken up by the surface stress. Similar eddy dynamics in the ocean transfer the momentum downwards to the ocean floor where it can be dissipated by form drag.

This eddy-driven momentum flux from the top of the atmosphere to the bottom of the ocean, together with the Eulerian mean flow, is also associated with the residual meridional overturning circulation. In the atmosphere, this is the Ferrel cell, with a poleward (frictional Ekman) flow at the surface. The corresponding wind-driven Ekman flow in the surface ocean has the same mass flux, but opposite direction [Gill, 1982, pp. 326–327]. The northward Ekman flow in the ocean drives a deep overturning in the circumpolar latitudes known as the Deacon cell, which effectively set the stratification and circulation of the global ocean interior [Nikurashin and Vallis, 2012; Wolfe and Cessi, 2010]. In this way, the westerly winds and the ocean circulation are intricately connected in the circumpolar latitudes of Drake Passage.

Any processes which alter the character of upper-tropospheric eddies will have an influence of the surface westerly wind jet (see Appendix A.2 for a discussion). As we shall see in Chapter 3, the position and strength of the Southern Hemisphere surface westerly wind jet is

1. Poorly simulated by global climate models
2. Undergoing significant changes in response to anthropogenic climate forcing

The poor simulation of the westerlies by climate models, and the response of the westerlies to anthropogenic forcing both have significant implications for the ocean circulation, and therefore the oceanic uptake of carbon.

2.2 Climate modelling and projection

2.2.1 The spectrum of climate models

Climate models are mathematical formulations of the major processes governing the climate system, and they can used to study the climate of the past and the future

[McAvaney *et al.*, 2001]. A spectrum of models with varying degrees of complexity have been designed for different purposes and are utilized to address specific research questions [Eby *et al.*, 2013]. For the simulation of climate change induced by anthropogenic carbon emissions, the representation of the carbon cycle in models is important in order to capture the influence of carbon–climate feedbacks, but many models lack this ability. Some commonly used models are described below.

Atmosphere-Ocean GCMs (AOGCMs) couple General Circulation Models (GCMs) of the atmosphere and ocean with sea-ice and land-surface models. However, some conditions still need to be imposed, such as the solar-constant and the composition of the atmosphere, which is specified rather than computed (i.e. they do not represent the carbon cycle). The Coupled Model Intercomparison (CMIP) Phase 3 models used in the Intergovernmental Panel on Climate Change (IPCC) fourth assessment report (AR4) fall in this category [Meehl *et al.*, 2007b].

Earth System Models (ESMs) are AOGCMs that include a representation of the carbon cycle (and potentially other geochemical constituents like nitrogen or ozone), within their subcomponents. Thus, ESMs are able to simulate the flow of carbon through the Earth System, and are therefore able to simulate the coupled evolution of the carbon–climate system. If anthropogenic emissions are specified, ESMs can project future changes in atmospheric carbon concentration (and climate) by simulating the response of the carbon cycle. Many of the CMIP5 models being used for the IPCC AR5 fall into this category [Taylor *et al.*, 2011].

ESMs of Intermediate Complexity (EMICs) are ESMs which have a reduced complexity in one or more sub-component. EMICs are usually faster to integrate because of their reduced complexity, and thus are suited to model development, and addressing questions which require long integrations or large ensembles [Eby *et al.*, 2013].

The increasing complexity of models, from the AOGCMs used in CMIP3 to the ESMs used in CMIP5, has important consequences. The increased model complexity, and specifically for our purposes the inclusion of a carbon cycle in the CMIP5 ESMs, means that the models are more realistic representations of the Earth System, and are able to quantify carbon-climate feedbacks. However, despite better representing

the system, the increased model complexity can lead to greater spread among models in the ensemble, leading to greater uncertainty in climate change projections [Knutti and Sedláček, 2012; Trenberth, 2010].

It is a key research priority to identify sources of uncertainty in these climate projections, especially in cases where systematic biases exist across the model ensemble. Identifying systematic wind biases in the model ensembles (Chapter 3), and quantifying their influence on the simulated carbon cycle (Chapters 4 and 5) and sea-ice (Chapter 6) is the objective in this thesis. To understand the wind-induced uncertainties in ESM carbon cycle modelling requires an explanation of how the models are initialized and the strategy used to make projections about the future climate.

2.2.2 Modelling strategy and initial condition bias

To illustrate the general strategy used to make projections of future climate we can consider a simple model of the ocean–atmosphere system consisting of two well-mixed boxes. The model is too simple to make useful predictions for the real ocean, but it provides insights into some of the basic assumptions in Earth System Modelling.

In this simplified system the airborne fraction of emissions, A_f, which drives climate change is simply one minus the fraction of emissions taken up by the ocean ($A_f = 1 - O_f$). The concentration of anthropogenic carbon in the ocean, C_{ant} (mol kg^{-1}), increases in time due to uptake according to:

$$\frac{\partial C_{\text{ant}}}{\partial t} = \frac{k_o k_g}{h} \left(\Delta pCO_2^a(t) - \Delta pCO_2^o(t) \right) \tag{2.14}$$

where k_o is the solubility of CO_2 (mol kg^{-1} atm^{-1}), k_g is the piston velocity (m s^{-1}), h is the depth of our ocean (m) and ΔpCO_2 are the anthropogenic perturbations to the atmospheric and oceanic partial pressures of CO_2 (atm), denoted by the superscripts a and o respectively [Sarmiento and Gruber, 2006]. The oceanic partial pressure perturbation is related to $C_{\text{ant}}(t)$ by

$$\Delta pCO_2^o(t) = \frac{\alpha R_B}{k_o} C_{\text{ant}}(t) \tag{2.15}$$

where

$$R_B = \frac{\partial pCO_2^o}{\partial DIC} \cdot \frac{DIC}{pCO_2^o} = 15 \tag{2.16}$$

is the dimensionless Revelle buffer factor (here assigned a value appropriate to the

high latitude ocean [Archer, 2005]), and α is the dimensionless ionization fraction given by [Follows and Williams, 2004]:

$$\alpha = \frac{k_o \, pCO_2^o}{DIC} = 0.005 \tag{2.17}$$

Now consider a simplified form of anthropogenic emissions that occur as a instantaneous pulse of S_0 moles of carbon occurring at time $t = 0$. Then the solution to (2.14) is given by

$$C_{\text{ant}}(t) = \frac{S_0 \cdot O_f}{\rho V} \left(1 - \mathrm{e}^{-t/\tau}\right) \tag{2.18}$$

where ρ is the density and V is the ocean volume ($m^o = \rho V$ is the total ocean mass) and τ is a characteristic time-scale of the ocean response, which depends on the total ocean depth, the gas-transfer coefficient, k_g, the CO_2 solubility, k_o, and the buffer factor, R_B (see Appendix A.3.1 for a full derivation of the solution). The fraction of total emissions taken up by the ocean at equilibrium, O_f, is given by

$$O_f = \frac{C_{eq}^o \cdot \dfrac{m^o}{R_B}}{C_{eq}^o \cdot \dfrac{m^o}{R_B} + M \cdot CO_{2(eq)}^a} = \frac{I_{OB}}{I_{OB} + I_A} \tag{2.19}$$

where C_{eq}^o is the pre-industrial DIC concentration, $CO_{2(eq)}^a$ is the pre-industrial atmospheric mixing ratio and M is the number of moles in the atmosphere. The anthropogenic emissions, S_0, partition themselves between the atmosphere and ocean according to the relative sizes of the pre-industrial reservoirs [Archer, 2005]. In the ocean the relevant reservoir is the buffered ocean carbon inventory, I_{OB}, and in the atmosphere it is the total atmospheric carbon inventory, I_A.

The key point is that the transient uptake of anthropogenic carbon in fact depends on the initial ocean DIC concentration, C_{eq}^o. This fact is a key feature of the mechanisms controlling ocean carbon uptake described is this thesis. In our simple model, this arises as a solubility constraint, but in the real ocean, circulation and biology also play important roles and their full representation requires an Earth System Model, which I adopt in Chapter 4. The potential role of the winds is evident, even from this simple model, because wind-speeds modulate the gas-transfer coefficient, k_g, but also indirectly control the solubility, k_o, through their influence on ocean temperature [Sarmiento and Gruber, 2006].

A further fundamental insight can be gained from the analytical model discussed

here, despite its simplicity. Because the oceanic uptake response depends on the initial ocean carbon concentration, the key question becomes how is the initial concentration set? Modellers exploit the fact that pre-industrial pCO_2^a is well known from ice-core records, which show long-term roughly stable conditions over the Holocene. Then, one can derive an equation for equilibrium ocean carbon storage analogous to (2.14), and specifying a given (equilibrium) level of $pCO^a_{2(eq)}$ (see Appendix A.3.2), the solution becomes:

$$C^o_{eq} = \frac{k_o}{\alpha} pCO^a_{2(eq)} \tag{2.20}$$

Now we can see that equilibrium ocean carbon concentrations are set only by the specified atmospheric boundary condition, $pCO^a_{2(eq)}$ and the model parameters α and k_o. Practically, Earth System models are integrated for a long spin-up period under specified $pCO^a_{2(eq)}$ in order to provide the model's simulated preanthropogenic "equilibrium" ocean carbon concentration. This pre-industrial equilibrium concentration, C^o_{eq}, can then be used to initialize (2.14) and to simulate the evolution of C_{ant} to historical changes and future scenarios of anthropogenic emissions. Summarizing, the two key insights into Earth System modelling provided by these simple considerations are:

1. The transient ocean carbon uptake resulting from anthropogenic emissions depends on the initial DIC concentration.

2. The initial (or pre-industrial) ocean DIC concentration is determined by the specified pre-industrial atmospheric CO_2 mixing ratio and internal model dynamics.

Here the parameters α and k_o were chosen. Different models, with different choices would lead to different equilibrium solutions (2.20). Imagine the situation where our model used a biased parameter, α, to find the pre-industrial equilibrium C^o_{eq}; but then in our use of (2.14) to simulate historical and future changes we use the correct, unbiased value. Our historical simulation and future projection would be biased by the use of a flawed model to determine the pre-industrial equilibrium. Effectively, this occurs because the model bias is changing the amount of carbon in the pre-industrial atmosphere–ocean system (see Appendix A.3.3). An underappreciated point in Earth System Modelling is indeed that the amount of carbon in the pre-industrial atmosphere-ocean system differs amongst models precisely though this mechanism. Additionally, α and especially R_B are not constants, but change in

response to climate forcing, affecting the time-dependent solutions [Sarmiento and Gruber, 2006].

In the real world and complex ESMs, ocean carbon concentrations depend on the climate and ocean circulation. As we have seen, these properties are closely connected to the Southern Hemisphere winds. The preceding framework allows me to outline of the problem that I tackle in this thesis. Specifically

1. Errors in the pre-industrial winds introduce a bias into the ocean carbon initial conditions used for transient climate simulations.

2. Biased initial conditions influence the magnitude of simulated ocean carbon uptake.

3. Time-evolving winds also influence the magnitude of simulated ocean carbon uptake and this transient wind effect can be estimated and compared to the magnitude of the pre-industrial bias effect in (2).

2.3 Chapter summary and key questions

The previous sections of this chapter have built up the components of the major problem addressed in this thesis, and I summarize them here.

1. The future climate depends on the level of anthropogenic emissions, and how the coupled carbon–climate system responds to those emissions.

2. The ocean is the principal sink of anthropogenic carbon, reducing the airborne fraction of emissions by around 30%.

3. The ocean carbon uptake on decadal to centennial scales depends heavily on the ocean overturning circulation. The latter is strongly connected to the Southern Hemisphere westerly winds through the dynamics of the Southern Ocean.

4. Simulated ocean carbon uptake is sensitive to both errors in the equilibrium or pre-industrial wind forcing and transient shifts in the forcing.

I now draw these points together to formulate the key questions I pose in this study

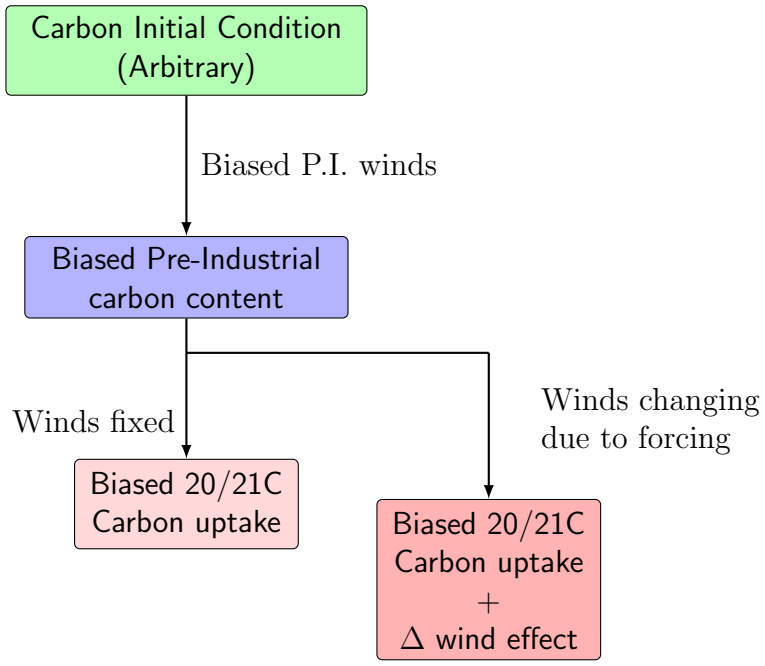

Figure 2.2: Taxonomy of the thesis problem

Key Questions:

1. Do climate models simulate the Southern Hemisphere westerly winds correctly?
2. How have the SH westerlies changed historically, in models and observations, and how are they projected to change in the future?
3. How do biases in model pre-industrial winds influence simulated ocean carbon uptake over the 20th and 21st century?
4. What effect do forced, transient changes in the winds have on the climate system, including ocean carbon uptake?
5. How does the parameterized representation of mesoscale ocean eddies influence the ocean carbon cycles response to these wind perturbations?

Chapter 3

Observed and simulated changes in the Southern Hemisphere surface westerly wind-stress

This chapter is based on the contents of the paper:

N. C. Swart and J. C. Fyfe [Aug. 2012a], Observed and simulated changes in the Southern Hemisphere surface westerly wind-stress, *Geophys. Res. Lett.*, **39,** DOI: 10.1029/2012GL052810

3.1 Introduction

The latitudinal position and the strength of the Southern Hemisphere (SH) surface westerly winds influence the rate of the oceanic meridional overturning circulation. They do so by controlling the Indo-Atlantic salt flux via the Agulhas Leakage [Beal *et al.*, 2011], and by governing the rate of deep upwelling in the Southern Ocean [Marshall and Speer, 2012]. This connection between the winds and oceanic overturning modulates the global carbon cycle [Ito *et al.*, 2010], making accurate knowledge of changes in the winds vital to understanding the fate of anthropogenic carbon [Le Quéré *et al.*, 2007]. Similarly, in climate models, correct simulation of the winds and their time-evolution under anthropogenic forcing is key to robust projections of future climate change [Swart and Fyfe, 2012b; Zickfeld *et al.*, 2007; Russell *et al.*, 2006b].

Observations and reanalyses show a positive trend in the Southern Annular Mode (SAM), the principal mode of atmospheric variability in the Southern Hemisphere (Fig. 3.1a; Marshall [2003]). It is often asserted that a poleward shift and strengthening of the SH surface westerly wind jet are synonymous with the positive trend in the SAM. However, while the strength of the jet appears to have increased robustly in the reanalyses (Fig. 3.1c), its annual mean position has not obviously experienced a poleward shift since 1979 (Fig. 3.1b). Prior to the start of the satellite era in 1979, the position of the jet varied significantly among the available reanalyses, with the large trends in the NCEP-NCAR Renanalysis 1 SAM index over the 1949-1978 period known to be spurious [Marshall, 2003].

In the Coupled Model Intercomparison Project (CMIP) phase 3 climate models, the magnitude of the change in westerly wind jet position in time has been shown to depend on the climatological jet position over the 20th century [Kidston and Gerber, 2010]. The 20th century westerlies simulated by the CMIP3 models are on average weaker and equatorward biased in position relative to observations [Fyfe and Saenko, 2006; Russell *et al.*, 2006a]. A validation of the climatology and trends in the SH westerlies as simulated by the new CMIP5 models is thus a priority for understanding the ocean circulation and carbon cycle dynamics in the CMIP5 results.

I use four reanalyses over the historical period from 1979 to 2010 to produce an observationally-based estimate of the climatology and trends in the SH surface westerly wind-stress jet. I then use this reanalysis based estimate to validate the jet climatology and trends simulated by the CMIP3 and CMIP5 climate models over the historical period, and finally I consider the response of the climate model winds to

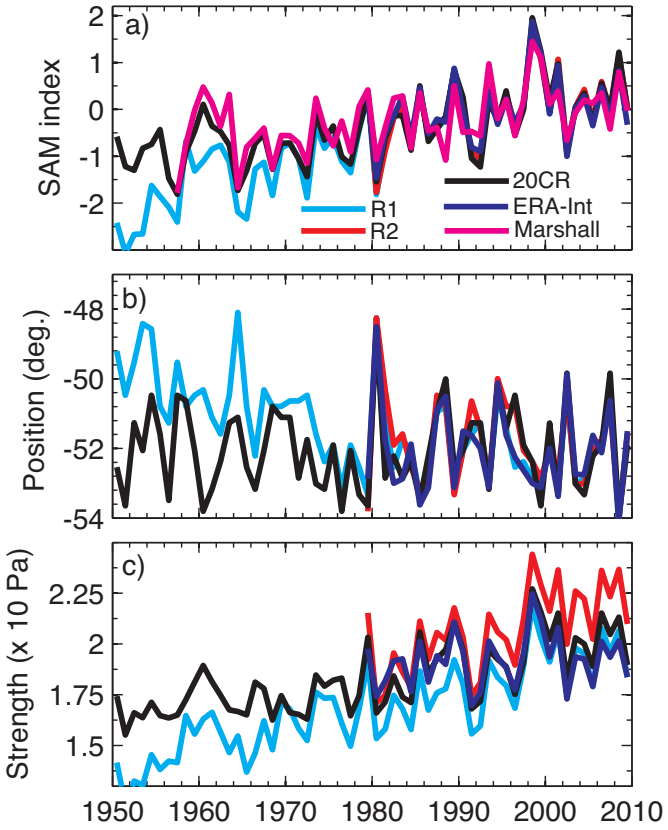

Figure 3.1: Historical changes in the annual mean Southern Annular Mode index, a) and in the SH surface westerlies latitudinal position, b) and strength, c) of the zonal-mean zonal wind-stress. Changes are shown for four reanalysis products, and in a) for updated observations from Marshall [2003].

future scenarios of anthropogenic forcing.

3.2 Data and Methods

3.2.1 Observations and reanalyses

I use the mean sea-level pressure (MSLP) and the surface zonal wind-stress from the four reanalysis products: NCEP-NCAR Reanalysis 1 (R1) [Kalnay *et al.*, 1996], NCEP-DOE Reanalysis 2 (R2) [Kanamitsu *et al.*, 2002] , ECMWF ERA-Interim Reanalysis (ERA-Interim) [Dee *et al.*, 2011] and NOAA-CIRES Twentieth Century Reanalysis Version 2 (20CR) [Compo *et al.*, 2011]. The NASA MERRA and NCEP CFSR reanalyses have not been included because these two products show significant disagreement with the other reanalyses in their strength trends (see Appendix A.4). In addition I use the Southern Annular Mode index updated online from Marshall [2003], an empirical measure based on zonal means of discrete station data.

For the reanalyses the Southern Annular Mode index was computed from the MSLP fields, as per Marshall [2003] as: SAM $= \mathrm{P}^*_{40^\circ\mathrm{S}} - \mathrm{P}^*_{65^\circ\mathrm{S}}$. Here $\mathrm{P}^*_{40^\circ\mathrm{S}}$ and $\mathrm{P}^*_{65^\circ\mathrm{S}}$ are the normalized monthly zonal MSLP at 40°S and 65°S, respectively. I use 1979 to 2010 as the averaging period in the normalization of the reanalyses SAM index. In the updated Marshall [2003] data I renormalize to the same period by subtracting the 1979 to 2010 mean.

3.2.2 Climate model data

I use the surface zonal wind-stress fields for the 20th century simulation of 23 CMIP3 models and for the historical simulations of 21 CMIP5 models (see Table A.1). Where multiple realizations exist for an individual model, I use only the first. To enable comparison with reanalysis data up until present day, the CMIP3 20th century simulations were extended from 2001 to 2010 using the SRES A1B simulations. The CMIP5 historical simulations were extended from 2005 to 2010 using the RCP4.5 simulations. The SRES and RCP scenarios are similar over this short extension period, and therefore the choice of scenario will not affect my results.

In considering simulated changes in the winds over the 1979–2100 period, the available subset of the above CMIP5 models wind-stress fields was used: 15 models for RCP2.6, 19 models for RCP4.5, 12 models for RCP6.0, 17 models for RCP8.5. The

available subset of CMIP3 models over the 1979–2100 period: 18 models for SRES A2 and 23 models for SRES A1B. For the comparison of the response of the jet to CO_2 forcing, the available subset for the 1% per year increase in CO_2 experiments to doubling, including 21 CMIP3 models and 17 CMIP5 models was used. The climate model data were made available through the World Climate Research Programme's (WCRP's) CMIP3 and CMIP5 multi-model datasets.

3.2.3 Definitions and trend calculations

For all calculations, the climate model and reanalysis wind-stress data was first interpolated onto a common 0.5-by-0.5 degree horizontal grid and to a common monthly no-leap-year calendar in time. For all time-series analyses the latitudinal position of the SH westerly wind-jet was defined as a search for the latitude of the maximum in the zonal-mean zonal surface wind-stress between 70° and 20°S. The strength of the jet was defined as the stress at this position. Where indicated I present results for the ensemble mean of the reanalyses, CMIP3 and CMIP5 models. In these cases, I have determined the latitudinal position and maximum strength of the SH surface westerly wind-stress in each reanalysis product and individual model, and then computed the ensemble mean as the average over the appropriate number of reanalyses or models. Temporal trends in position and strength were computed using a linear least squares fit to the ensemble mean data, which has been monthly, seasonally or annually averaged. The confidence interval of the trends are based on the variance of the ensemble mean, and account for auto-correlation following Santer *et al.* [2000].

3.3 Results

3.3.1 Climatological postion and strength

Over the historical period from 1979 to 2010 the reanalyses show agreement on the latitudinal position of the zonal wind-stress maximum, with a zonal-mean position near 52°S (Fig. 3.2a). Both the CMIP3 and CMIP5 models have a climatological zonal mean position which is statistically significantly equatorward biased relative to the reanalyses. The CMIP5 models do however represent an improvement over the CMIP3 models, with a more accurate position, and a smaller inter-model spread. When the latitudinal position of the maximum wind-stress is considered by longitude,

it can be seen that the equatorward position bias in the climate models occurs at all longitudes. The bias is predominant over the Pacific Ocean, because the climate model winds fail to make the sharp southward-turn near 150°E evident in the reanalyses (Fig. 3.2c).

The climatological zonal-mean strength of the wind-stress is similar between the reanalyses and climate models, near 0.19 Pa (Fig. 3.2b). Again, the CMIP5 models show a far tighter spread with no outliers, in contrast to the CMIP3 models which had a large spread in strength with two outliers having low wind-stresses of around 0.13 Pa. Nonetheless, the climate models in general exhibit a slightly lower wind-stress than the reanalyses over the Indian and Pacific ocean basins (Fig. 3.2d).

3.3.2 Historical trends in position and strength

Trends are considered for the ensemble mean position and strength of the zonal-mean zonal wind-stress for the four reanalyses, 23 CMIP3 and 21 CMIP5 models over the period 1979-2010. The reanalyses and CMIP5 models show no significant trend in annual mean position, while the CMIP3 models show a trend that is marginally significant (Fig. 3.3a). The reanalyses, CMIP3 and CMIP5 models all exhibit their largest trends in the Austral summer (DJF), all of which indicate a poleward shift in the wind-stress, and are statistically significant. However, the significant poleward trend in DJF is counteracted in all cases by an equatorward trend in JJA (and SON in the reanalyses, but not the climate models). No significant annual-mean positional trends appear on a longitude-by-longitude basis (not shown).

The reanalyses and both groups of climate models show significant positive trends in the strength of the annual-mean wind-stress over the historical period (Fig. 3.3b). The significant annual trends result from the positive trends in wind-stress that occur in all seasons. The largest trends in strength occur in DJF in the reanalyses and CMIP5 models, while the CMIP3 models exhibit the greatest strengthening in SON. In general however, the climate models show a strengthening trend that is significantly weaker than the reanalyses indicate, which can be confirmed by checking that the confidence intervals of the trends do not overlap (Fig. 3.3b). An accurate modern jet strength, together with the underestimation of strength trends over the 20th Century, means that the models have pre-industrial jets that are too weak (see Fig. 4.1 and Section 5.1). Note that I have not included the NASA MERRA and NCEP CFSR reanalyses that exhibit negative strength trends, which may be related to dis-

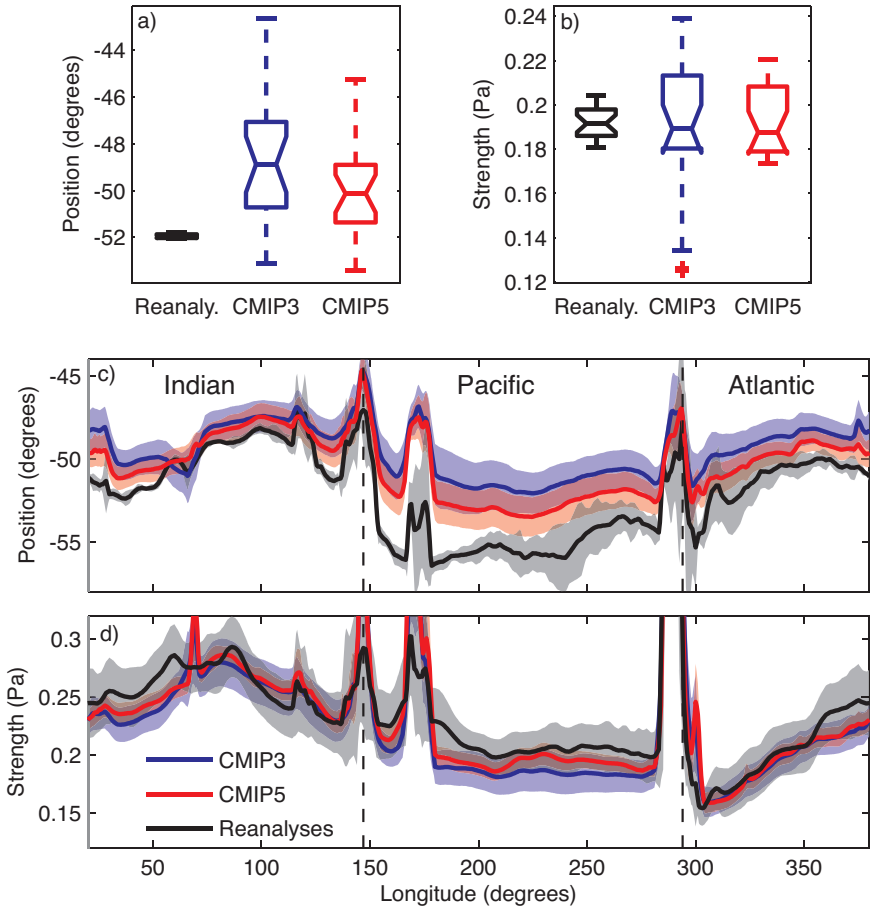

Figure 3.2: Climatologies of the SH surface westerly wind-stress position (a, c) and strength (b, d) over 1979–2010. Four reanalyses, 23 CMIP3 models and 21 CMIP5 models are compared in notched box plots of climatological a) position and b) strength of the zonal-mean zonal wind-stress ; c) latitudinal position by longitude for the reanalyses, CMIP3 and CMIP5 ensemble means and d) strength by longitude for the respective ensemble means. In a), b) whiskers extend to the most extreme data point within 1.5 times the interquartile range, and red plus symbols are outliers. The notches represent a robust estimate of the uncertainty about the medians for box-to-box comparison. Boxes whose notches do not overlap indicate that the medians of the two groups differ at the 5% significance level. Envelopes in c), d) show the 95% confidence interval. Dashed black lines indicate the ocean basin boundaries.

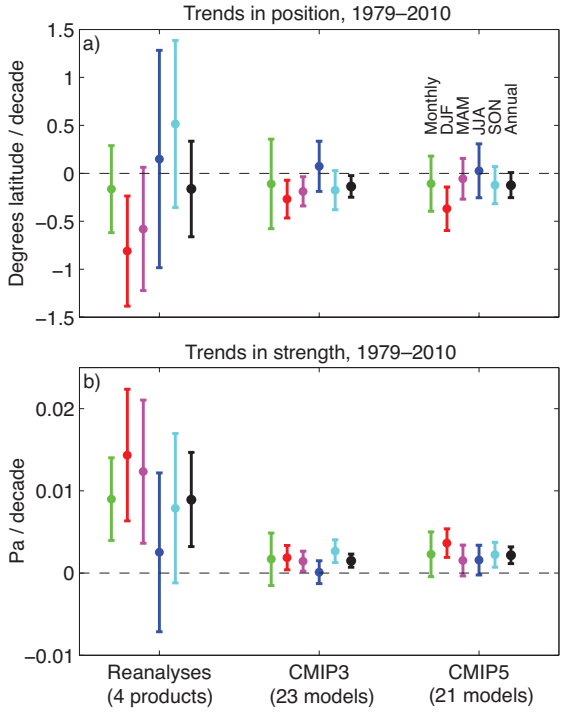

Figure 3.3: Historical trends in the SH surface westerly wind-stress position, a) and strength, b). Trends are computed over the period 1979–2010 on the ensemble mean position and strength from four reanalysis products, 23 CMIP3 models and 21 CMIP5 models respectively. The error bars show the 95% confidence interval of the trends, where auto-correlation has been accounted for. For each ensemble, trends are computed for monthly means, seasonal means and annual means of the zonal-mean zonal wind-stress. For CMIP3 the data are a combination of historical runs (1979–2000) with SRES A1B (2001–2010), and for CMIP5 a combination of historical runs (1979–2005) with RCP4.5 (2006–2010).

continuities associated with the assimilation of ocean surface winds (See Appendix A.4).

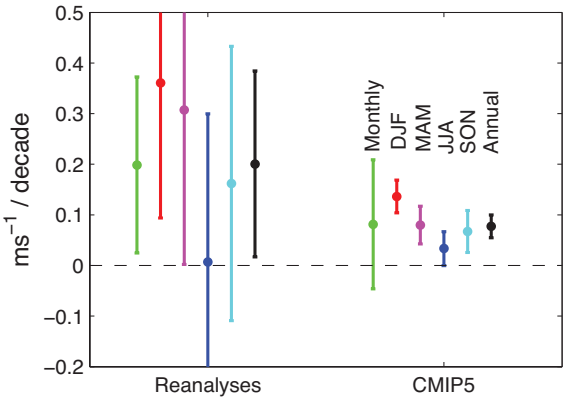

Figure 3.4: Historical trends in the SH surface wind-speed. Trends are computed over the period 1979–2010 on the ensemble mean strength from four reanalysis products and 18 CMIP5 models respectively. The error bars show the 95% confidence interval of the trends, where auto-correlation has been accounted for. For each ensemble, trends are computed for monthly means, seasonal means and annual means of the zonal-mean zonal wind-stress. For CMIP5 a combination of historical runs (1979–2005) with RCP4.5 (2006–2010) is used.

It should also be noted that wind-stress strength trends will be sensitive to the form of the drag-coefficient employed in the climate models and reanalyses. To compare my results to wind-speed I have computed trends in surface wind-speed over the historical period from 1979 to 2010 in reanalyses and the CMIP5 models (Fig. 3.4). As for surface wind-stress, I find significant positive trends in annual mean surface wind speed in both reanalyses and the CMIP5 models. These positive trends in wind-speed are also consistent with station based trends from Southern Ocean islands [Hande *et al.*, 2012; Yang *et al.*, 2007].

3.3.3 Projected changes over the 21st century and sensitivity to CO_2 forcing

The change in the CMIP5 ensemble mean position and strength of the SH westerlies over the 21st century is computed as an anomaly from the 1979-2010 climatology for the four RCP scenarios (Fig. 3.5a, b). The changes are greatest under the strongest CO_2 forcing in RCP8.5 as expected, with a poleward shift of around 1.5° and a strengthening of 0.02 Pa or roughly 10% by the end of the 21st century.

As in the trends over the historical period, the changes in jet strength over the 21st century are more robust than changes in jet position. A statistically significant change in annual mean position occurs only under RCP8.5 by 2100. Changes in jet strength are significant by the century's end for all the RCPs, except for in RCP2.6, under which significant mitigation of anthropogenic emissions occurs. The changes in jet strength and position over the 21st century in the RCPs are the result of opposing trends in CO_2 and ozone forcing. Increasing CO_2 forcing drives the jet to strengthen and move polewards, while recovery of stratospheric ozone drives the jet to weaken and shift equatorward [Son *et al.*, 2010]. Therefore ozone recovery over the 21st century may help to explain the weak trends seen in RCP2.6 and 4.5. The changes in the jet projected by the CMIP3 ensemble under the SRES A2 and SRES A1B scenario fall within the envelope of the RCP projections by the CMIP5 ensemble (Fig. A.3). However, the anthropogenic forcing of the CMIP3 and CMIP5 models during the 21st century differs under the SRES scenarios and RCPs respectively.

To directly compare the relative sensitivity of the multi-model ensembles to CO_2 forcing I use the simulations with a 1% a year increase in atmospheric CO_2 concentration. The simulations begin at an atmospheric CO_2 concentration of roughly 286 parts per million (ppm), as observed around the year 1860, and increase at 1% a year to doubling which occurs 70 years later. The CMIP3 and CMIP5 models both show a continuous poleward shift and strengthening of the SH surface westerly jet in response to this CO_2 forcing (Fig. 3.5c, d). The ensemble mean response of the jet position and strength to CO_2 forcing is very similar in both the CMIP3 and CMIP5 models, and statistically indistinguishable from one another over the 70 year period to CO_2 doubling.

3.4 Summary and conclusions

Changes in the SH surface westerly wind-stress have been associated with changes in the Agulhas leakage [Biastoch *et al.*, 2009], observed warming of the subtropical western boundary currents [Wu *et al.*, 2012], and with frontal shifts and enhanced warming observed in the Southern Ocean [Gille, 2008], with implications for the Southern Ocean carbon sink [Le Quéré *et al.*, 2007; Zickfeld *et al.*, 2008]. I have shown that while a significant strengthening of the zonal-mean SH westerly wind-stress jet has occurred since 1979, there is no consistent evidence for an annual mean shift in the position of the jet over the historical period. However, poleward shifts have occurred

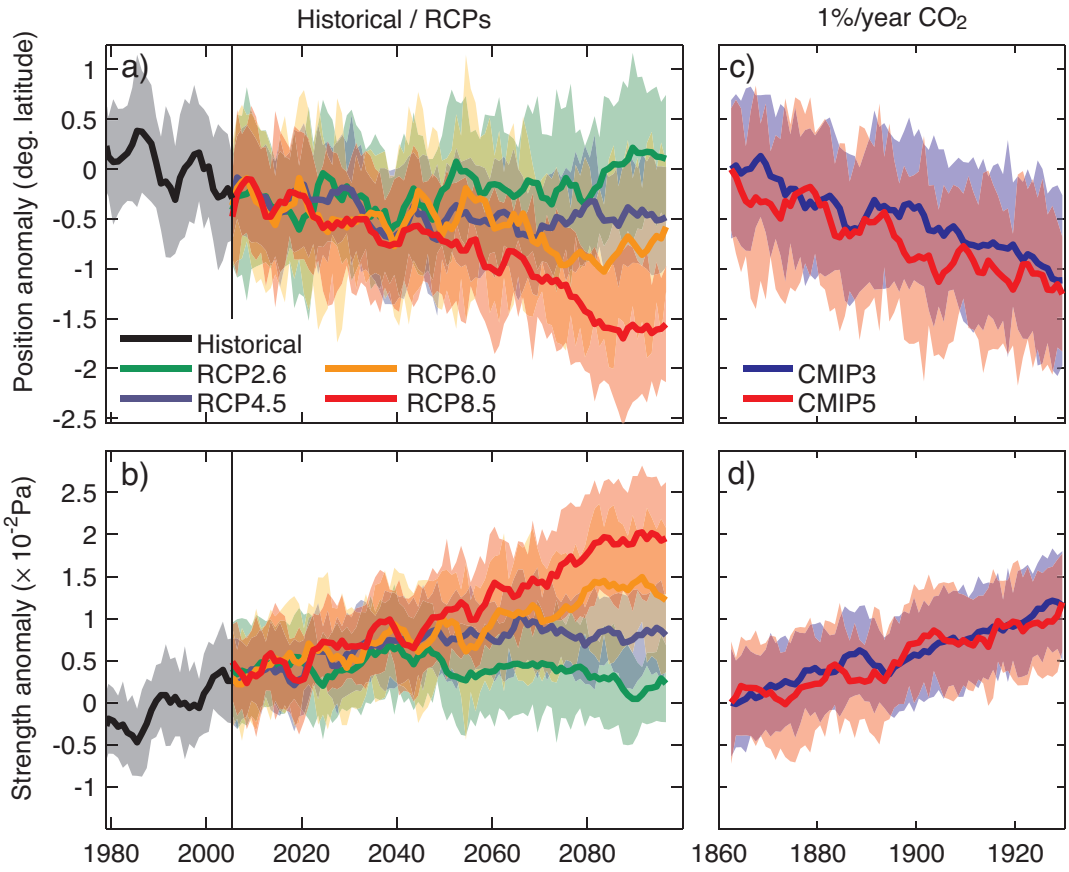

Figure 3.5: Simulated changes in the annual mean SH surface westerly wind-stress position (a, c) and strength (b, d). The CMIP5 ensemble mean jet position and strength anomalies under historical (1979–2005) and four RCP forcing scenarios (2006-2100) are shown in a) and b) ; The CMIP3 and CMIP5 ensemble mean jet position and strength anomalies under a 1%/year increase in atmospheric CO_2 from 286 ppm to doubling are shown in c) and d). Envelopes represent the 95% confidence intervals. Anomalies are relative to the 1979–2010 base-period (a, b) and 1860–1865 (c, d), and are computed from the zonal-mean zonal wind-stress. Data have been smoothed with a 5–year wide boxcar.

during the Austral summer, which is also the season of greatest strengthening. The large changes during the Austral summer are consistent with previous findings, and owe to stratospheric ozone depletion [Son *et al.*, 2010]. Increasing CO_2 forcing operates year-round, and also drives the jet to strengthen and move poleward.

The magnitude of the strengthening trend in the CMIP3 and CMIP5 climate models is significantly smaller than the observed strengthening. Though this result should be interpreted with caution because there is disagreement on the strength trends amongst the reanalyses (see Fig. A.2); lack of observations leads the reanalyses to be unreliable in the Southern Hemisphere [Son *et al.*, 2010], and the lack of atmosphere-ocean coupling in reanalyses with prescribed SST's could influence changes in the jet.

The CMIP5 climate models show less model-to-model variability, and a more accurate position for the SH surface westerly wind-stress than the CMIP3 models, but they remain significantly equatorward biased relative to the reanalyses over the historical period. The CMIP5 ensemble also suggests that the SH surface westerly wind-stress maximum will move poleward by as much as 1.5° and strengthen by as much as 10% by the end of the 21st century in response to anthropogenic forcing. However, the amount of projected strengthening could be an underestimate, since the CMIP5 ensemble significantly underestimates the strengthening of the wind-stress over the historical period relative to reanalyses. This conclusion is however subject to the uncertainties in the reanalyses discussed above.

Temporal changes in the SH winds are thought to have significant implications for the ocean circulation and the carbon cycle in the 21st century [Zickfeld *et al.*, 2007], but the impact of climatological wind-stress biases is as yet unknown. As the coupled climate models evolve into Earth System Models, accurate simulation of the SH wind-stress and its time-evolution becomes vital for robust simulations of climate change, and particularly for the diagnosis of carbon emissions, indicating the SH wind-bias as a key model shortfall requiring attention. In the following chapters, I quantify the magnitude of these wind-stress effects on the ocean carbon cycle.

Chapter 4

The influence of the CMIP3 zonal wind-stress biases on ocean carbon

This chapter is based on the contents of the paper:

N. C. Swart and J. C. Fyfe [Jan. 2012b], Ocean carbon uptake and storage influenced by wind bias in global climate models, *Nature Clim. Change*, **2,** pp. 47–52, DOI: 10.1038/nclimate1289

4.1 Introduction

The oceanic uptake of carbon in coupled carbon-climate models is subject to a number of uncertainties [Friedlingstein *et al.*, 2006]. These include uncertainties in the physical circulation due to poorly resolved dynamics [Meredith *et al.*, 2011], incorrect wind-stress forcing at the ocean surface [Fyfe and Saenko, 2006; Russell *et al.*, 2006b], as well as other uncertainties such as the rate of biological carbon sequestration [Eby *et al.*, 2009; Friedlingstein *et al.*, 2006]. My study isolates and quantifies the uncertainty associated with one of these factors, the surface wind-stress.

The Southern Hemisphere westerly winds display an equatorward biased position and anomalous strength in the pre-industrial control experiments of the Coupled Model Intercomparison Project Phase 3 (CMIP3) models [Meehl *et al.*, 2007b], relative to observed pre-industrial winds (Fig. 4.1). However, the effect of the wind-stress biases on ocean carbon storage in the CMIP3 models has not been directly evaluated because those models do not include interactive carbon cycles [Russell *et al.*, 2006b]. The new generation of carbon-climate models, a subset of CMIP5, now include carbon cycles which allows them to track the flow of carbon through the earth system [Hibbard *et al.*, 2007]. However, inter-model comparisons are confounded by differences in ocean mixing schemes and a number of other factors [Russell *et al.*, 2006a], which independently influence carbon uptake and may obscure the role of the wind-stress bias. To isolate the influence of pre-industrial wind-stress biases on ocean carbon I have designed a novel experiment which eliminates the confounding physical differences between models.

4.2 Methods

4.2.1 Modelled and observed pre-industrial winds

To evaluate the bias in the CMIP3 pre-industrial wind-stresses, I computed a best estimate of the observed pre-industrial wind-stress using re-analysis products. There is uncertainty in the strength of the late 20th century westerly wind-stress in the Southern Hemisphere, as described by the differences between the ERA40 [Uppala *et al.*, 2005], NCEP40 [Kalnay *et al.*, 1996], CORE.v2 [Large and Yeager, 2009] and NOAA_CIRES.v2 [Compo *et al.*, 2011] climatologies. Using the average over these four climatologies provides my best estimate of the 20th century wind-stress,

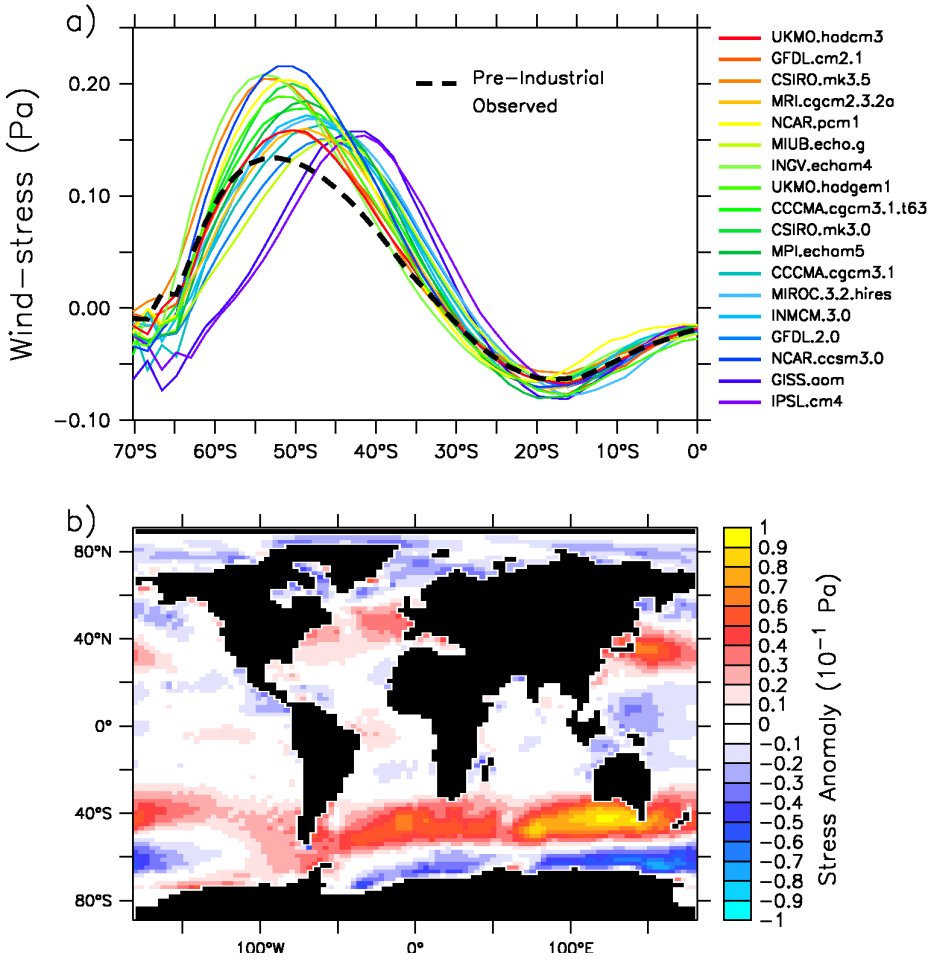

Figure 4.1: **Wind-stress comparisons.** **a,** The zonal mean pre-industrial wind-stress from the 18 CMIP3 models used in this study. The heavy black dashed line shows the observationally derived pre-industrial wind-stress; **b,** Zonal wind-stress anomaly map, computed as the ensemble mean of the 18 CMIP3 wind-stresses minus the observationally derived pre-industrial wind-stress.

$\overline{\tau_{20C}} = 0.25 \times [\text{ERA40} + \text{NCEP40} + \text{CORE.v2} + \text{NOAA\_CIRES.v2}_{1950-2000}]$. Then, I compute a pre-industrial to present-day difference as $\Delta\tau = \tau_{1950-2000} - \tau_{1871-1900}$ where τ is taken from the NOAA–CIRES.v2 twentieth-century reanalysis. My best-guess pre-industrial wind-stress climatology follows as:

$$\tau_{\text{pre-industrial}} = \overline{\tau_{20C}} - \Delta\tau. \tag{4.1}$$

The Southern Hemisphere westerly jet is in about the same location, but weaker by roughly 0.025 Pa in the pre-industrial wind-stress best estimate, compared with the late 20th Century reanalyses.

Then, for 18 models which submitted wind-stress fields to the World Climate Research Programme's (WCRP's) CMIP3 archive [Meehl *et al.*, 2007b], a monthly zonal wind-stress climatology was created using the last 100 years of the pre-industrial control experiment. Almost all of the individual CMIP3 models pre-industrial winds in the Southern Hemisphere are equatorward displaced, and significantly stronger than the observed pre-industrial winds (Fig. 4.1; Table A.2). The CMIP3 ensemble mean strength and position is statistically significantly different from the observations.

Because the biases in the CMIP3 winds are much larger than the uncertainties in observed-winds (Table A.2), my results are qualitatively insensitive to the exact choice for the observed pre-industrial wind-stress. I have tested this by using only the NCEP-40 reanalysis wind-stress for the control run, and found the conclusions to be the same (not shown). The model biases in wind-stress position (about 3°) are on the same order as the meridional-resolution of the model grid (1.8°), yet they are well resolved because their scale is much smaller than that of the westerly-wind jet (about 30°) [Kushner *et al.*, 2001].

4.2.2 Experimental design

For my climate simulations I used version 2.9 of the intermediate complexity University of Victoria Earth System Climate Model (UVic ESCM) [Weaver *et al.*, 2001], which is described in Appendix A.5. The UVic ESCM was started from an established pre-industrial equilibrium and integrated for 7000 years under constant 1850 atmospheric CO_2 concentrations (283.9 ppm) to produce the control run. The control run was forced with my best-estimate of the observed pre-industrial wind-stress. I then conducted 18 equilibrium experiments, which were also integrated for 7000 years under constant 1850 atmospheric CO_2 concentrations, using the 18 individual CMIP3

pre-industrial zonal wind-stress climatologies. These experiments are compared to the 7000 year control run in this work. The only difference between the control run and the experiments was the surface wind-stress field over the ocean.

From the end of the equilibrium runs, I launched transient CO_2 experiments, spanning the period 1850 - 2200. During the transient runs, CO_2 concentrations were allowed to freely evolve, while CO_2 emissions into the atmosphere were specified based on observations until the year 2000 and then following the SRES A2 scenario (A2 from 2000-2100; after 2100 emissions are held constant). All other forcings were held at 1850 levels during the transient runs. In the transient experiments, I continued to force the 18 member ensemble with the CMIP3 pre-industrial winds, while the control simulation forcing remained the best-estimate of the observed pre-industrial wind-stress. The wind-stress was held fixed in order to isolate the effect of the pre-industrial wind-stress bias on the transient simulations.

4.3 Equilibrium carbon storage

4.3.1 The influence of zonal wind-stress

Total ocean carbon storage adjusted to new equilibria over several thousand years in the CMIP3 wind-stress experiments (Fig. 4.2a). The ocean holds less carbon in the wind-stress-biased CMIP3 experiments than in the control simulation that used observed pre-industrial winds. The total range in carbon storage amongst the runs after 7000 years is around 400 Pg, a small fraction of total ocean carbon, but a significant change with respect to the atmospheric carbon reservoir of about 600 Pg. The differences in ocean carbon storage between CMIP3 equilibrium experiments are due to the indirect influence of wind-stress on the air-sea CO_2 fluxes, through changes to the circulation (Fig. 4.2b,c; wind-speed effects are excluded here).

The period required to equilibrate ocean carbon under the CMIP3 wind-stresses is set by the altered surface CO_2 flux, combined with the overturning time-scale required to ventilate the oceanic interior. Changes in the biological pump were relatively minor, and cannot explain the changes in ocean carbon storage. The major adjustment to equilibrium of the ensemble mean over the first 2000 years (Fig. 4.2a), was driven by the time-integrated surface CO_2 flux anomaly (Fig. 4.2c). The flux anomalies were distributed across the surface of the world ocean, but were most prominent in the Southern Ocean. In zonal integral, the ocean south of 30°S accounted for over

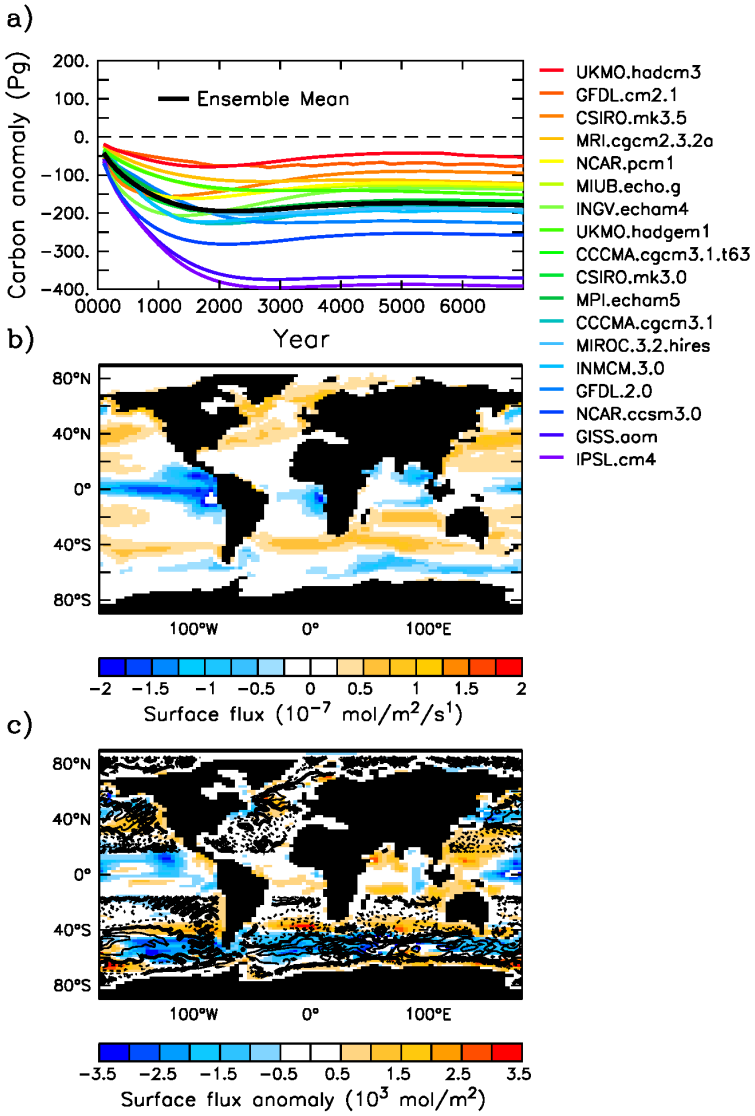

Figure 4.2: **Evolution of ocean carbon to equilibrium. a,** Ocean total carbon anomaly for 18 CMIP3 wind-stress experiments (colored lines) with the ensemble mean shown in black. The anomaly is computed relative to the control simulation; **b,** Ensemble mean surface CO_2 flux of the 18 CMIP3 experiments at year 7000; **c,** The shading shows the ensemble mean surface CO_2 flux anomaly, relative to the control, integrated from year 0 to 2000. Negative values (blue shades) indicate anomalous outgassing from the ocean. The contours show the ensemble mean Ekman pumping anomaly (positive values, the solid contours, indicate increased upwelling). The area 15°S – 15°N, where the Ekman pumping anomaly is not well defined has been masked. Equilibrium experiments were conducted under 1850 forcing, and only surface wind-stress varies between runs.

80% of the variability in global CO_2 surface flux. The decrease in ensemble mean total ocean carbon was principally driven by anomalous outgassing between 40°S and 60°S. Here, the wind-stress bias drove upwelling of carbon rich deep-waters through a positive Ekman pumping anomaly (Fig. 4.2c), which subsequently outgassed to the atmosphere. A compensatory enhanced in-gassing occurred between 20°S and 40°S owing to anomalous downwelling there, but its integrated effect is significantly smaller. Southern Ocean flux anomalies due to wind-stress biases may be smaller in models with higher spatial resolution, but are likely to remain substantial since carbon transport is governed by Ekman dynamics even in eddy-resolving models [Ito *et al.*, 2010].

4.3.2 The effect of including wind-speeds

The surface CO_2 flux is given by

$$F = k_g(k_o \cdot pCO_2^a - CO_{2\,(\mathrm{surf})}^*) \tag{4.2}$$

where k_o is the CO_2 solubility, pCO_2^a is the atmospheric partial pressure of CO_2 and $CO_{2\,(\mathrm{surf})}^*$ is the surface ocean concentration of CO_2 (also see Appendix A.5). Changes in surface wind speed can alter the surface flux by changing the gas transfer velocity, k_g, while surface wind-stress changes can alter vertical Ekman pumping and the surface ocean CO_2 concentration, $CO_{2\,(\mathrm{surf})}^*$ and the temperature dependent solubility, k_o. I have performed additional integrations that include a change to both the wind-stress and wind-speed, for three of the CMIP3 models. The models were chosen so as to have a high (NCAR.ccsm3.0), medium (CCCma.cgcm.3.1) and a low (GFDL.cm2.1) bias in the Southern Hemisphere wind-strength, thus bracketing the previous result (Fig. 4.3).

It can be seen that including the wind-speed effect reduces the ocean carbon storage anomaly for the two cases with medium (CCCma,cgcm.3.1) and high (NCAR.ccsm3.0) wind-stress biases. For the low wind-stress bias case (GFDL.cm2.1), by year 7000, the result of including wind-speed changes is actually to increase the ocean carbon anomaly. While in all cases the inclusion of wind-speed changes the magnitude of the result, it does not alter the conclusion that the CMIP3 pre-industrial wind-stress biases leads to reduced ocean carbon storage. Wind-speed changes were excluded from the main study for simplicity, since wind-speeds also affect other factors in the model such as evaporation.

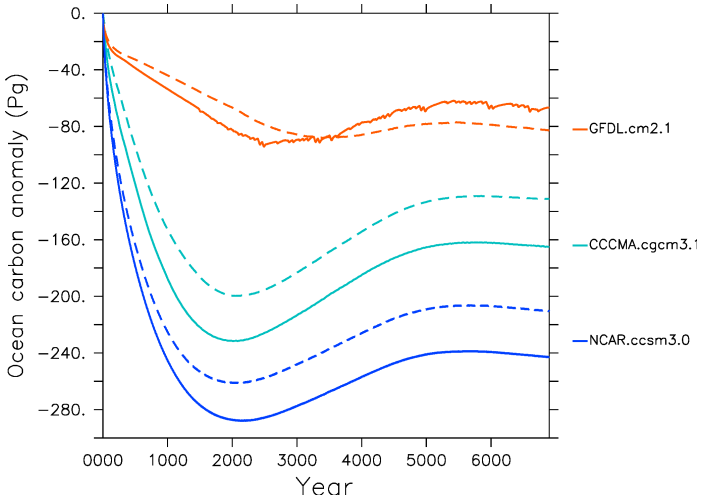

Figure 4.3: **The impact of including wind-speed on ocean carbon.** The solid lines show the adjustment of ocean carbon to changes in wind-stress only (as for Figure 4.2a). The dashed lines show the adjustment when wind-stress and surface wind-speed are changed. The effect is shown for three models with a high (NCAR.ccsm3.0), medium (CCCma.cgcm.3.1) and a low (GFDL.cm2.1) bias in wind-strength.

4.4 Equilibrium ocean carbon distribution

Wind-stress biases also lead to a redistribution of carbon within the ocean. The CMIP3 experiments exhibit an increase in Atlantic carbon storage, and a decrease in Pacific carbon storage, on average, relative to the control (Fig. 4.4a). The changes amount to only several percent of the total carbon storage locally, but again represent a significant fraction of the atmospheric reservoir. The inter-basin redistribution of carbon cannot readily be explained by surface CO_2 flux changes, which were nearly zonally symmetric (Fig. 4.2b). Rather, the Atlantic accumulation of carbon occurred principally between 500 and 4000 m, north of 40°S and was associated with a slow-down in the upper-limb of the Meridional Overturning Circulation (MOC; Fig. 4.4b).

As we shall see below, the MOC slowdown resulted from changes in the Agulhas leakage. The Agulhas leakage refers to the transport of Indian Ocean water into the South Atlantic via the Agulhas Retroflection south of Africa, and is the principal conduit for Indo-Atlantic exchange [Beal *et al.*, 2011]. Variability in Agulhas leakage strength is linked to Atlantic MOC variability on centurial to millenial timescales by paleo-observations [Peeters *et al.*, 2004], and Atlantic salinity trends in modern observational records [Biastoch *et al.*, 2009]. Previous modelling studies have shown that the Agulhas leakage modulates MOC strength through the Indo-Atlantic exchange

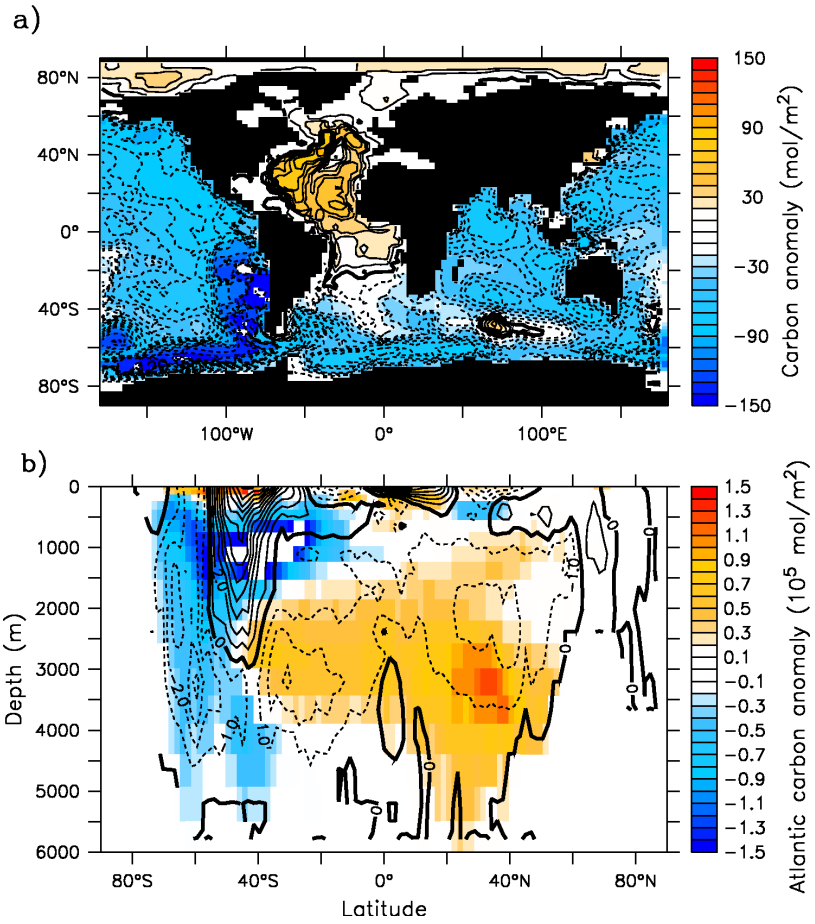

Figure 4.4: **Equilibrium ocean carbon storage. a,** Ensemble mean ocean total carbon anomaly (column inventory) of the 18 CMIP3 wind-stress experiments; **b,** Ensemble mean zonally integrated total carbon anomaly for the Atlantic ocean is given by the shading. Contours show the ensemble mean global meridional overturning stream-function anomaly. Contour interval is 1 Sv. All anomalies are computed relative to the control simulation forced with observed pre-industrial winds, and are based on the mean over years 6900 – 7000

of salt [Weijer *et al.*, 1999], and contributes to MOC variability on decadal [Biastoch *et al.*, 2008] to millennial timescales [Sijp and England, 2008; Sijp and England, 2009].

The strength of the Agulhas leakage depends on the latitude of the zero in wind-stress curl in the Indian Ocean south of Africa [Biastoch *et al.*, 2009; Sijp and England, 2008]. In our equilibrium experiments, models with equatorward positions of the zero wind-stress curl exhibit a reduced Agulhas leakage (Fig. 4.5a) and Indo-Atlantic salt exchange. Models with a reduction in the Indo-Atlantic salt flux in turn experienced a freshening of the near surface North Atlantic (Fig. 4.5b). Here vertical density gradients are more salinity dependent, and hence North Atlantic convection was reduced proportionally to the degree of freshening associated with a reduced Agulhas leakage (Fig. 4.5c). A reduction in the deep water formation rate is what lead to a slow down in the uper-limb of the Atlantic MOC (Fig. 4.5d). A slower MOC, with reduced Indo-Atlantic exchange then caused the accumulation of carbon in the Atlantic that we see in the CMIP3 experiments (Fig. 4.5e). Thus, the relative degree of Atlantic carbon accumulation is directly dependent on the volume flux of the Agulhas leakage (Fig. 4.5f). Similarly, the decrease in total ocean carbon in the Indo-Pacific basins is due to a compensating acceleration of the lower-limb of the MOC (Fig. 4.4b).

To understand the mechanism, consider the conservation of total ocean carbon following an water parcel (i.e. a Lagrangian framework), given by:

$$\frac{\delta C_{\text{total}}}{\delta t} = s \tag{4.3}$$

where s represents all sources and sinks of carbon, including from air-sea exchange and biological processes. For a water parcel at depth, s is dominated by the input and remineralization of carbon from the biological rain. For the trivial case in which s is constant everywhere, the carbon concentration is simply $C_{\text{total}} = st + c_0$. Here the total carbon concentration is linearly dependent on the time available for accumulation. Slowing the circulation, or otherwise displacing younger waters with older waters (for example by changing the relative contributions of NADW and AABW) will increase the carbon concentration and total carbon storage through this accumulation of the biological rain. This is what is observed to occur in the Atlantic basin in the CMIP3 wind-stress experiments. By contrast, speeding up the circulation reduces the time available for biological rain accumulation, resulting in the decreased carbon concentrations. The biological rain is in fact not constant in space or time over the ocean. Indeed, changes in advection, air-sea fluxes and biological productivity all influence

carbon concentrations locally, as seen for example in the large negative Pacific carbon anomalies adjacent to Chile. Nonetheless the biological pump remains of similar strength between the CMIP3 experiments, and the above mechanism contributes to the broad inter-basin carbon anomalies seen in the CMIP3 experiments. However, physical circulation changes that deepen the thermocline in the Indo-Pacific, lead to a warming of the surface ocean, and contribute to the decrease in carbon storage through direct solubility effects. Similarly, cooling of the deep ocean, through a relative shift in the contributions of NADW and AABW increase carbon storage there, and particularly so in the region of Atlantic accumulation (see Chapter 5 for more discussion of these mechanisms).

4.5 Transient ocean carbon uptake

Differences in equilibrium ocean carbon storage affect the oceanic uptake of carbon during time-evolving (transient) climate-change simulations. Transient simulations spanning the period 1850–2200, were launched from the end of the 7000 equilibrium experiments. Atmospheric CO_2 was allowed to evolve freely while carbon emissions were specified following scenario A2 of the Special Report on Emissions Scenarios (SRES) [Meehl *et al.*, 2007a], for both the CMIP3 experiments and the observed wind-stress control simulation. In the transient experiments, I continued to force the 18 member ensemble with the CMIP3 pre-industrial winds, while the control simulation forcing remained the observed pre-industrial wind-stress. I held the wind-stress fixed, rather than evolving, so that we could isolate the effect of the pre-industrial wind-stress bias on the transient simulations. Varying the wind-stress during these simulations (as in Zickfeld *et al.* [2007]), would make it impossible to differentiate the separate effects of the pre-industrial equilibrium wind-stress bias and the transient wind-stress impact.

Carbon emissions increased atmospheric CO_2 concentrations, altered the air-sea pCO_2 gradient, and forced a net oceanic uptake of carbon across all the CMIP3 transient simulations, and the control simulation forced with observed pre-industrial winds. Natural outgassing of carbon from the ocean (Fig. 4.6b) was reduced due to increasing atmospheric CO_2 concentrations, and a decreasing ΔpCO_2 in the tropical upwelling regions for all the simulations, and led to the net oceanic uptake. Over periods in which the deep-ocean circulation becomes important, there are significant differences in the rate of ocean carbon uptake amongst the simulations (Fig. 4.6a).

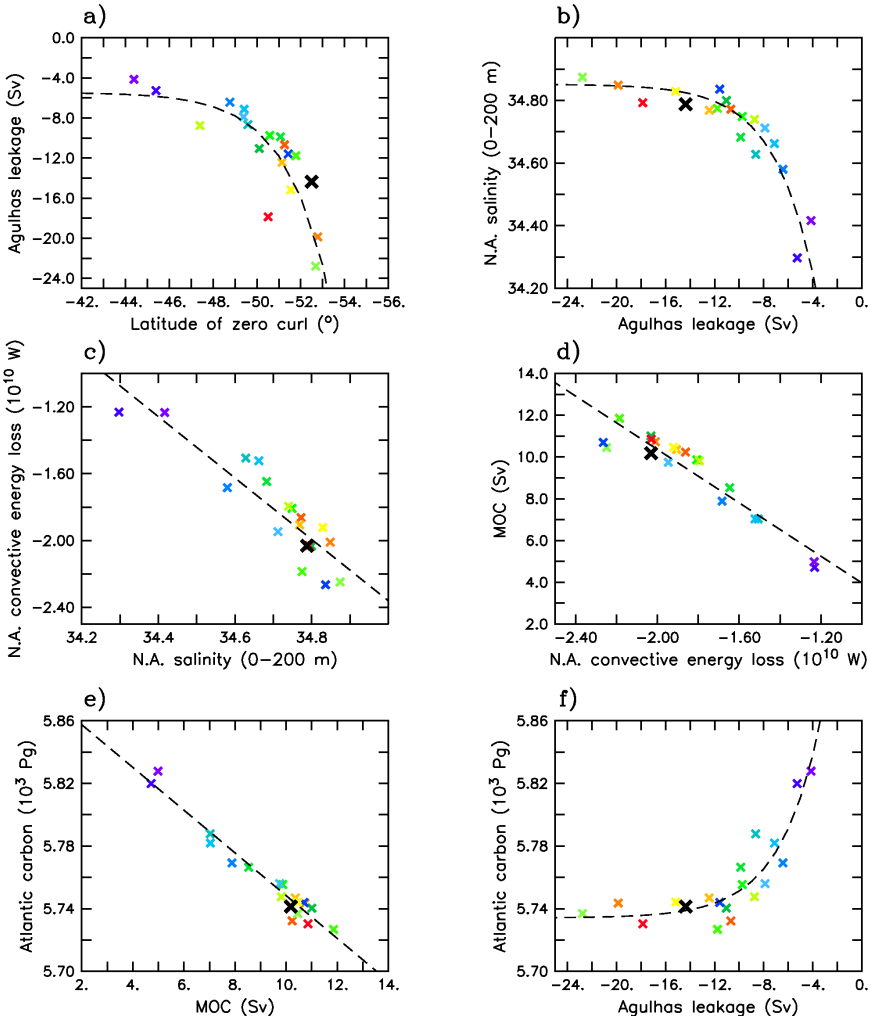

Figure 4.5: **Equilibrium carbon-circulation relations. a,** Latitude of zero wind-stress-curl over the Indian Ocean (mean 20 – 40°E) vs. Agulhas Leakage at 20°E; **b,** Agulhas Leakage (20°E) vs. mean North Atlantic salinity in the upper 200 m; **c,** Mean North Atlantic salinity (0 – 200 m) vs. Energy loss from convection in the North Atlantic; **d,** Energy loss from convection in the North Atlantic vs. global Meridional Overturning stream-function (mean 500 – 2000 m, 30°S – 60°N); **e,** Mean MOC steam-function (500 – 2000 m, 30°S – 60°N) vs. Atlantic carbon (30°S – 60°N); **f,** Atlantic carbon (30°S – 60°N) vs. Agulhas Leakage (20°E). All variables are plotted based on the equilibrium experiment year 6900–7000 mean. Dashed lines represent exponential (a, b, f) and linear (c, d, e) least squares fits to the data. The colour scheme for the markers corresponds to Fig. 1. The heavy black markers show the control, forced with observed pre-industrial winds.

All the CMIP3 runs uptake more carbon than the control run. In total, by year 2200 there is a 100 Pg range in total ocean carbon uptake amongst the CMIP3 runs. This represents an uncertainty amongst the models of roughly 10% of the 1000 Pg of total ocean carbon uptake since 1850.

The principal reason for the increased ocean carbon storage by the CMIP3 experiments relative to the control is an anomalously large reduction in oceanic outgassing of carbon from the principal natural outgassing regions in the tropical Pacific (Fig. 4.6c). The predominant signal in the tropics is related to the air-sea pCO_2 gradient. Here, the deep-water upwelling in the CMIP3 wind simulations had a lower carbon content than the control (see Fig. 4.2a), leading to a reduced pCO_2 gradient, and a decrease in equatorial outgassing in the CMIP3 wind simulations, relative to the control. Thus, inter-experiment differences in uptake rates during the transient simulations are principally due to differences in the oceans deep-water carbon concentration. The pre-industrial wind-stress bias led to a bias in the deep ocean carbon initial condition of the transient experiments, causing these low deep-water carbon concentrations and increased uptake of atmospheric CO_2. This over-estimation of ocean carbon sequestration in our CMIP3 transient climate simulations leads to a modest under-estimation of atmospheric CO_2 relative to the control (Fig. 4.7)

4.6 Discussion

The effects of the wind-stress bias on ocean circulation and carbon dynamics will have a dependence on the details of the mesoscale eddy field [Meredith *et al.*, 2011]. Coarse resolution climate models, such as those used in CMIP3, are unable to explicitly resolve mesoscale eddies, but typically use the Gent-McWilliams [Gent and McWilliams, 1990] scheme to parameterize the effects of sub-grid scale eddy mixing. I acknowledge this limitation, but point out that these models are prominent tools used in projecting future climate change. Consistent with my objective to test the influence of wind-bias in the CMIP3 models, I have used a model which has a typical CMIP3 resolution, and which employs the Gent-McWilliams eddy parameterization (the UVic ESCM). Since my results are expressed as anomalies from a control simulation, additional tests (not shown) reveal that my results are largely insensitive to the exact magnitude of isopycnal diffusivity specified in the Gent-McWilliams scheme (but we return to this topic in Chapter 5). Southern Ocean circulation errors due to wind-stress biases may be smaller in models with higher spatial resolution, but are

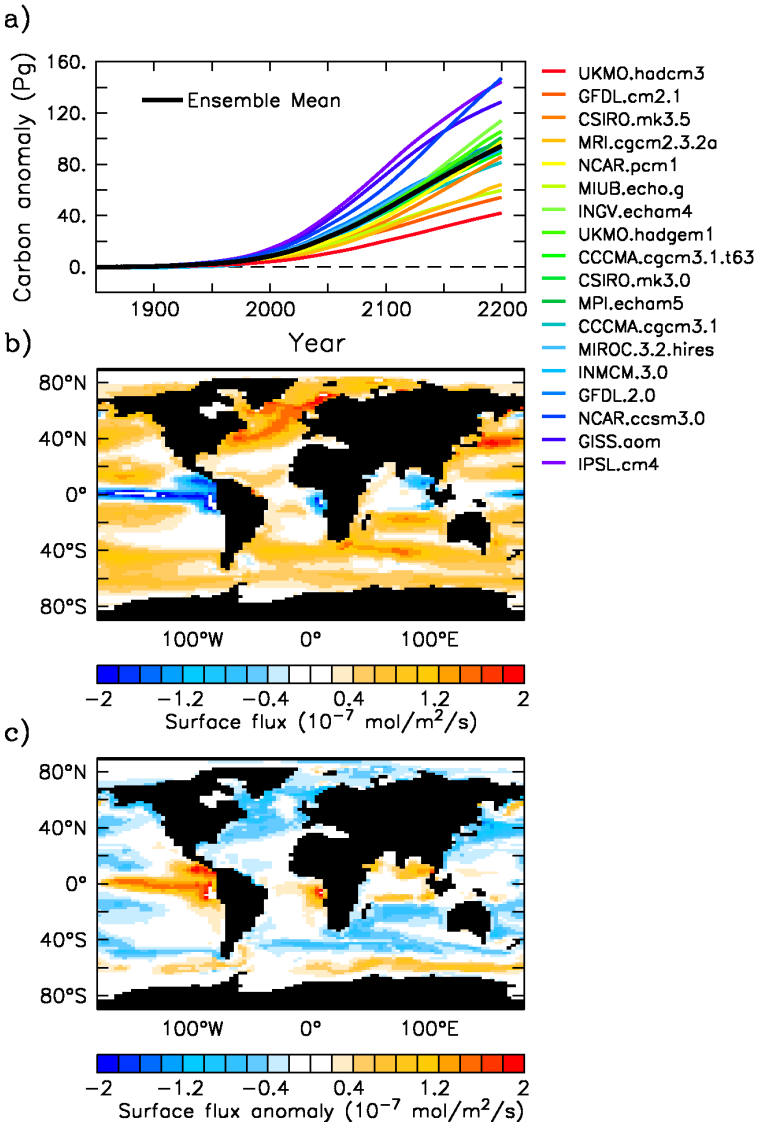

Figure 4.6: **Transient ocean carbon uptake.** **a,** Total ocean carbon uptake anomaly for the 18 CMIP3 experiments, relative to the control simulation with observed winds. The black line shows the ensemble mean uptake anomaly; **b,** Ensemble mean surface CO_2 flux of the 18 CMIP3 experiments at year 2200; **c,** Ensemble mean surface CO_2 flux anomaly. Anomalies are computed as the CMIP3 experiment ensemble mean at year 2200 minus the ensemble mean at 1850, minus the control simulation difference (2200 – 1850). The transient experiments used the end point of the equilibrium experiments (Fig. 1a) as their initial condition. All forcing, including wind-stress, was held constant at pre-industrial levels, except for atmospheric CO_2 emissions, which increased from 1850 to 2100 according to the SRES A2 scenario, and then were held fixed (see text for details).

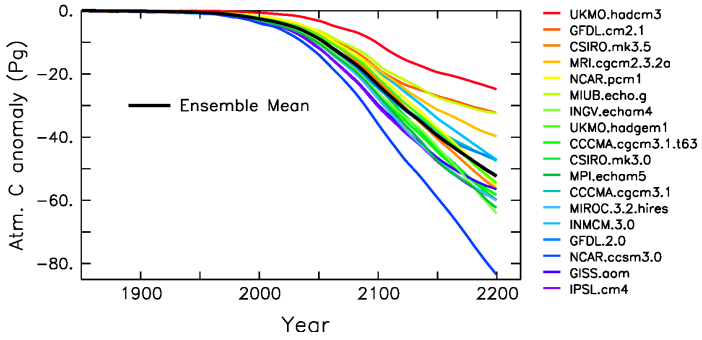

Figure 4.7: **Atmospheric CO_2 anomaly.** The coloured lines represent the atmospheric CO_2 change since 1850 in the CMIP3 experiments, minus the atmospheric CO_2 change in the control simulation forced with observed pre-industrial winds. The solid black line is the ensemble mean of the 18 CMIP3 experiments. Although atmospheric CO_2 is increasing over time in all the experiments, the CMIP3 atmospheres accumulate less CO_2 than the control, leading to the negative anomaly shown here. Atmospheric CO_2 emissions increased from 1850 to 2100 according to the SRES A2 scenario, and then were held fixed, but wind-stress remained pre-industrial.

likely to remain substantial [Meredith *et al.*, 2011]. Similarly, the details of the Agulhas leakage are modulated by mesoscale-eddy processes [Biastoch *et al.*, 2009], that the UVic ESCM does not directly resolve, yet our result of a reduced Agulhas leakage occurring due to an equatorward displaced westerly wind-stress is fully consistent with eddy-resolving model simulations [Biastoch *et al.*, 2009].

In the original CMIP3 coupled models the wind-stress evolves in time, generally exhibiting a poleward shift over the 20th and 21st centuries [Kidston and Gerber, 2010; Fyfe and Saenko, 2006]. It has previously been shown that CMIP3 ensemble mean 20th century poleward wind-shift can increase ocean carbon uptake in transient climate change experiments [Zickfeld *et al.*, 2007]. The pre-industrial initial condition bias that we describe here is independent and of greater magnitude than the previously described changes induced by the transient poleward wind-stress shifts [Zickfeld *et al.*, 2007]. Note that our results pertain to a single climate model, forced by different wind-stresses. Caution should be used in generalizing these results to inter-model or model-observation comparisons, because other uncertainties in ocean carbon uptake may influence the signal that I have described.

4.7 Conclusions

I have isolated and quantified one out of several potential uncertainties in modelled ocean carbon uptake rates. Current climate model wind-stress biases will reduce pre-industrial ocean carbon storage, as well as increase ocean carbon uptake and reduce atmospheric CO_2 in transient climate change simulations, relative to simulations with unbiased winds, that are otherwise identical. The CMIP3 spread of wind-stress biases lead to an uncertainty in ocean carbon uptake of approximately 10% by year 2200. My findings should help with interpreting uncertainties in the next generation of coupled carbon-climate models being used in the CMIP5 exercise.

Chapter 5

The influence of CMIP5 wind biases and transient wind changes on ocean carbon

5.1 Introduction

In Chapter 4 I demonstrated that the pre-industrial zonal wind-stress bias in the CMIP3 models had a significant influence on ocean carbon storage. In this chapter, I update those results using the CMIP5 ensemble winds. I then extend my investigation to examine the influence of other components of the pre-industrial wind.

It is also known that the time-evolution of the winds can influence carbon uptake in the Southern Ocean. Using inversions of atmospheric CO_2 and a coarse-resolution ocean model forced at the surface by reanalysis winds and buoyancy fluxes Le Quéré *et al.* [2007] proposed that the observed strengthening of the Southern Hemisphere westerlies reduced the net uptake of carbon by the Southern Ocean. This so-called "saturation of the Southern Ocean CO_2 sink" occurred because the intensified winds increased outgassing of natural CO_2 from the Southern Ocean, a result also found in other studies using coarse resolution ocean models and reanalysis based surface forcing [Lovenduski *et al.*, 2008; Lovenduski *et al.*, 2007]. The intensified outgassing of natural CO_2 is offset by ingassing of anthropogenic CO_2 due to rising atmospheric concentrations, but which term ultimately dominates the net Southern Ocean CO_2 flux is a matter of debate and may change in time [Zickfeld *et al.*, 2008]. Additionally the wind-induced circulation changes are modulated by ocean eddies [Böning *et al.*, 2008] not resolved, nor adequately parameterized [Hallberg and Gnanadesikan, 2006] in these studies using coarse resolution models. The future response of Southern Ocean carbon-climate feedbacks is therefore uncertain, but of key interest given the primary importance of the region for anthropogenic CO_2 uptake [Gruber *et al.*, 2009]

Coupled climate models are the most comprehensive tools available to examine such changes. The influence of simulated time-evolving winds has previously been considered only for the CMIP3 multi-model ensemble mean wind, where the pre-industrial bias was artificially corrected [Zickfeld *et al.*, 2007]. Using an ensemble mean wind-field is however problematic, because in the Southern Hemisphere where the models jets are offset from each other, the ensemble mean jet will have a low-biased strength (see Figure A.4). Here I advance on Chapter 4 and previous studies, by isolating the influence of simulated wind-changes on ocean carbon uptake for the individual members of the CMIP5 ensemble, comparing the magnitude of this "transient wind effect" to the "pre-industrial bias" effect described above, and testing the sensitivity of the ocean response to the parameterization of mesoscale eddies.

5.2 Surface winds in the CMIP5 models and Reanalyses

5.2.1 Pre-industrial winds

The pre-industrial zonal-mean zonal wind-stress of the CMIP5 models fall within a narrow envelope over most latitudes, except in the westerly wind belts (see Appendix A.7 for details of the models used). The region of the Southern Hemisphere westerlies has the largest inter-model spread (Fig. 5.1a). The model winds, here representing a climatology over 1871–1899, may be compared with the Twentieth Century Reanalysis (20CR) winds [Compo *et al.*, 2011] over the same period. The model winds are largely consistent with the 20CR winds over most latitudes, except for in the region of the Southern Hemisphere westerlies.

The CMIP5 multi-model ensemble mean wind-stress shows a Southern Hemisphere westerly jet that is equatorward displaced and too strong relative to 20CR. These CMIP5 pre-industrial wind biases are similar to those of the CMIP3 ensemble discussed in Chapter 4, and the equatorward bias is similar to that over the satellite era discussed in Chapter 3. Therefore, these results extend the conclusions of a satellite-era CMIP5 zonal wind-stress bias in Chapter 3 to the pre-industrial era. The models meridional wind-stress similarly shows a spread in the region of the SH westerlies as well as in a region near 65°N, but 20CR generally falls within the model spread, and the biases are not significant as they were for τ_x (Fig. 5.1b).

There is more significant disagreement between the pre-industrial surface wind speeds. At mid-to-high latitudes the CMIP5 wind-speeds are significantly higher than those in 20CR. The largest wind-speed difference is between 40° and 50°S where the equatorward displacement of the models jets relative to 20CR enhances the difference beyond the general offset seen at the surrounding latitudes. Two CMIP5 models, CanESM2 and MRI-CGCM3, have particularly high wind-speeds, the latter especially clear north of 60°N. Also shown for comparison is a modern era climatology over 1968–1996 from NCEP Reanalysis 1 (R1; Kalnay *et al.* [1996]), which is the default wind-climatology used in the UVic model (Fig. 5.1). The CMIP5 model pre-industrial wind speeds generally fall within the bounds of the reanalysis climatologies, but are generally more similar to the R1 modern era climatology than the 20CR pre-industrial climatology. The weak high-latitude wind-speeds in the 20CR pre-industrial climatology are in fact questionable, as discussed in Appendix A.7.1.

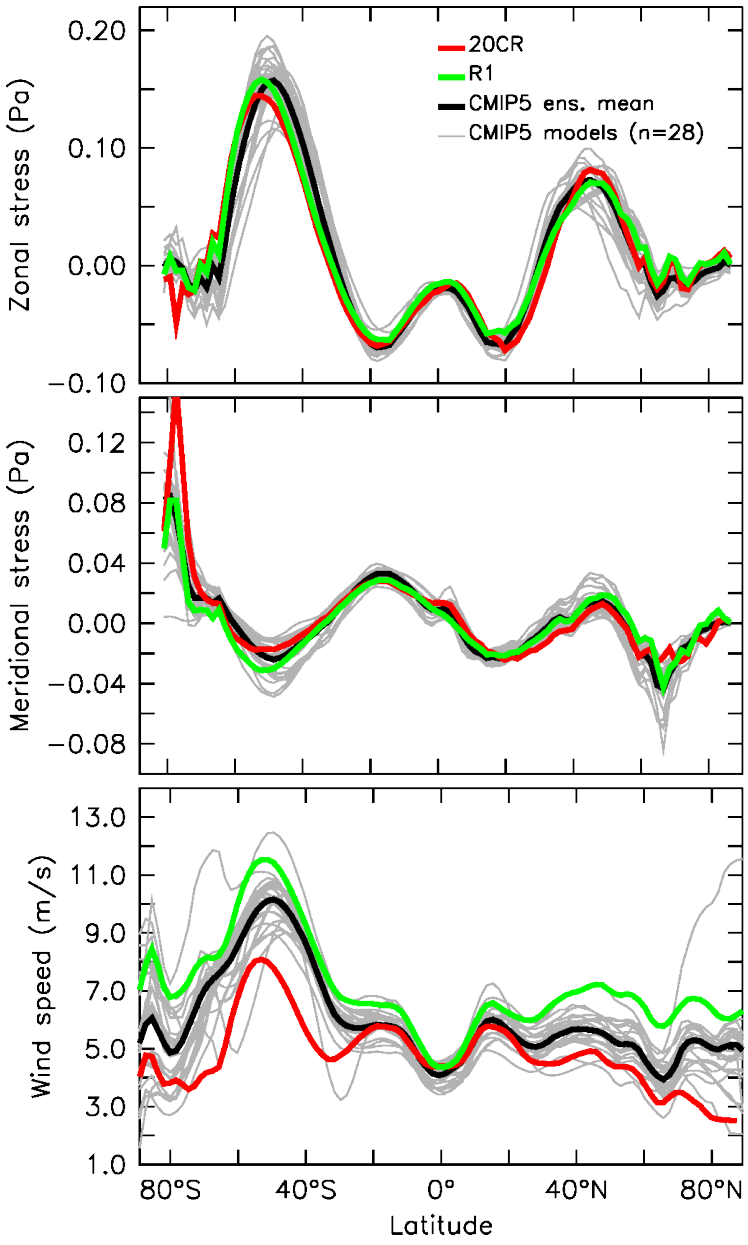

Figure 5.1: The zonal-mean zonal wind-stress (a), meridional wind-stress (b) and surface wind-speed (c) of 28 CMIP5 models for the climatological period 1871–1899. The CMIP5 ensemble mean wind-stress is also shown (black), together with the winds from the 20th Century Reanalysis over the same climatological period (red) and the default winds used in the UVic model (green), which are based on a 1968–1996 climatology from NCEP Reanalysis 1.

5.2.2 Wind changes over the 20th and 21st centuries

We now focus on the Southern Hemisphere westerly wind jet, where model biases and temporal changes are the largest. The strength of the westerly jet is defined as the maximum in the zonal-mean zonal wind-stress or wind-speed between 70° and 20°S, or as the minimum of the zonal-mean meridional wind-stress over those latitudes, for each variable respectively. It is worthwhile to note here that the ensemble mean of the CMIP5 jet strengths computed over the individual models is not equal to the strength of the jet in the ensemble mean wind, as illustrated in Figure A.4.

The CMIP5 wind-stress and speed fields show a strengthening of the jet from 1871 to 2100 (Fig. 5.2) and also exhibit a poleward jet shift (not shown here but see Chapter 3). The zonal wind-stress shows the largest relative change. The ensemble mean of the CMIP5 jet strengths in τ_x is too high relative to 20CR in the late 19th century. Over the course of the 20th Century, the CMIP5 models underestimate the strengthening of the jet, and by the end of the 20th century have an ensemble mean jet strength which is similar to, or slightly weaker than 20CR. This result is consistent with the conclusion that the models underestimate the jet strengthening trend over the satellite era from Chapter 3, and it extends that conclusion to the whole 20th century (subject to the uncertainty in 20CR trends discussed in A.7.1). The model underestimation of the jet strengthening trend explains how the models can have a roughly accurate jet strength over a satellite-era climatology (see 3.3), but overestimate the strength of the pre-industrial jet relative to 20CR (e.g. Fig. 5.1a).

The observed strengthening of the SH westerly winds is also seen in R1, which exhibits a roughly similar trend to 20CR, and a far larger trend than the CMIP5 models (Fig. 5.2). However the Southern Hemisphere winds are poorly constrained by the reanalyses [Son *et al.*, 2010], especially in the pre-satellite era, where the trends in both available products, R1 and 20CR, are questionable as detailed in Chapter 3 and Appendix A.7.1 respectively. Thus, the 20th century trends in SH jet strength could be i) underestimated by the CMIP5 models, ii) overestimated by the available reanalyses, or iii) both. As discussed in Chapter 3, the jet strengthening does appear to be a robust result with strong positive trends (much greater than the CMIP5 models) seen in τ_x in four out of six reanalyses over the more reliable satellite era (e.g. Figures 3.3 and A.2), as well as consistent wind-speed trends observed at weather stations in the Southern Ocean [Hande *et al.*, 2012; Yang *et al.*, 2007]. Thus, the balance of evidence seems to suggest option i), that the models underestimate the strengthening

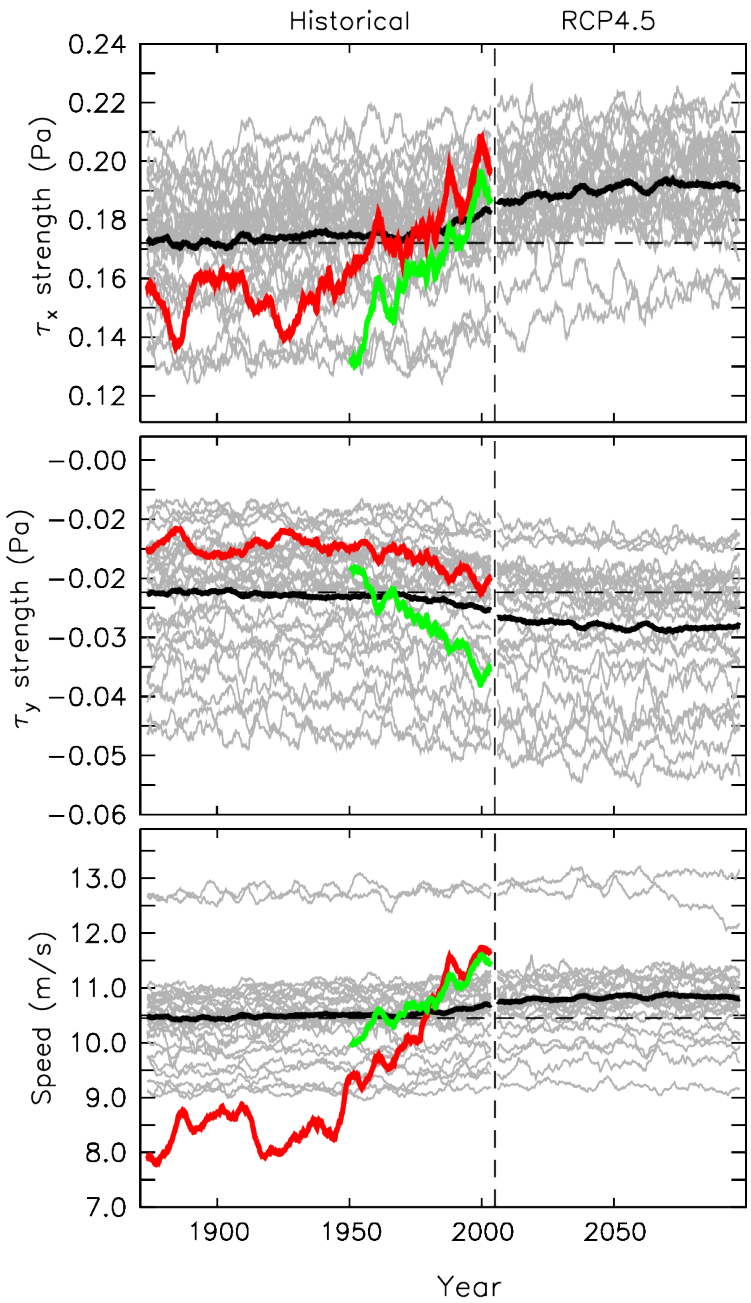

Figure 5.2: The time-evolution of the maximum strength of the zonal-mean SH westerly wind jet in zonal-wind stress (top), meridional wind-stress (middle) and in wind-speed (bottom). The historical period (1871–2005) includes 28 CMIP5 models, and the period 2006–2100 is based on the RCP4.5 experiments of 24 CMIP5 models. Also shown is the jet evolution in 20CR (red), and in R1 (green). All lines have been smoothed with a 5-year wide boxcar filter.

trend, as the most likely. Owing to this uncertainty in the reanalysis wind trends I will use both the pre-industrial (1871 to 1899) 20CR climatology and the more reliable modern (1968 to 1996) R1 based climatology to assess model performance in simulations of ocean carbon storage and uptake.

5.3 Modifications to the UVic Earth System Climate Model

5.3.1 Wind forcing

The aim of this chapter is to assess how the biases in the CMIP5 models pre-industrial winds and the temporal wind-changes over the 20th and 21st centuries influence ocean carbon uptake. Following the approach in Chapter 4, this will be done by forcing the UVic ESCM [Weaver *et al.*, 2001, see Appendix A.5 for the model descrpition] with winds derived from the CMIP5 models.

The total wind-effect on the ocean can be partitioned into the individual effects from different components of the wind. In the UVic ESCM (see Fig. 5.3) the winds are partitioned into three basic components: (i) vertically integrated atmospheric winds (w_a) that advect heat and moisture; (ii) surface wind-speeds (w_s) that drive the turbulent exchange of tracers between the ocean (or land) surface and the atmosphere and (iii) surface wind-stresses over the ocean that have a zonal and meridional component (τ_x and τ_y respectively) which drive ocean dynamics along with the surface buoyancy forcing. Experiments have been done to test the influence of each surface wind component, and these are introduced in the following section.

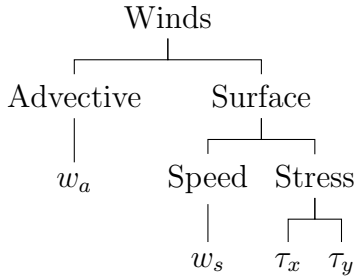

Figure 5.3: Wind-components in the UVic ESCM.

5.3.2 Eddy parameterization

The Gent-McWilliams (GM) eddy parameterization [Gent *et al.*, 1995; Gent and McWilliams, 1990] as implemented in many coarse resolution models, including the UVic ESCM, to have a fixed coefficient of eddy diffusivity, has recently been criticized [Hallberg and Gnanadesikan, 2006; Böning *et al.*, 2008; Gent and Danabasoglu,

2011]. In the real ocean, increases in Southern Ocean winds that tend to drive a more vigorous Eulerian mean overturning circulation and incline the isopycnals are thought to be largely compensated for by increases in the opposing eddy-induced overturning circulation, which tends to relax the isopycnals back towards the horizontal, resulting in little net change in the observed isopycnal slopes [Böning *et al.*, 2008] and correspondingly in the residual overturning circulation (see Section 2.1.3 for a review of terminology). The importance of the enhanced Southern Ocean eddy activity compensating for increasing Southern Ocean winds has been shown in the high-resolution simulations of Spence *et al.* [2009]; Spence *et al.* [2010] and by using a coefficient of eddy diffusivity dependent on the wind-stress as in Fyfe *et al.* [2007].

This effect can be taken into account by including a variable coefficient of eddy diffusivity into the GM parameterization. Here the GM parameterization was updated to have a variable coefficient in the same manner as described in Gnanadesikan *et al.* [2006], Farneti and Gent [2011] and Saenko [2012]. Briefly, instead of assuming that the GM coefficient of eddy diffusivity is constant everywhere, it is allowed to vary in space and time and is prescribed as:

$$\mathrm{v}K_{\mathrm{GM}}(x,y,t) = \frac{\alpha}{h-h_m}\int_{-h}^{-h_m} |\nabla\rho|\,\partial z\left(\frac{gL^2}{\rho_0 N_0}\right) \tag{5.1}$$

where g is the gravitational acceleration, $\rho_0 = 1025$ kg m^{-3} is a constant reference density, N_0 is a prescribed constant buoyancy–frequency of 0.004 s^{-1}, L is a constant prescribed eddy length scale of 50 km, α is a dimensionless tuning constant, and $|\nabla\rho|$ is the horizontal density gradient or baroclinicity which is averaged over depths between $h_m = 100$ and $h = 2000$ m. The range of $\mathrm{v}K_{\mathrm{GM}}$ is then constrained between a minimum of 300 and a maximum of 5000 m^2 s^{-1}. To highlight the influence of the eddy response to changing winds, this variable coefficient GM scheme was employed in specific experiments that are described below (i.e. the regular GM scheme with a fixed coefficient is used unless noted).

5.4 The influence of CMIP5 wind-biases on equilibrium ocean carbon storage

5.4.1 Experiments

The UVic ESCM was initialized from a previously established model equilibrium [Eby *et al.*, 2013] and integrated for 5000 years, with the external forcing (greenhouse gas, sulphate aerosol, land-use, orbital, solar) set to year 1800 levels. All components of the wind (τ_x, τ_y, w_s and w_a) were set to a 20CR wind-climatology computed over the period 1871–1899, and this simulation using 20CR winds is called control C1. Over the course of the 5000-year simulation, the model comes into equilibrium with the prescribed 20CR wind and year-1800 radiative forcing.

Then three discrete experiments were conducted in order to isolate the influence of each component of the CMIP5 surface winds. For each experiment, 5000-year runs were done for an ensemble of 28 members of the UVic ESCM, with each member forced by a monthly wind climatology from an individual CMIP5 model, which had been re-gridded to the UVic model grid. Each ensemble member in the experiments was initialized from the same established model equilibrium, and subjected to the same year–1800 forcing as the control simulation, C1. The CMIP5 monthly wind climatologies were derived from data spanning the period 1871–1899, to be consistent with the 20CR climatology used in control C1 (1871–1899 is the first 30-years available from 20CR). In the CMIP5 models, the 1871–1899 climatology is very similar to climatologies produced from the pre-industrial control runs (not shown).

In the first experiment (E1) each of the 28 ensemble members had its zonal wind-stress (τ_x) replaced by the CMIP5 τ_x, while all other wind components remained the 20CR climatology. In the second experiment (E2), the zonal and meridional wind-stress ($\tau_x + \tau_y$) were both replaced with CMIP5 winds, and in the third experiment (E3) the surface wind-speed was also replaced ($\tau_x + \tau_y + w_s$). In all these experiments the atmospheric advective winds remained those from the 20CR climatology. These three experiments are compared to control C1 in the text (Table 5.1).

Because of the uncertainties in the 20CR surface wind speeds (Section 5.2 and Appendix A.7.1), another control simulation (C2) was done, this time setting all components of the wind (τ_x, τ_y, w_s and w_a) to the R1 wind-climatology computed over the period 1969–1996 (the default winds used by the UVic model). A fourth experiment (E4) was then done, setting all the surface wind-components ($\tau_x + \tau_y + w_s$)

Table 5.1: Simulations with fixed winds and fixed year–1800 forcing. The name of the run, the source of the wind-fields, the GM scheme and the number of runs (#) are indicated. The Difference field shows how anomalies were computed for each experiment, and it is indicated in which Figure they are shown.

Name	τ_x	τ_y	w_s	w_a	vK_{GM}	#	Difference	Figure
C1	20CR	20CR	20CR	20CR	NO	1		
E1	CMIP5	20CR	20CR	20CR	NO	28	D1=E1-C1	5.4a
E2	CMIP5	CMIP5	20CR	20CR	NO	28	D2=E2-C1	5.4b
E3	CMIP5	CMIP5	CMIP5	20CR	NO	28	D3=E3-C1	5.4c
C2	R1	R1	R1	R1	NO	1		
E4	CMIP5	CMIP5	CMIP5	R1	NO	28	D4=E4-C2	5.6a
C3	R1	R1	R1	R1	YES	1		
E5	CMIP5	CMIP5	CMIP5	R1	YES	28	D5=E5-C3	5.6b

to the CMIP5 climatologies. In experiment E4 the atmospheric advective winds are set to those from the R1 wind-climatology. Experiment E4 is therefore nearly a repeat of experiment E3, the only differences being the atmospheric advective winds, and the control to which the experiments are compared (Table 5.1). The large size of the CMIP5 3-d atmospheric fields precluded me from computing advective winds from each CMIP5 model. However, testing the sensitivity of ocean carbon to the influence of changing atmospheric advective winds suggests it to be small compared to changes in the surface wind components (Fig. A.7).

Then to test the influence of the choice of GM coefficient a third control simulation was done (C3), setting all components of the wind (τ_x, τ_y, w_s and w_a) to the R1 wind-climatology, and utilizing the variable coefficient GM parameterization. A fifth experiment (E5) was also done, setting all the surface wind-components ($\tau_x + \tau_y + w_s$) to the CMIP5 climatologies, the atmospheric advective winds to the R1 wind-climatology, and using the variable coefficient GM parameterization (vK_{GM}). These simulations are described in Table 5.1 and a full map of this chapter's experimental design is shown in Fig. A.9. We now explore the results.

5.4.2 Total ocean carbon storage

The CMIP5 zonal-wind stresses in experiment E1 cause the ocean to lose carbon relative to the control C1 in 26 out of 28 ensemble members (Fig. 5.4a). The experiment ensemble mean total ocean carbon loss was about 130 Pg, which is sizeable relative to the atmospheric carbon reservoir, and statistically significantly different from zero at the 5% significance level given the inter-model spread in ocean carbon of about 250 Pg (based on a one-sample t-test, and the null hypothesis that the ensemble mean anomaly is zero).

This CMIP5 wind-stress induced anomaly has a similar pattern, but a magnitude that is about 70 Pg less than that found for the comparable CMIP3 wind expriment in Chapter 4. This is to be expected since the CMIP5 wind-biases are similar, but slightly smaller than those in CMIP3 relative to 20CR (Fig. 4.1). The 28 member CMIP5 ensemble used here is also larger than the 18-member CMIP3 ensemble used in Chapter 4, and the control used there was a "hybrid" of several reanalyses, not the pure 20CR control used here.

The surface flux anomalies relative to the control show regions of gain and loss across the global ocean, but the negative anomalies representing oceanic outgassing

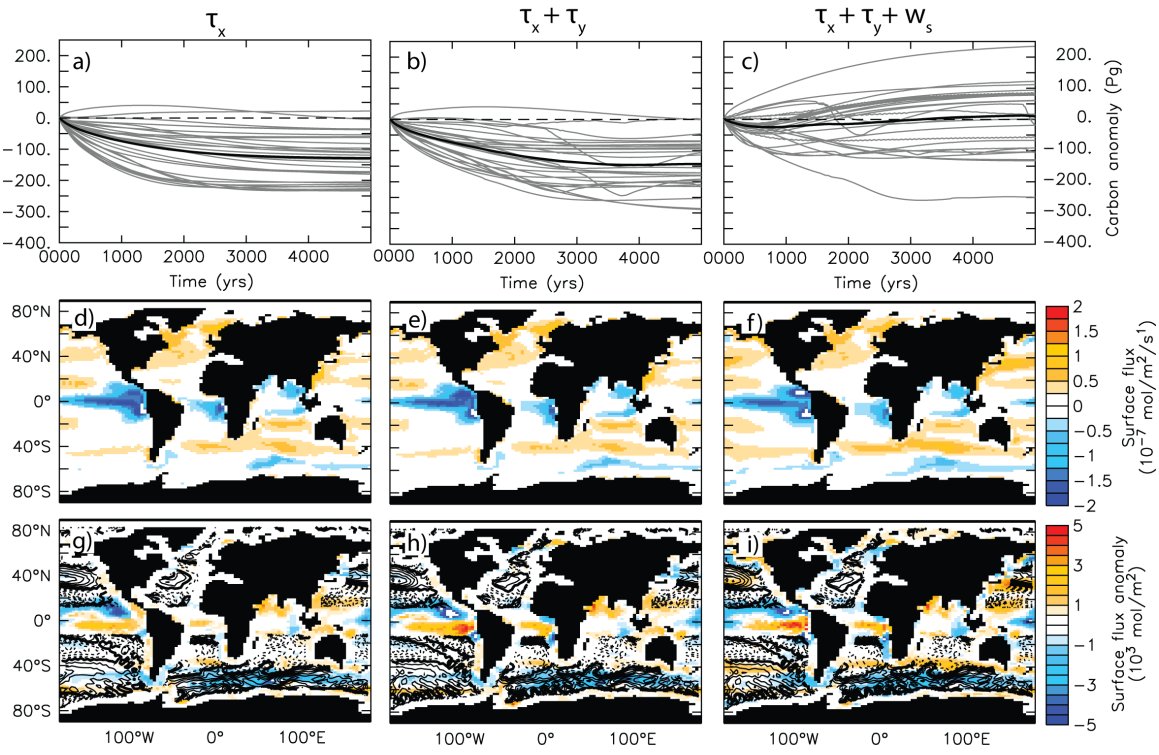

Figure 5.4: (a, b, c) The total ocean carbon evolution under 28 CMIP5 model winds in the spin-up runs, expressed as an anomaly relative to the 20CR control (C1), and shown for the three experiments E1, E2 and E3 described in the text; (d, e, f) the ensemble mean surface CO_2 flux; (g, h, i) the ensemble mean surface CO_2 flux anomaly relative to the 20CR control (C1) time-integrated from years 0 to 2000 is shown in shading, and the Ekman pumping anomaly is shown in contours. The black solid line in a), b) and c) is the experiment ensemble mean.

are concentrated in the Southern Ocean between about 40 and 60°S (Fig. 5.5d). The region of Southern Ocean outgassing is associated with positive Ekman pumping anomalies (Fig. 5.4g). In this region, a stronger wind-stress curl in the experiments drives enhanced northward Ekman transport, speeding up the residual Southern Ocean overturning circulation, and leading to upwelling of carbon rich deep waters that outgas to the atmosphere. Compensatory ingassing anomalies driven by negative Ekman pumping anomalies occur to the north and south, but are too small to fully compensate the strong outgassing, making the Southern Ocean a net source of carbon to the atmosphere relative to the control (Fig. 5.5g).

Including the CMIP5 meridional wind-stress components in experiment E2 does not significantly influence the picture already described (Fig. 5.4b). The ensemble

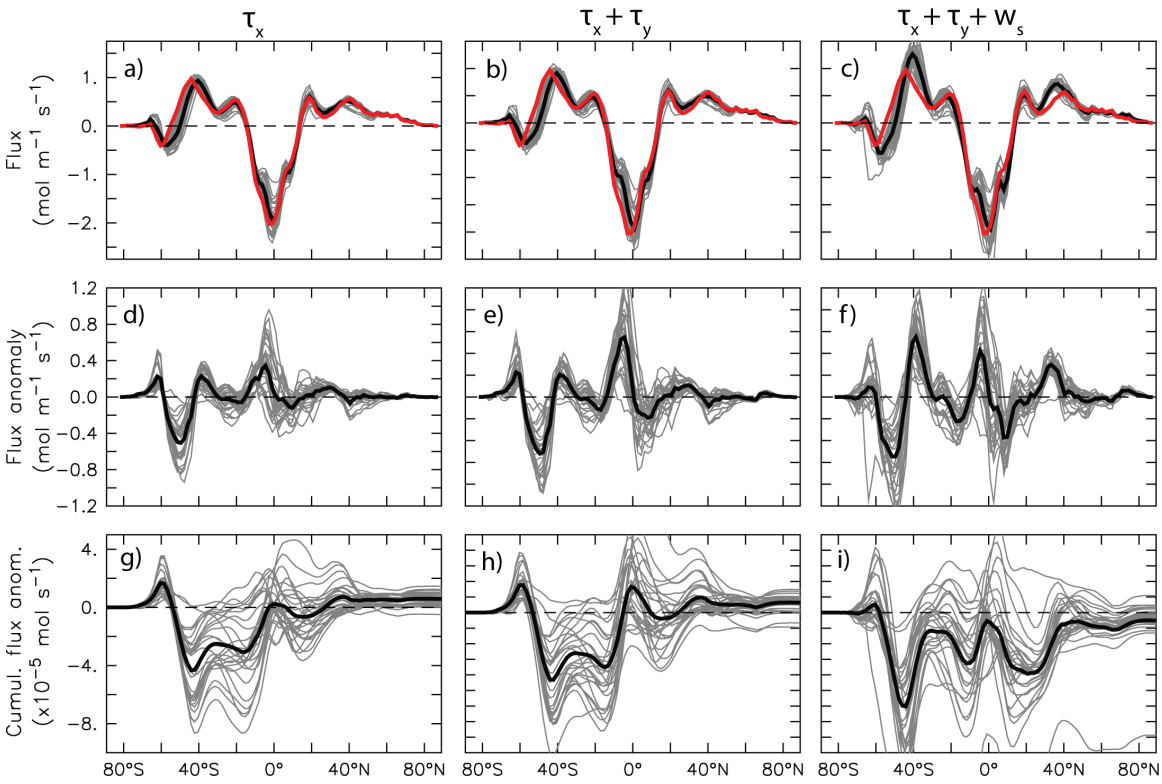

Figure 5.5: (a, b, c) The zonally integrated surface flux of CO_2 for the 28 CMIP5 experiments (grey) and the 20CR control (C1) in red, for the three experiments E1, E2 and E3; (d, e, f) the zonally integrated flux anomaly in the experiments, relative to the 20CR control ; (g, h, i) the zonally integrated flux anomaly, cumulated from south to north. All fields represent time averages over the years 4900 to 5000. The black solid lines are the experiment ensemble mean.

mean total ocean carbon loss of around 150 Pg is somewhat more than in the τ_x experiment. This occurs because including τ_y increases the wind-stress curl anomaly relative to the 20CR control (C1), increasing the strength of Ekman pumping anomalies and outgassing over the Southern Ocean (Fig. 5.5e). The flux anomalies near the equator also increased in magnitude, with anomalous ingassing near 5°S becoming particularly large. This equatorial flux anomaly, enhanced by the meridional wind stresses, is concentrated in the eastern Pacific (Fig. 5.4h), and is likely associated with the well known double Intertropical Convergence Zone (ITCZ) problem in models, which causes excessively strong trade-winds and insufficient asymmetry around the equator [Lin, 2007], as in Fig. 5.1. Two ensemble members also developed somewhat unstable behaviour and failed to reach a solid equilibrium, because of the onset

of periodic millennial timescale Southern Ocean flushing episodes, similar to those described for the UVic model by Meissner *et al.* [2008].

The addition of CMIP5 wind-speeds in experiment E3 significantly alters the picture (Fig. 5.4c). The ocean carbon loss in many ensemble members is turned into a carbon gain by changing to the CMIP5 wind speeds, and the ensemble mean anomaly becomes slightly positive, but is not statistically significant. The strong wind-stress driven outgassing anomalies still occur in the Southern Ocean between about 40 and 60°S, and are in fact enhanced by the switch to CMIP5 wind-speeds (Fig. 5.5f). However, the compensating ingassing anomalies immediately to the north of this are relatively more enhanced by the wind-speeds. The enhanced compensatory ingassing forces the Southern Ocean ocean closer towards being flux neutral in the integral sense, as opposed to being a region of strong net negative fluxes as in the previous two experiments (Fig. 5.5i). The wind-speeds also enhanced the flux anomalies in the northern hemisphere. The net result is a near zero ensemble mean flux anomaly, and ocean carbon storage anomaly relative to control C1. However, as noted the 20CR pre-industrial wind-speeds may be low-biased, which might have influenced this result.

The experiment E4, which is a repeat of E3, but uses the R1 climatology advective winds and is compared to the R1-based control, C2, was done in order to bracket the uncertainty in the ocean response to the different reanalysis wind speeds. Relative to the C2 control the experiment E4 ensemble mean loses about 65 Pg of ocean carbon after 5000 years (Fig. 5.6a), which is statistically significant at the 5% level (based on a one-sample t-test, and the null hypothesis that the ensemble mean anomaly is zero). Several ensemble members still show the reversal from carbon-loss to carbon-gain seen in experiment E3, but the effect is not sufficient to balance the carbon loss in the remaining ensemble members. Relative to control C2, the largest negative flux anomalies in the experiment still occur in the Southern Ocean, with strong compensation to the north and south (Fig. 5.7c), but in general the anomalies are smaller than in experiment E3. The equatorial anomalies between 20°S and the equator still occur, but are also weaker than in E3.

Changing the physical model to have a variable rather than constant eddy diffusivity reduces the relative ocean carbon loss. In the variable GM experiment, E5, the ensemble mean ocean carbon loss relative to control C3 was only around 30 Pg (Fig. 5.6b). In this case, the ensemble mean anomaly at year 5000 is no longer statistically significant 5% level. In the variable GM experiment, several ensemble members

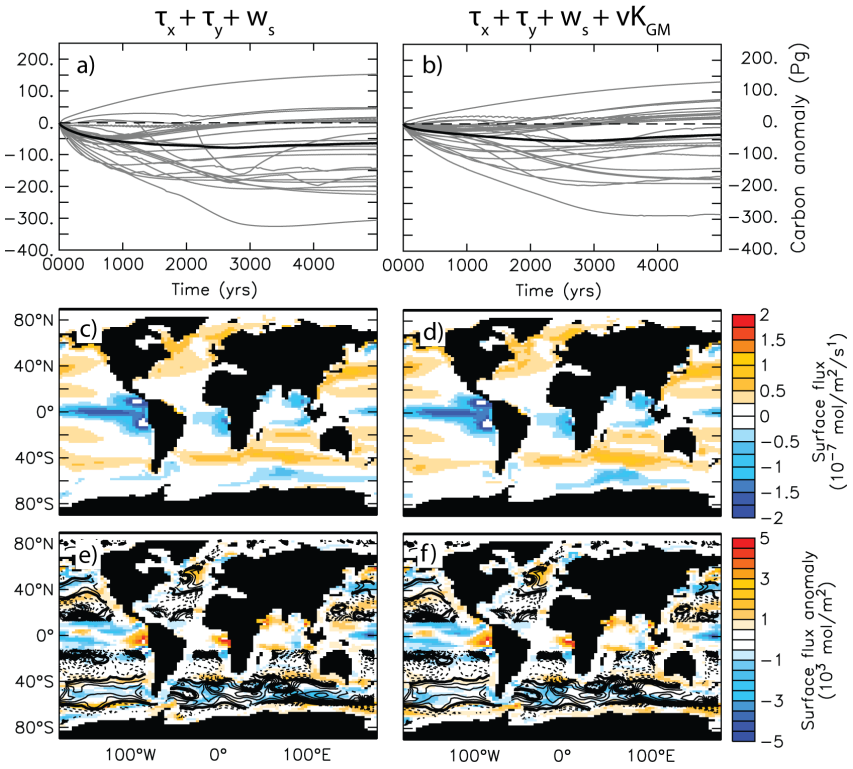

Figure 5.6: (a, b) The total ocean carbon evolution under 28 CMIP5 model winds in the spin-up runs, expressed as an anomaly relative to the respective R1 control, and shown for the a) fixed and b) variable GM experiment; (c, d) the ensemble mean surface CO_2 flux; (e, f) the ensemble mean surface CO_2 flux anomaly relative to the R1 control time-integrated from years 0 to 2000 is shown in shading, and the Ekman pumping anomaly is shown in contours. The black solid line in a) and b) is the experiment ensemble mean. Anomalies in a), c) and e) are relative to the fixed GM control (C2) while anomalies in b), d) and f) are relative to the variable GM control (C3).

reverse behaviour and begin to gain ocean carbon after around year 2000, and these runs appear to take longer to reach equilibrium. The reduction in ocean carbon loss in the variable GM experiment (E5) relative to the regular GM experiment (E4), can be partly attributed to reduced outgassing from the Southern Ocean (see Appendix Fig. A.10). Thus, the net effect of including all components of the surface winds, and a variable GM scheme is to reduce the ensemble mean ocean carbon anomaly to near zero in the experiment using CMIP5 winds relative to the R1 based control. However, this near-zero net ocean carbon storage anomaly is the result of large but compensating surface flux anomalies, which affect the distribution of carbon within

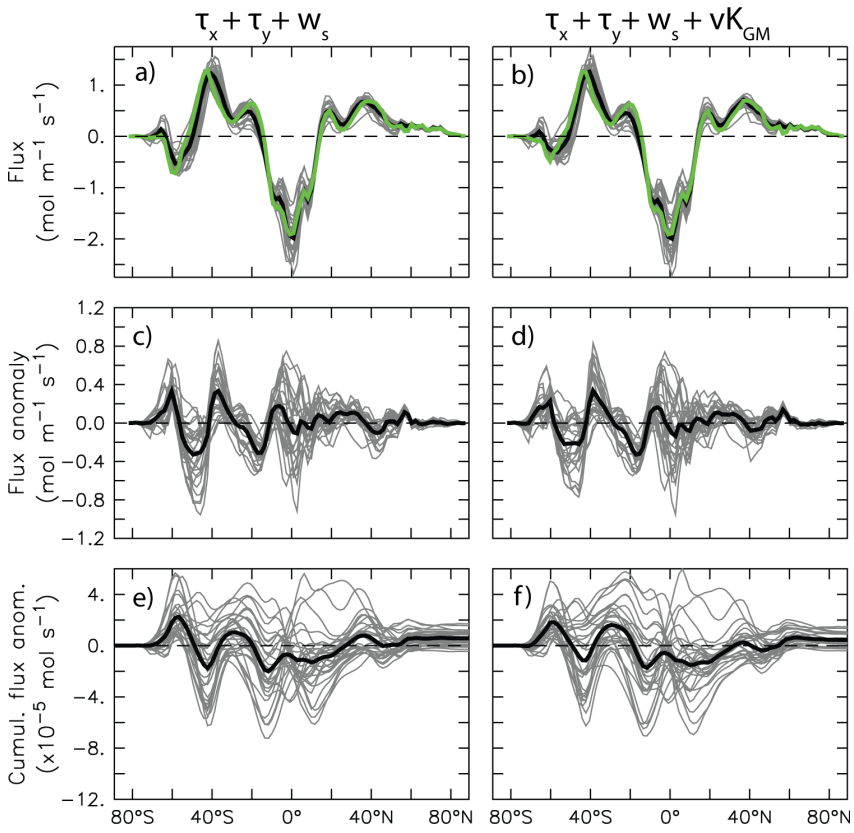

Figure 5.7: (a, b) The zonally integrated surface flux of CO_2 for the 28 CMIP5 experiments (grey) and the R1 respective control in green for the a) fixed and b) variable GM experiment; (c, d) the zonally integrated flux anomaly in the CMIP5 experiments, relative to the R1 control; (e, f) the zonally integrated flux anomaly, cumulated from south to north. All fields represent time averages over the years 4900 to 5000. The black solid lines are the experiment ensemble mean. Anomalies in c) and e) are relative to the control C2, while anomalies d) and f) are relative to control C3.

the ocean.

5.4.3 Ocean carbon distribution

The column inventory of total ocean carbon shows that the CMIP5 winds cause a redistribution of ocean carbon. Carbon accumulates in the deep Atlantic basins and is depleted in the Indo-Pacific in the CMIP5 ensemble-mean relative to the control (Fig. 5.8). The carbon redistribution is in general similar for the regular (E4) and variable (E5) GM experiments, and also broadly similar to that seen under the CMIP3 zonal-wind stresses seen in Chapter 4. Therefore, we restrict further examination to the variable GM experiment.

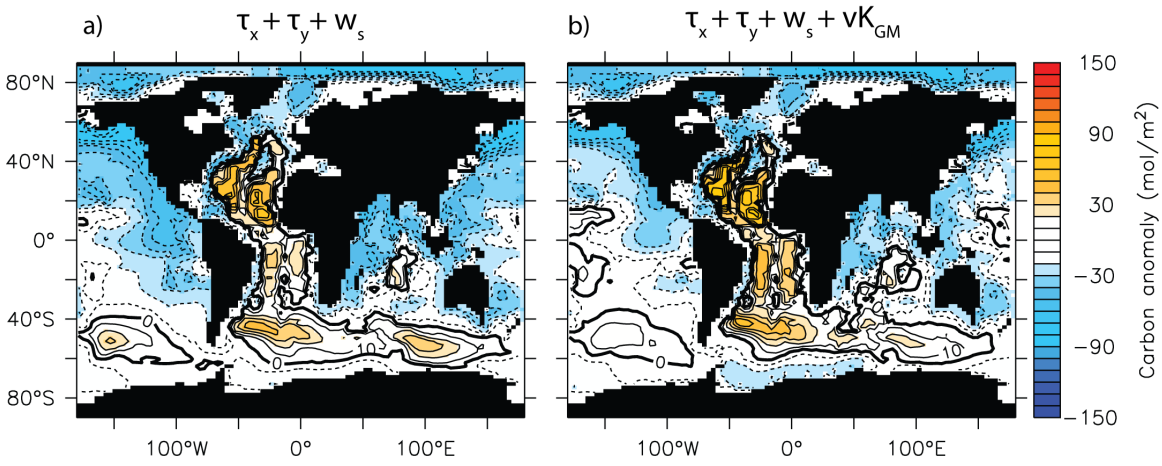

Figure 5.8: The experiment ensemble mean column inventory of total ocean carbon, expressed as an anomaly relative to the respective R1 control, and shown for the a) fixed and b) variable GM experiment; a) is relative to control C2 and b) is relative to control C3.

Carbon was also redistributed vertically in the ocean under the CMIP5 winds (Fig. 5.9). In the zonal-mean, the global ocean lost carbon from thermocline waters spanning the upper 2,000 m, with a weak accumulation of carbon at greater depths. The net loss of ocean carbon already discussed above was driven by the loss of carbon from thermocline waters dominating over the deep-water carbon gain. The deep-accumulation of carbon occurred almost exclusively in the Atlantic basin, explaining the increased Atlantic column inventory. The vertical distribution of Atlantic carbon accumulation is also very similar to that seen under the CMIP3 wind-ensemble (Fig. 4.4, but note that figure uses a zonal-integral over the Atlantic not a zonal-mean).

By contrast, the loss of carbon from the thermocline waters occurred predominantly in the Indo-Pacific basins (Fig. 5.9b).

The change in ocean carbon distribution can be related to changes in MOC (Fig. 5.9d). The relative accumulation of carbon in the Atlantic which occured between depths of 3,000 and 5,000 m, occured due to the replacement of relatively new, low carbon North Atlantic Deep Water (NADW) with older, more carbon rich Antarctic Bottom Water (AABW). The displacement of the NADW overturning cell by the AABW cell can be seen in the MOC streamfunction (Fig. 5.9f). The greatest shoaling of the NADW cell occured near 40°N and 3,500 m depth, coincident with the maximum Atlantic ocean carbon anomaly. However, shoaling of the NADW cell and carbon accumulation occured throughout the Atlantic basin, centred on a depth near 4,000 m.

In this region of the North Atlantic close to the NADW formation region, the NADW waters are comparatively young, while by contrast at depths near 4,000 m the AABW is on its return limb to the Southern Ocean, and is comparatively old. The older AABW is more carbon rich largely owing to the additional time it has had to accumulate carbon from the biological rain as discussed in Section 4.4. The wind-induced circulation changes also lead to a cooling of the deep ocean and a warming of the thermocline in the experiment ensemble mean relative to the R1 control (Fig. 5.10). The cold anomalies, coincident with the expansion of the AABW cell, can also account for increased deep carbon storage in the Atlantic, because of increased CO_2 solubility.

The NADW cell is weakened and displaced by the AABW cell because of changes in the winds. In particular, the Agulhas leakage mechanism described in Section 4.4 was responsible for driving the changes in the North Atlantic overturning circulation (Fig. A.11). The latitude of the wind-stress curl over the south-east Indian Ocean controls the Indo-Atlantic volume and salt flux. The Indo-Atlantic salt flux in part determines the salinity of the North Atlantic surface waters: saltier surface waters lead to more convection and a stronger NADW overturning cell. Thus more equatorward winds lead to a reduced Agulhas leakage, a fresher North Atlantic with less convection and a reduced NADW overturning cell. The exact relationships shown in Figure A.11 differ somewhat from those for the CMIP3 winds shown in Figure 4.5, because of differences in the wind-ensembles, and because other wind-determined factors like Southern Ocean upwelling and atmospheric moisture transport also have an influence on NADW strength.

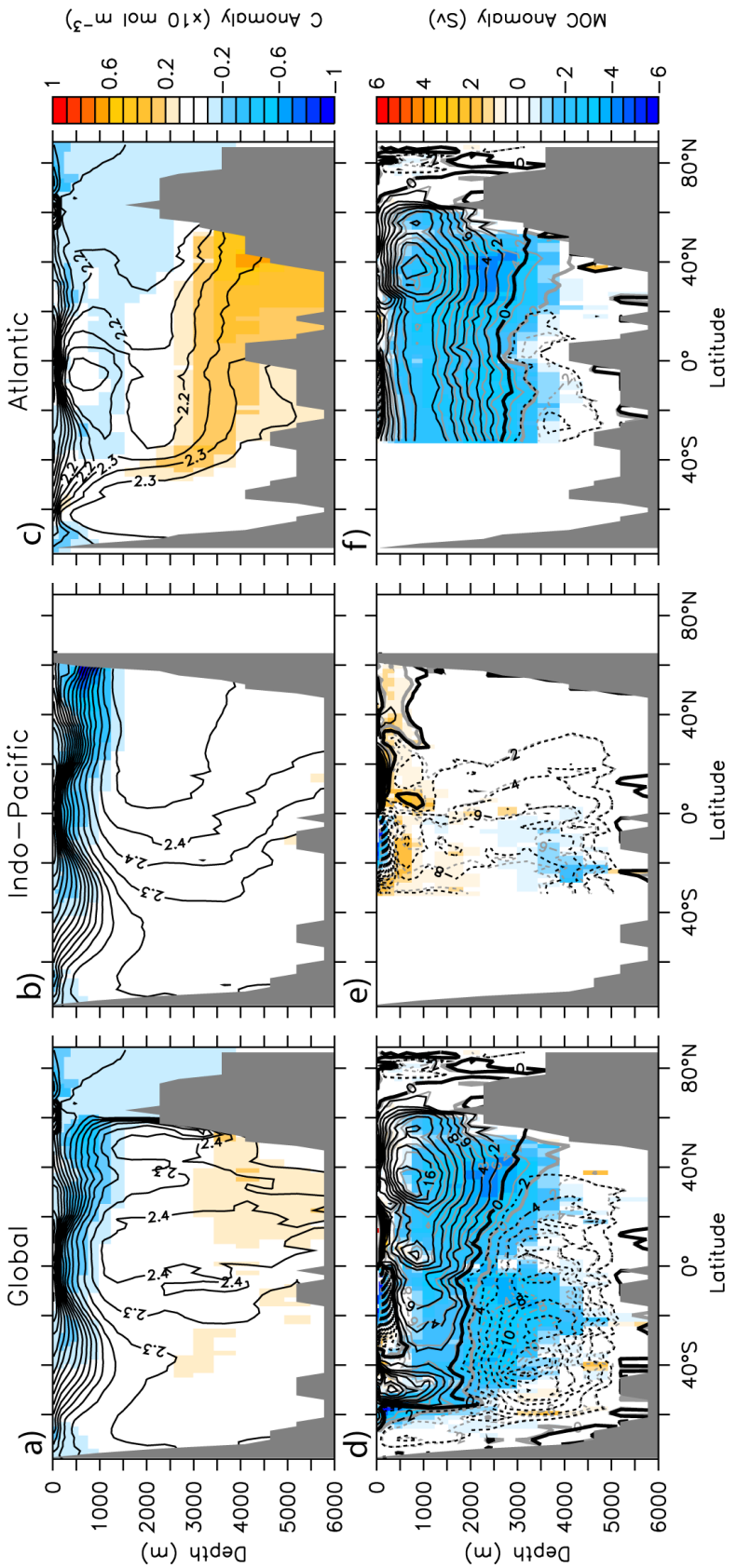

Figure 5.9: (a, b, c) The zonal mean of the variable GM experiment (E5) ensemble mean total ocean carbon in contours, with shading giving the anomaly relative to the R1 control (C3); (d, e, f) The ensemble mean MOC (Sv) is contoured in black, the R1 control MOC is contoured in grey, and their difference is given by the shading. All fields are averages over years 4900 to 5000, and zonal means are shown for the global ocean (a, d), the Indo-Pacific (b, e) and the Atlantic (c, f).

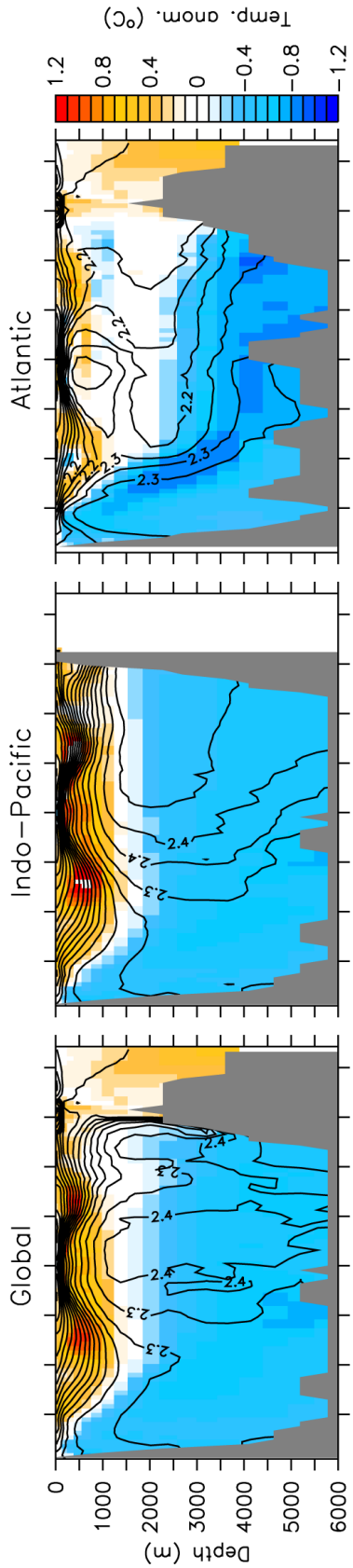

Figure 5.10: The zonal mean of the variable GM experiment (E5) ensemble mean temperature anomaly relative to the R1 control (C3). Temperatures are averages over years 4900 to 5000, and zonal means are shown for the global ocean, the Indo-Pacific and the Atlantic.

The Indo-Pacific carbon loss occurred from thermocline waters that are ventilated in the Southern Ocean (Fig. 5.9b). That is to say the total ocean carbon contours connect to the surface in the Southern Ocean (but also note that carbon is not a conservative tracer, but influenced by biology as noted above). The MOC streamfunction over the SO shows that the Deacon cell is intensified in the CMIP5 ensemble mean relative to the control. The CMIP5 winds drive a deepening of the thermocline, and a warming of the surface ocean by up to 1.2°C, which reduces its carbon storage capacity through solubility effects as described by Ito and Follows [2003]. For example, the 10°C isotherm is about 60 m deeper between 40°S and 40°N on average for the experiment ensemble mean, relative to the control. The thermocline deepening is likely driven by the stronger CMIP5 winds driving more northward Ekman transport and therefore increasing subduction to the north. Increased subduction increases the volume flux of thermocline waters, and without enhanced Northern Deepwater formation the thermocline deepens, as suggested by Gnanadesikan and Hallberg [2000]. The enhanced Ekman transport is partly compensated by enhanced eddies in the variable GM scheme, and therefore this effect is stronger in the regular GM experiment (not shown). The vertical redistribution of ocean carbon is thus likely forced by both solubility and biological pump mechanisms and the result for the CMIP5 winds is consistent with the idealized glacial wind cases described by d'Orgeville *et al.* [2010]. The redistribution of ocean carbon in these equilibrium experiments can influence carbon uptake during transient climate change simulations which use the equilibrium simulations as their initial condition, as we now explore.

5.5 Transient ocean carbon uptake under CMIP5 winds

5.5.1 Experiments

Transient runs were conducted for the period 1800–2005 under historical forcing and continued from 2006–2100 under the RCP4.5 forcing (see Meinshausen *et al.*, 2011 for details of the forcing). A transient control run (C2T) was initialized using the year 5000 fields of C2, and integrated subject to time-evolving forcing, but with all wind-components held fixed at the R1 wind-climatology used in C2. Similarly, a second transient control run (C3T) was produced using the variable GM coefficient, fixed R1

climatological winds and initialization from C3. Then, transient experiments were done subject to the same historical/RCP4.5 radiative forcing and using the fixed and variable GM schemes, and initialized from experiments E4 and E5 respectively. To separate the influences of pre-industrial wind-bias from transient wind-changes, each experiment was further divided into:

1. A fixed-wind experiment, with winds held at their pre-industrial climatology (E4Tf and E5Tf for the fixed and vK_{GM} respectively).

2. A time-evolving wind experiment with winds evolving in time from their pre-industrial climatology starting in 1871 (E4Te and E5Te for the fixed and vK_{GM} respectively).

The forcing evolved in time from 1800–2100, but time-evolving winds were only available from the year 1871 onwards, so I continued to use the pre-industrial wind climatologies over the period 1800–1870. This is a reasonable approach since the low levels of external forcing mean no significant trends are expected to occur in the wind forcing during this period. From 1871 onwards the CMIP5 time-evolving wind forcing was used for each ensemble member. The transient experiments are listed in Table 5.2 and a full map of the chapter's experimental design is shown in Fig. A.9. We start the next section by first considering the fixed wind experiments.

5.5.2 The influence of pre-industrial wind bias

In the first climate change simulation, the wind-forcing was held constant at the pre-industrial climatology, but the forcing evolved in time. Under the fixed GM scheme in experiment E4Tf, the ocean takes up around 375 Pg of carbon by 2100 in the experiments and the R1 control (Fig. 5.11a). The experiment ensemble mean takes up about 8 Pg more carbon than the control, with some ensemble members taking up around 30 Pg more (Fig. 5.11c).

The enhanced uptake in the experiment relative to the R1 control represents the "pre-industrial" wind bias effect on ocean carbon uptake. The magnitude of the bias is small relative to total ocean carbon uptake, representing about 2.5% for the ensemble mean, but nonetheless this uptake anomaly is statistically significantly different from zero at the 5% level (based on a one-sample t-test). The relative magnitude of the uptake bias for the ensemble mean (about 2.5%) is smaller than that found for the CMIP3 winds, using zonal-wind stress alone (Chapter 4), partly

Table 5.2: Transient experiments with historical/RCP4.5 forcing and fixed pre-industrial winds (top) or time-evolving winds (bottom, indicated by Δ). The name of the run, the source of the wind-fields, the GM scheme and the number of runs (#) are indicated. The Difference field shows how anomalies were computed for each experiment, and it is indicated in which Figure they are shown. Init. indicates which run the simulations were initialized with.

Name	τ_x	τ_y	w_s	w_a	v$K_{\rm GM}$	#	Difference	Figure
C2T	R1	R1	R1	R1	NO	1		
E4Tf	CMIP5	CMIP5	CMIP5	R1	NO	28	D6=E4Tf-C2T	Fig. 5.11c
C3T	R1	R1	R1	R1	YES	1		
E5Tf	CMIP5	CMIP5	CMIP5	R1	YES	28	D7=E5Tf-C3T	Fig. 5.11d
	$\Delta\tau_x$	$\Delta\tau_y$	Δw_s	w_a				
E4Te	CMIP5	CMIP5	CMIP5	R1	NO	28	D8=EeTe-C2T	Fig. 5.12c
E5Te	CMIP5	CMIP5	CMIP5	R1	YES	28	D9=E5Te-C3T	Fig. 5.12d

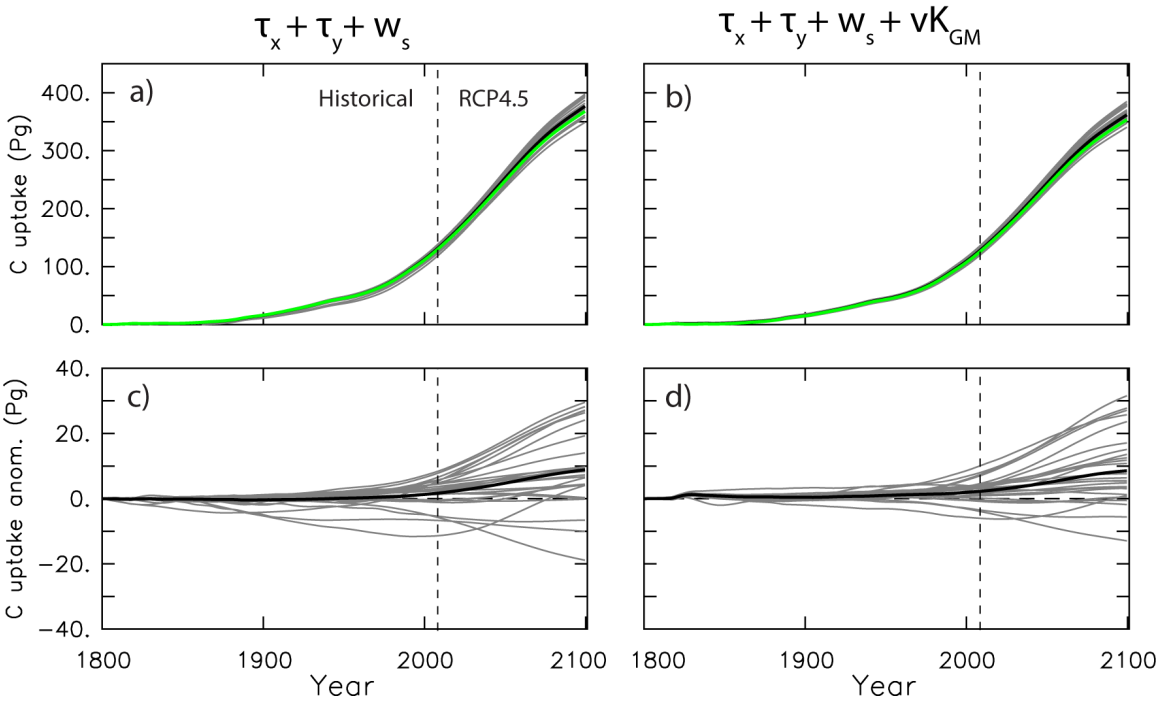

Figure 5.11: (a, b) Total ocean carbon uptake over 1800–2100 under historical/RCP4.5 forcing and fixed pre-industrial winds, shown for the a) regular (E4Tf) and b) variable (E5Tf) GM experiments; (c, d) total ocean carbon uptake anomaly in the experiments, relative to the R1 controls, C2T and C3T respectively. The black solid lines are the experiment ensemble mean, and the green lines are the respective controls.

because of the compensating effects of wind-speed on total equilibrium carbon storage described in the previous section. Though, the results are not directly comparable because of i) different climate forcing used (SRESA2 emissions in Chapter 4, vs. RCP4.5 CO_2 concentrations here), ii) different ensemble sizes and iii) different model and control winds.

Using the variable GM scheme in experiment E5Tf reduces total ocean carbon uptake in both the experiment and control, to around 355 Pg by 2100 (Fig. 5.11b). Because the reduction in total uptake is similar for the control and the experiment ensemble members, the uptake anomaly (Fig. 5.11d) remains close to that for the regular GM case. In other words, the pre-industrial wind bias effect on transient ocean carbon uptake is not significantly influenced by the representation of eddies, as argued in Chapter 4.

5.5.3 The influence of transient wind changes

In the transient wind experiments, the winds in the experiment ensemble members are allowed to time-evolve from 1871 to 2100, but the winds in the R1 control remain constant. Total ocean carbon uptake remains similar, but the uptake anomaly relative to the control appears slightly reduced in the regular GM experiment, E4Te, but nearly unchanged in the variable GM experiment, E5Te (Fig. 5.12). To highlight more clearly the difference between the transient and fixed wind experiments, the uptake anomaly (transient minus fixed) was computed (Fig. 5.13). For the regular GM experiment, the negative anomalies indicate that the transient wind simulations have less ocean carbon uptake than the fixed wind simulations (Fig. 5.13a). This represents the transient-wind (or climate change) induced saturation of the ocean carbon sink, as discussed by Le Quéré *et al.* [2010] and Sarmiento *et al.* [2010]. Examination of the surface flux anomalies show that the transient winds force a strong outgassing in the Southern Ocean between 40° and 50°S, which is the so called "saturation of the Southern Ocean CO_2 sink", here representing the effect from simulated, rather than observed winds [Le Quéré *et al.*, 2007; Lovenduski *et al.*, 2008].

The magnitude of the transient wind-effect on ocean carbon uptake was around 3 Pg for the ensemble mean of the regular GM experiment (and is significantly different from zero at the 5% level). Thus, under constant eddy diffusivity, the transient wind-effect has an influence about half the size of the pre-industrial bias effect already described. This confirms the prediction made in Chapter 4 that the pre-industrial

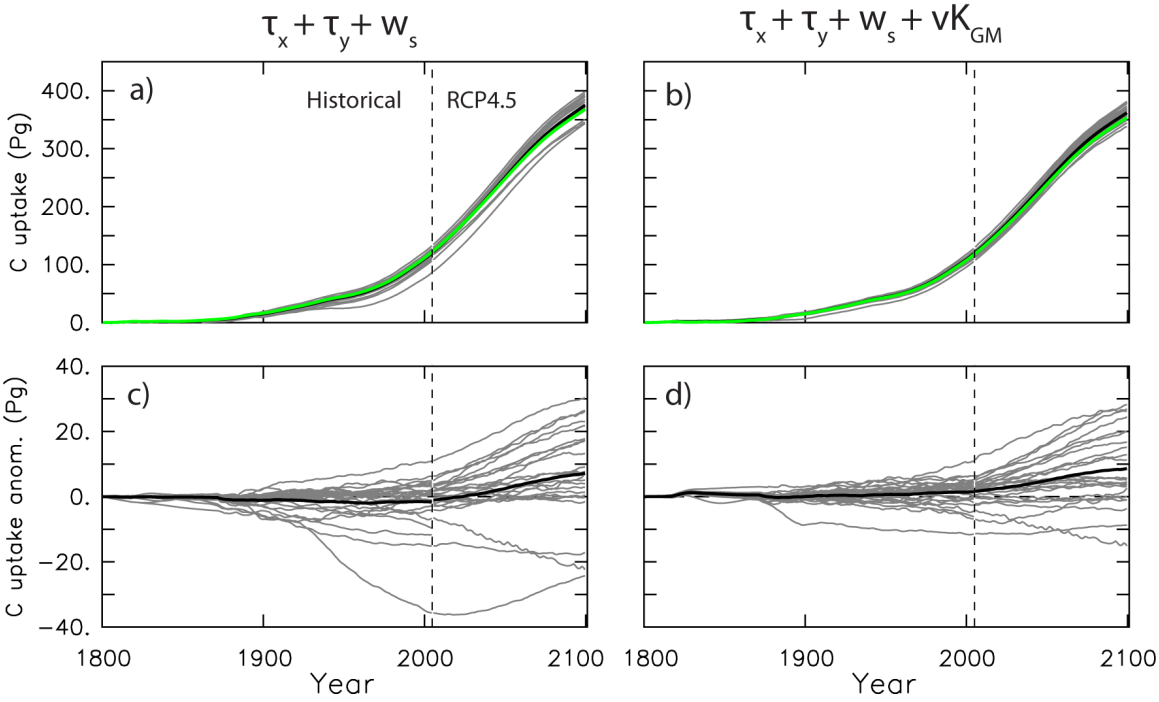

Figure 5.12: (a, b) Total ocean carbon uptake over 1800–2100 under historical/RCP4.5 forcing and time-evolving winds, shown for the a) regular (C4Te) and b) variable (C5Te) GM experiments; (c, d) total ocean carbon uptake anomaly in the experiments, relative to the R1 controls, C2T and C3T respectively. Note that the experiment ensemble size changes from 28 members during the historical period (1800–2005) to 24 members over the RCP period (2006–2100). The black solid lines are the experiment ensemble mean, and the green lines are the respective controls.

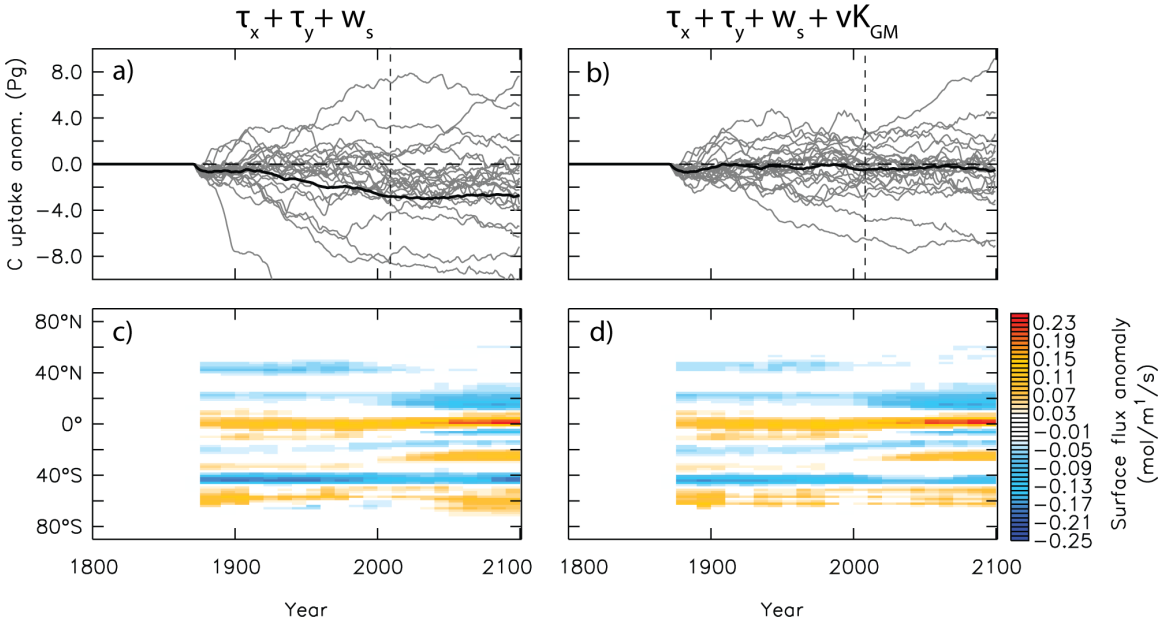

Figure 5.13: (a, b) Ocean carbon uptake difference between the time-evolving and fixed-wind experiments, shown for the a) regular and b) variable GM cases over 1800–2100; (c, d) zonally integrated surface CO_2 flux difference between the time-evolving and fixed-wind experiments over 1800–2100. Note time-evolving winds only begin in 1871, so anomalies prior to that date are zero. The difference in a) and c) is given by (E4Te - E4Tf) while the difference in b) and d) is given by (E5Te - E5Tf).

bias effect was the more significant. Under the variable GM scheme, the ocean carbon uptake difference between the transient and the fixed wind experiments is not significantly different to zero (Fig. 5.13b). The surface flux anomalies show that the variable eddy scheme has reduced the strong outgassing from the Southern Ocean (Fig. 5.13d). That is, under the variable GM scheme the eddies compensate the effect of increasing winds, and reduce that simulated saturation of the Southern Ocean CO_2 sink. This is an important finding, because previous studies on the Southern Ocean CO_2 sink using observed winds have not considered a variable eddy scheme [Le Quéré *et al.*, 2007; Lovenduski *et al.*, 2008].

Under the typical climate modelling strategy, where the end point of long pre-industrial control runs are used to initialize model fields for transient climate change simulations, the modelled ocean carbon uptake is sensitive to pre-industrial winds biases. In the experiments conducted here, this pre-industrial wind bias effect was significantly larger than the effect of time-evolving wind changes in the transient simulations, particularly when using a variable GM scheme. This finding is also

important for studies using ocean models to estimate carbon uptake using reanalysis-based forcing. These observational studies are likely similarly sensitive to even modest errors in the prescribed ocean carbon initial condition, typically taken from imperfect observations [e.g. Le Quéré *et al.*, 2010; Le Quéré *et al.*, 2007].

The CMIP5 climate models underestimate transient wind changes in the sensitive Southern Ocean region, relative to multiple reanalyses over the satellite era (Chapter 3), which implies the simulated transient wind effect examined here could be underestimated relative to that seen in the real ocean. However, because the variable GM scheme largely compensates for transient wind-induced circulation changes, the CMIP5 trend bias is unlikely to affect the general conclusion. To test this, transient simulations with time-evolving winds from 20CR.

5.6 Transient carbon uptake under 20CR winds

An additional set of experiments were done, similar to E4Te/f and E5Te/f, except using 20CR derived winds. That is, the atmospheric advective winds are based on the R1 climatology, but all surface wind components are derived from 20CR, and the runs were initialized from 5000-year spin-ups with the 20CR climatology computed over 1871–1889, as for the CMIP5 winds in experiments E4 and E5. The 20CR run with time-evolving winds and the regular GM scheme has about 4 Pg more ocean carbon uptake by year 2000 than the run with fixed pre-industrial winds (Fig. 5.14a). This is the opposite sense of the response to transient wind forcing seen in the CMIP5 models (Chapter 5), and in previous studies using ocean model driven by renalaysis winds [Le Quéré *et al.*, 2010; Le Quéré *et al.*, 2007; Lovenduski *et al.*, 2008]. There is a considerable outgassing anomaly, intensifying with time near 50°S in the Southern Ocean, in the 20CR transient run relative to the fixed winds run (Fig. 5.14c). However, this transient wind-driven Southern Ocean outgassing anomaly is more than compensated for by ingassing anomalies to the north in the Southern Ocean, and particularly near 40°N. The strong ingassing near 40°N occurs in the western North Pacific (Fig. 5.15a) and is driven by strong transient wind changes that occur in that region in 20CR (Fig. 5.15b). A similar pattern is observed under NCEP/DOE Reanalysis 2 (R2) and satellite derived winds by Le Quéré *et al.* [2010, see their Figure 4]. This feature appears to be driven by the intensifying and poleward shifting westerly-wind jet in the Northern Hemisphere [e.g. Wang *et al.*, 2006], similar to the changes in the Southern Hemisphere jet discussed in Chapter 3,

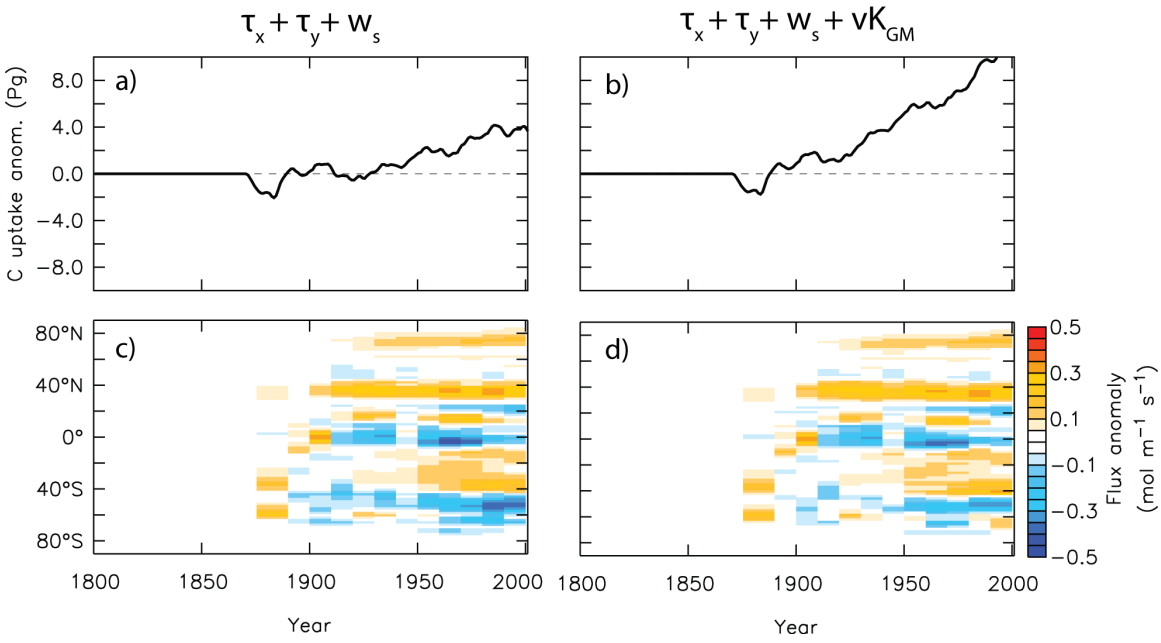

Figure 5.14: (a, b) Ocean carbon uptake difference between the time-evolving and fixed-wind runs using 20CR winds, shown for the a) regular and b) variable GM cases over 1800–2005; (c, d) zonally integrated surface CO_2 flux difference between the time-evolving and fixed-wind runs over 1800–2000. Note time-evolving winds only begin in 1871, so anomalies prior to that date are zero.

but this requires further investigation.

Thus, using the UVic model forced by 20CR winds I simulate an intensification of the net ocean carbon sink over the 20th century, not a weakening as simulated by other studies using time-evolving NCEP/NCAR Reanalysis 1 (R1) forcing [Le Quéré *et al.*, 2007; Lovenduski *et al.*, 2008]. This occurs under the regular GM scheme even though the 20CR winds do cause a tendency for "saturation" of the Southern Ocean CO_2 sink in the words of Le Quéré *et al.* [2007]. Thus it appears that trends in the ocean carbon sink are sensitive to the product chosen to force the ocean model, as noted in [Le Quéré *et al.*, 2010]. The previous studies cited used surface buoyancy forcing from R1, whereas in my simulations the surface buoyancy forcing was computed by the UVic model, which is one major difference between the studies (besides the wind forcing), the other being the model initialization. Further investigation is needed to determine whether the wind (and resulting carbon flux trends) seen in 20CR over the western north Pacific are reliable. Indeed, a rigorous model intercomparison project forced by climate changes from across the different reanalysis products is required to

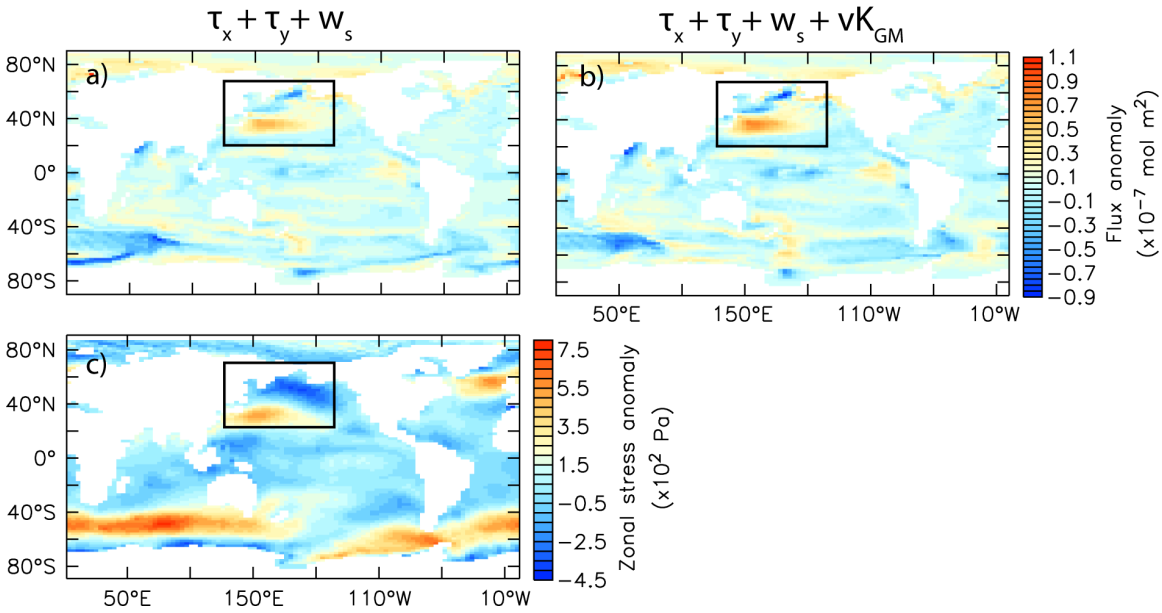

Figure 5.15: (a, b) The surface flux difference between the run using time-evolving 20CR winds, and the run using fixed pre-industrial 20CR winds for the a) regular and b) variable GM; (c) the zonal wind-stress anomaly at year 2000 between run with transient 20CR winds and the runs with wind fixed at the pre-industrial climatology. The boxes show the region of interest in the western North Pacific.

constrain the uncertainty in historical ocean carbon uptake trends, but this is beyond my scope here.

Under the variable GM scheme, the saturation of the Southern Ocean CO_2 sink is reduced (Fig. 5.14d), and under 20CR transient winds this allows even greater intensification of the net global ocean CO_2 sink (Fig. 5.14b), forced mainly by the uptake in the western north Pacific. Thus it appears the choice of eddy parameterization, not explicitly considered in previous studies [Le Quéré *et al.*, 2007; Le Quéré *et al.*, 2010; Lovenduski *et al.*, 2007; Lovenduski *et al.*, 2008], can significantly influence the conclusions on the influence of wind-induced climate change feedbacks on the ocean carbon sink. With these conclusions on ocean carbon uptake, we now briefly consider the potential influence of the winds on other aspects of the climate system.

5.7 The influence of wind-changes on other aspects of the climate system

The CMIP5 pre-industrial wind biases caused changes to the residual overturning circulation in the Southern Ocean, the dynamics of the Agulhas leakage, and the global overturning circulation, as we saw in Section 5.4. Changes in the simulated winds over the 20th and 21st centuries, notably in the Southern Hemisphere westerlies, also influenced the dynamics of the Southern ocean circulation and surface carbon fluxes. In addition to these wind-influences on the ocean circulation, the time-evolving CMIP5 winds had a significant influence on Southern Hemisphere sea-ice area, which we briefly explore now (but see Section 6.2 for details on the data and the sea-ice area calculation).

Satellite observations show the Southern Hemisphere sea-ice area to have increased by a small but statistically significant amount since 1979, but the vast majority of CMIP5 models simulate a significant decline in sea-ice over the same period (see Fig. 5.16 and Chapter 6). Wind-changes have been identified as an important driver of observed regional Antarctic sea-ice trends [Holland and Kwok, 2012]. Here I compare sea-ice area in the UVic model with variable GM, between the experiments with time-evolving CMIP5 derived winds and the fixed pre-industrial winds.

The experiment using time-evolving winds does an excellent job of reproducing the large sea-ice loss simulated by the original CMIP5 models (Fig. 5.16). This provides a validation of the ability of the UVic model to simulate sea-ice processes occurring in the CMIP5 ensemble. The experiment using CMIP5 winds fixed at their pre-industrial level loses significantly less sea-ice over the 20th and 21st centuries. These experiments indicate that the time-evolving wind changes in the CMIP5 models cause additional Southern Hemisphere sea-ice loss, relative to simulations with fixed winds. This is a surprising result, since time-evolving wind changes have been proposed as a mechanism to explain the observed Southern Hemisphere sea-ice gain [e.g. Holland and Kwok, 2012]. The CMIP5 Southern Hemisphere wind-biases, and the underestimation of simulated wind-trends documented in Chapter 3 may be contributing to the disagreement between the simulated and observed sea-ice trends. Alternatively, missing forcing in the CMIP5 models could play a role, as is explored in the following chapter.

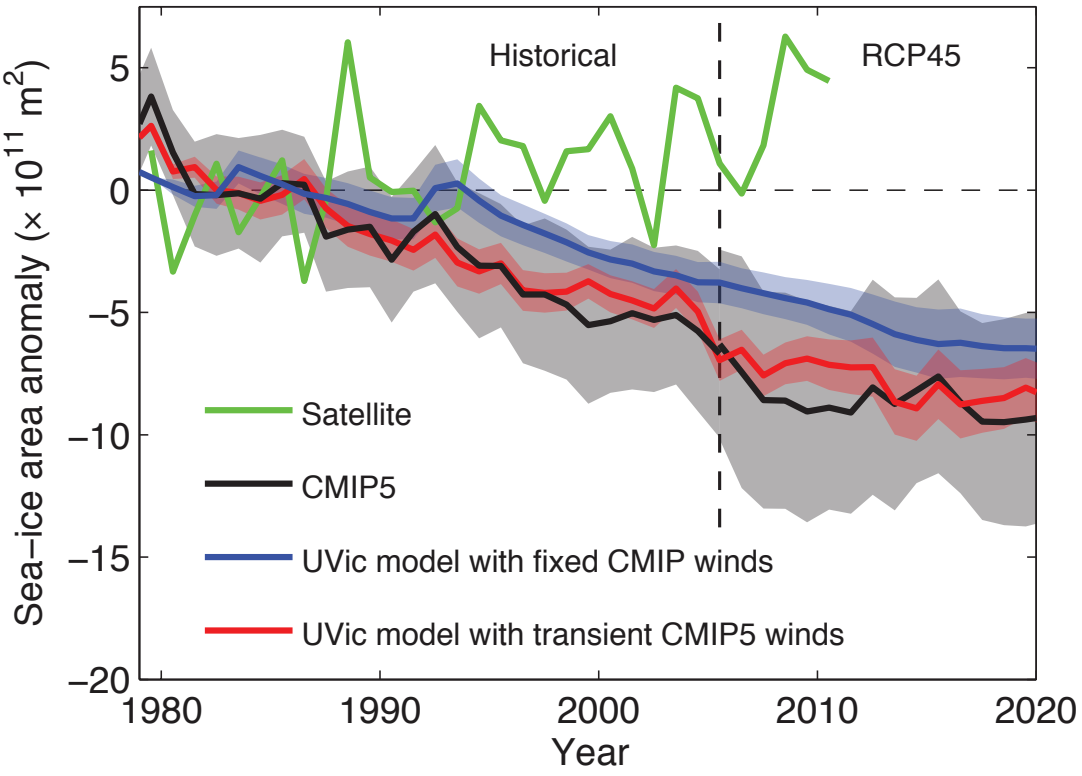

Figure 5.16: The Southern Hemisphere sea-ice area anomaly relative to the 1979–1989 base period, from the run 1 of 34 original CMIP5 models (black), and from the UVic model forced with CMIP5 winds that are fixed at their pre-industrial level (blue) and that evolve in time (red); also shown is the observed satellite sea-ice area from NSIDC using the NASATEAM algorithm. For model simulations the solid lines show the ensemble mean, and the envelopes give the 95% confidence interval.

5.8 Conclusions

There are several key conclusions to draw from this chapter:

1. The CMIP5 pre-industrial winds have biases, particularly in the region of the Southern Hemisphere westerlies, extending the conclusions of a satellite-era bias in Chapter 3.

2. The CMIP5 SH westerly jets show a strengthening and poleward shift in time in response to anthropogenic forcing over the 20th Century, but these trends are underestimated relative to reanalyses. This extends the conclusion of Chapter 3 that the models underestimate the strength trend over the satellite era.

3. The pre-industrial wind-biases vertically redistribute ocean carbon in "pre-industrial control" simulations.

4. When using a regular GM scheme the wind biases significantly reduce total ocean carbon storage, but when using a variable GM scheme the wind biases do not change the ocean carbon storage significantly.

5. The pre-industrial wind bias significantly increases ocean carbon uptake in transient climate change simulations, through the bias in the ocean carbon distribution introduced in the initialization of the transient simulations.

6. Simulated time-evolving wind changes over the 20th and 21st centuries significantly decrease ocean carbon uptake when using a regular GM scheme for eddy parameterization, but not when using a variable GM scheme.

7. The 20CR transient wind-changes increase ocean carbon uptake in the UVic model, in contrast to the CMIP5 model winds, and previous studies using R1 forcing.

8. The time-evolving winds simulated by the CMIP5 models tend to increase Southern Hemisphere sea-ice loss, relative to simulations with fixed winds.

Chapter 6

The influence of recent Antarctic ice-sheet retreat on sea-ice area trends

This chapter is based on the contents of the paper:

N. C. Swart and J. C. Fyfe [2013], The influence of recent Antarctic ice-sheet retreat on sea-ice area trends, *Geophys. Res. Lett.*, (submitted)

6.1 Introduction

Various mechanisms have been proposed to explain the observed increase in Antarctic sea-ice area since 1979 (Fig. 6.1, green curve) including freshening of the surface Southern Ocean from precipitation [Liu and Curry, 2010] and ocean-sea-ice feedbacks [Zhang, 2007]. In particular, wind changes have been identified as an important driver of regional Antarctic sea-ice trends [Holland and Kwok, 2012], though the respective roles of internal variability and anthropogenic forcing in driving these wind-induced trends is unclear [Bitz and Polvani, 2012; Sigmond and Fyfe, 2010; Turner *et al.*, 2009]. Fresh-water forcing of the surface Southern Ocean is known to drive sea-ice growth [Swingedouw *et al.*, 2008; Aiken and England, 2008; Stouffer *et al.*, 2007], but the effect of recently observed dynamic mass loss from the Antarctic Ice Sheet (AIS) [Rignot *et al.*, 2011; King *et al.*, 2012; Shepherd *et al.*, 2012] has not been quantified.

The dynamic mass loss from the AIS is thought to be caused, at least partly, by the strengthening of the Southern Hemisphere westerly winds [Pritchard *et al.*, 2012]. Stronger westerlies drive more upwelling of comparitively warm Circumpolar Deep Waters into proximity with the Antarctic shelf. When brought into contact, the warm CDWs drive basal melting of marine ice sheets, reducing their buttressing capacity and ultimately leading to the acceleration of Antarctic glaciers [Joughin *et al.*, 2012; Pritchard *et al.*, 2012]. Simulating these mechanisms requires a coupled dynamic ice sheet model, ubiquitously absent from the climate models simulations contributed to CMIP5.

The CMIP5 multi-model ensemble mean shows a significant decline in Antarctic sea-ice (Fig. 6.1, black curve) given time-evolving changes in ozone (tropospheric and stratospheric), greenhouse gases, aerosols (sulphate, black carbon and organic carbon), land use (e.g., deforestation), solar variability and volcanic activity. I hypothesize that the discrepancy between the CMIP5 ensemble-mean and observed sea-ice area trend is due, at least in part, to unaccounted for mass loss from the AIS in the CMIP5 models. To test this hypothesis I employ the UVic Earth System Climate Model to quantify the impact of observationally constrained ice-sheet derived freshwater forcing on Antarctic sea-ice area trends since 1979. I then rigorously test the consistency between the observed and simulated sea-ice trends, and the potential influence of the fresh-water effect.

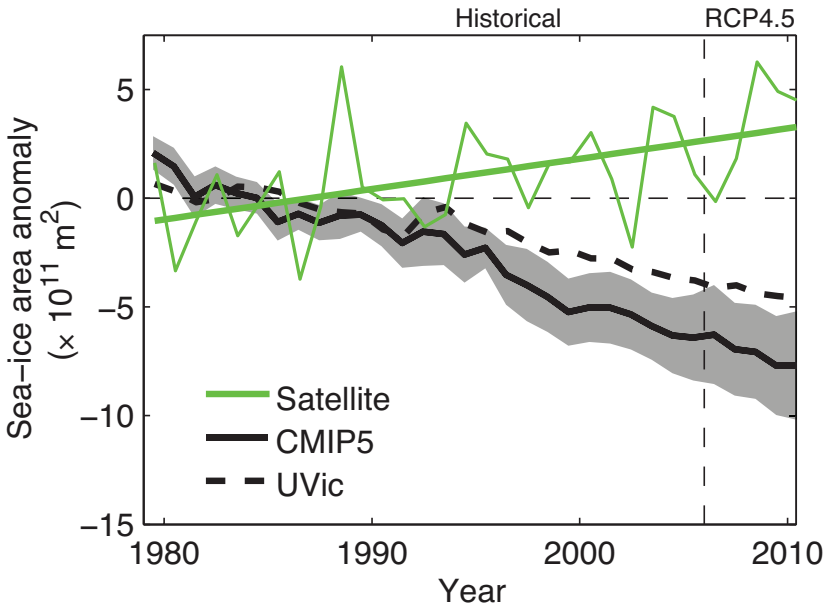

Figure 6.1: Antarctic sea-ice area anomaly relative to the 1979–1989 mean, for satellite observations using the NASATEAM algorithm, the ensemble-mean of 38 CMIP5 models (with a total of 135 realizations), with the envelope indicating the 95% confidence interval, and the UVic model. The thick green curve is the linear least-squares fit to the observed anomalies.

6.2 Data and methods

I use the monthly sea-ice fraction from the historical and RCP4.5 continuation simulations of 38 CMIP5 models, including all available realizations, [Taylor *et al.*, 2011] archived by the Program for Climate Model Diagnosis and Intercomparison (PCMDI– see Appendix A.8). I compute annual-mean sea-ice area as the area-integrated sea-ice fraction over all grid cells with a sea-ice fraction of greater than 15%, and I compute linear least-squared trends over the period 1979–2010. The satellite sea-ice area data is the updated NASA TEAM monthly total Antarctic sea-ice area provided by the National Snow and Ice Data Centre [Stroeve, 2003].

To investigate the influence of freshwater (FW) forcing I employ the University of Victoria Earth System Climate Model (UVic-ESCM) version 2.9 [Weaver *et al.*, 2001, see Appendix A.5 for the model descrpition]. Here the model uses a fixed wind climatology derived from the 20th Century Reanalysis [Compo *et al.*, 2011]. The version of the model that I use is very similar to that used in the recent model intercomparison of Eby *et al.*, 2013, except that I have updated the Gent-McWilliams eddy parameterization [Gent *et al.*, 1995; Gent and McWilliams, 1990] to have a variable coefficient in the same manner as described in Gnanadesikan *et al.* [2006] and Saenko [2012] and Chapter 5. All of the simulations were initialized from a multi-centennial spin-up, and integrated using historical natural and anthropogenic forcing from 1800 to 2005 and RCP4.5 scenario forcing thereafter [Meinshausen *et al.*, 2011]. Forced in this way the UVic ESCM shows a decline in Antarctic sea-ice area (Fig. 6.1, black dashed curve) that is less than in the CMIP5 simulations, because the wind-forcing has been held fixed (c.f. Fig. 5.16; and note the CMIP5 envelope is smaller here because all available model realizations (135) are used in the averaging here).

6.3 Sea-ice response to ice-sheet mass loss

Several recent studies using surface mass balance and gravimetry have concluded that the Antarctic Ice Sheet as a whole has been losing mass since about 1992 [Rignot *et al.*, 2011; King *et al.*, 2012; Shepherd *et al.*, 2012]. These losses predominantly occur from the West Antarctic Ice Sheet (WAIS), which is estimated to have been losing mass regionally since about the early 1970's [Rignot *et al.*, 2008]. The vast majority of this mass loss is thought to be the result of dynamic losses from the retreat of marine

ice sheets [Joughin *et al.*, 2012; Pritchard *et al.*, 2012; Rignot *et al.*, 2011]. The observed dynamic ice-sheet mass losses imply a flux of fresh water into the Southern Ocean, and significant freshening of the waters surrounding Antarctica is indeed well documented [Purkey and Johnson, 2013; Jacobs and Giulivi, 2010; Jacobs *et al.*, 2002; Rintoul, 2007].

In order to span the range of the significant observational uncertainties in the absolute magnitude of ice-sheet mass loss (Fig. 6.2a), as well as in the timing of mass loss initiation, I conducted two ensembles of experiments using the UVic ESCM: 1) a WAIS ensemble with 5 different rates of mass loss acceleration, and in which forcing begins in 1974, and 2) an AIS ensemble with ten different rates of acceleration, and with forcing initiation in 1992 (see Appendix A.8). In each simulation the fresh water flux equivalent to the mass loss is evenly distributed across the UVic ESCM ocean surface grid cells adjacent to Antarctica. The experiment without such fresh water forcing is used as a control.

The ice-sheet derived FW forcing reduced simulated sea-ice loss over the historical period, relative to the control (Fig. 6.2). The freshwater forcing acts to stabilize the Southern Ocean stratification, thereby reducing the vertical oceanic heat flux and sea-ice basal melt which leads to sea-ice growth, as previously documented [Bintanja *et al.*, 2013; Aiken and England, 2008; Stouffer *et al.*, 2007; Hellmer, 2004].

However, even the strongest rates of FW forcing I applied could not reverse the negative sea-ice trend induced by the radiative forcing. Sea-ice area loss was reduced by 64% by 2020 relative to the control in the strongest case of the AIS ensemble (Fig. 6.2c). But for the FW scenario closest to observed rates of mass loss (AIS3, Shepherd *et al.* [2012]), sea-ice loss was only reduced by 11% relative to the FW control in 2020. For the WAIS ensemble with an earlier onset, sea-ice loss was reduced by between 6 and 50%, with the lower end forcing scenarios being the most observationally consistent.

If we consider linear-least squared trends, the FW forcing reduced the negative sea-ice trend relative to the control by 0.09–0.84×10^{11} m^2/decade for the WAIS ensemble, and 0.08–0.78×10^{11} m^2/decade for the AIS ensemble over the period 1979–2010. In the more strongly forced cases this is a large effect relative to the magnitude of the linear trend in observed sea-ice area of $1.39 \pm 0.82 \times 10^{11}$ m^2/decade (95% confidence interval accounting for serial correlation), but for the more observationally realistic low end cases the effect is small.

I have thus quantified the potential for Antarctic ice-sheet mass loss to influence

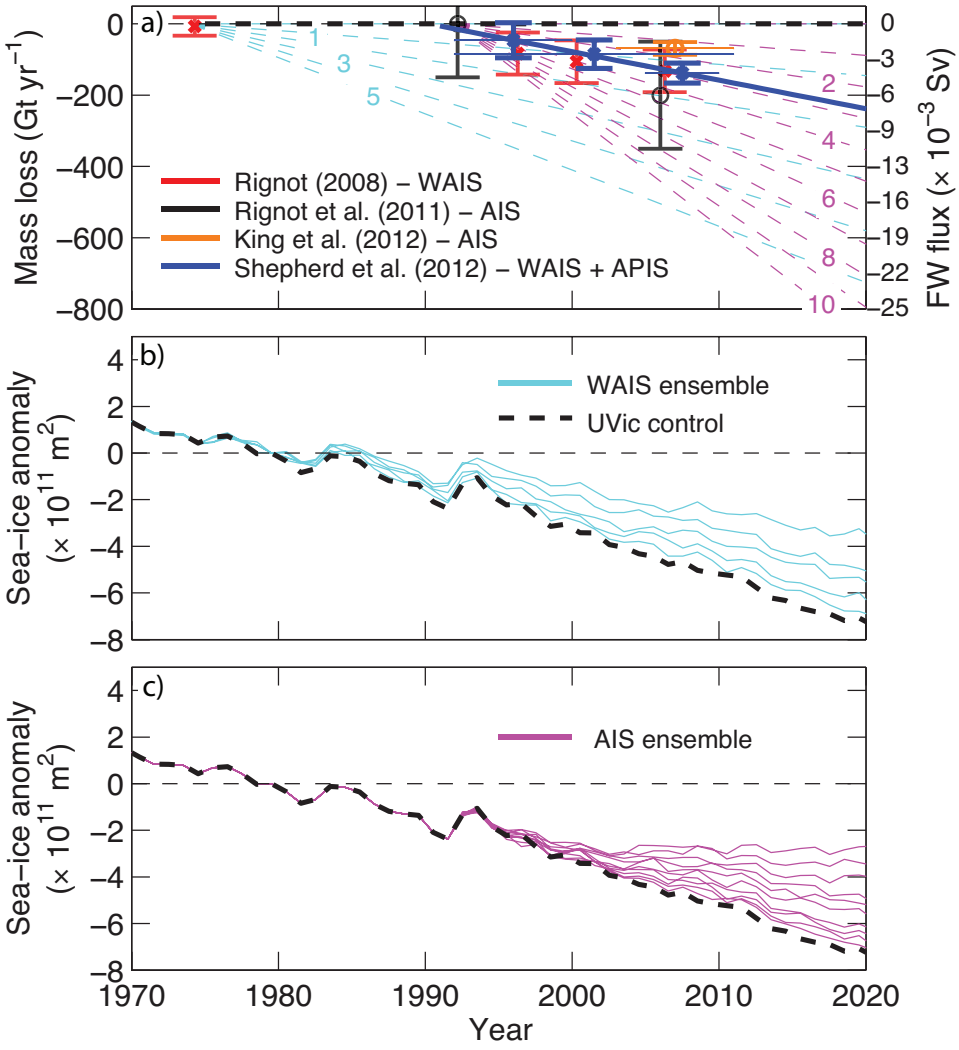

Figure 6.2: (a) Antarctic ice-sheet mass balance from several recent published estimates. Vertical error bars represent published rates of uncertainty in mass balance, and horizontal lines indicate the period over which the mass balance was estimated. The ensembles of cyan and magenta dashed lines show the equivalent rates of freshwater forcing applied to my model. (b,c) The Antarctic sea-ice area anomaly relative to 1979–1989 for experiments forced with freshwater input around Antarctica simulating ice-sheet mass loss for the ensemble of (b) five rates of WAIS mass loss acceleration and (c) ten rates of AIS mass loss acceleration.

sea-ice area trends over the historical period by using idealized freshwater forcing experiments in the UVic ESCM. For observationally consistent rates of mass loss, the effect on sea-ice area trends is small.

Since ice sheet dynamics are not represented in the CMIP5 models, Bintanja *et al.* [2013] suggested the dynamic ice-sheet derived FW forcing could influence the simulated sea-ice area trends. There are large internal variability and model response uncertainties associated with Antarctic sea-ice trends [Turner *et al.*, 2012], and so to address the relative importance of ice-sheet induced freshwater forcing amidst these uncertainties we return to the CMIP5 multi-model ensemble.

6.4 Implications for the CMIP5 multi-model ensemble

The CMIP5 multi-model ensemble-mean shows a large negative annual-mean sea-ice area trend over the historical period (Fig. 6.1, black curve). However, the histogram of sea-ice area trends shows that there is an extremely large spread across the individual members of the CMIP5 ensemble (Fig. 6.3). The trends span an order of magnitude from -16.0 to 2.7×10^{11} m^2/decade. The spread of trends reflects a difference in the response to historical forcing between models, and the influence of internal variability within individual models runs. This internal variability must be accounted for when comparing simulated and observed trends.

We can use the distribution of sea-ice trends across the individual members of the CMIP5 ensemble, to quantify the likelihood of simulating the observed positive sea-ice trend. Internal variability is taken into account using multiple realizations from each model, where available. A test of the null hypothesis that the CMIP5 ensemble mean and observed sea-ice area trends are equal can be done by making the assumption that the model trends are exchangeable and using a Monte-Carlo based resampling technique to construct an empirical distribution for the model trends [Fyfe *et al.*, 2013, and see Appendix A.8.1 for details on the technique]. Then, this empirical distribution can be used to determine whether the observed trend falls within the 5 to 95% range of individual model trends, where internal-variability in the models has been taken into account.

Under the assumption that the models are exchangable, the null hypothesis that the model mean and observed trends are equal is just accepted at the 10% significance

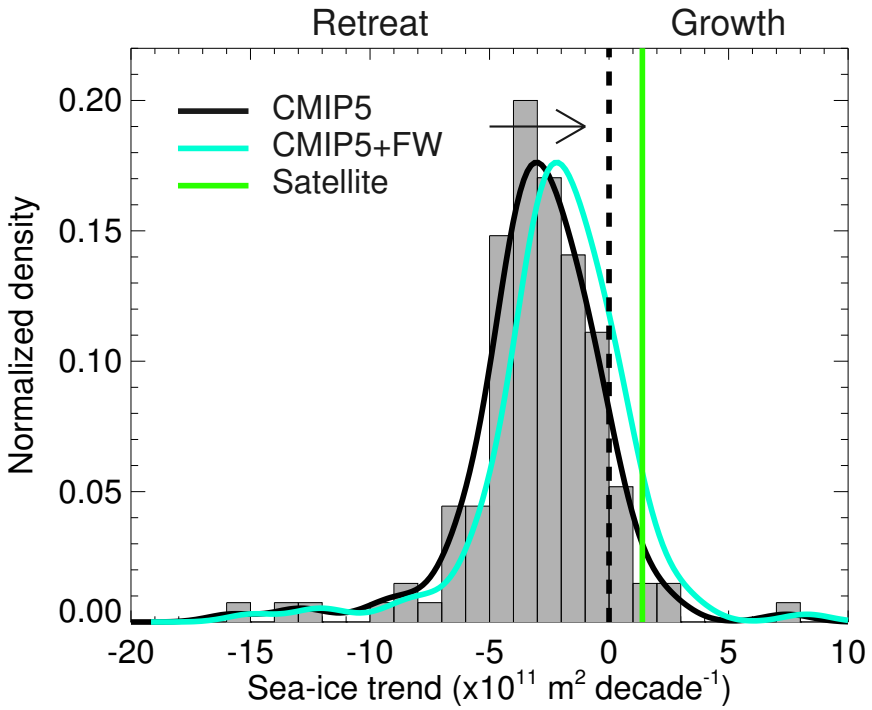

Figure 6.3: The distribution of linear sea-ice-area trends from the CMIP5 models over 1979–2010 (bars), with a Gaussian kernel estimate of the distribution (solid black); also shown is the distribution uniformly shifted towards positive values by the magnitude of the strongest version of the fresh-water effect (cyan); the green solid-line shows the trend from satellite observations.

level ($p = 0.051$). Thus it appears in this test using all available models, and accounting for internal variability, that the area integrated CMIP5 model sea-ice trends are just marginally statistically consistent with the observed trend.

The FW forcing effect quantified earlier using the UVic ESCM is small relative to the CMIP5 trends, but could systematically shift the model trends closer to the observations. To illustrate the maximum potential impact, I add the positive sea-ice area trend anomaly caused by the largest FW forcing (WAIS5) in the UVic ESCM to the CMIP5 trend distribution (Fig. 6.3). After positively shifting the CMIP5 trend distribution by 0.84×10^{11} m^2/decade to account for the strongest FW effect I tested, the null hypothesis that the model mean trend and observed trend are equal is accepted at the 10% significance level, with a small change in the p-value ($p = 0.064$) indicating that the FW forcing makes the area-integrated model trends more consistent with the observed trend. Thus, accounting for the FW effect makes the area-integrated Antarctic sea-ice trends simulated by the CMIP5 models slightly more consistent with the observed trend, but the effect is small.

6.5 Discussion and conclusions

I have quantified the effect of fresh water forcing of the surface Southern Ocean from dynamic mass loss from the Antarctic Ice Sheet. Bintanja *et al.* [2013] have recently suggested that this fresh water forcing could significantly influence Antarctic sea-ice area trends. However, they only considered a single, constant rate of fresh water forcing of 250 Gt yr^{-1} applied for 40 years. The recently reconciled observational estimates suggest a lower, but accelerating rate of mass loss and fresh-water forcing [Shepherd *et al.*, 2012]. In my experiments, which have an accelerating rate of fresh water forcing consistent with the reconciled observational estimates, there is only a small influence on simulated historical sea-ice trends, with a reduction in ice area loss of about 10%.

The evolution of Antarctic sea-ice over the recent decades has strong regional patterns and is strongly influenced by wind-forcing [Holland and Kwok, 2012; Simpkins *et al.*, 2012; Lefebvre and Goosse, 2008; Liu *et al.*, 2004]. In this investigation I only considered the area-integrated sea-ice trend, and I also held the winds fixed to isolate the FW forcing effect. Including time-evolving CMIP5 winds enhances sea-ice loss, as shown in Chapter 5.

The ice-sheet derived freshwater forcing is also likely to have a strong regional

pattern, with the major source of forcing in the West Antarctic [Rignot *et al.*, 2008]. My simulations indicate the sea-ice response to a surface fresh-water flux adjacent to Antarctica, but in reality the ice-sheet fresh water flux could be injected somewhat northward into the Southern Ocean by icebergs [Silva *et al.*, 2006], and is likely input at depths of up to several hundred meters where basal ice-sheet melt occurs [Joughin *et al.*, 2012].

The standard sea-ice component of the UVic model used here is based on a zero layer thermodynamics model, and has only two categories (ice or open water) [Weaver *et al.*, 2001]. Using a more sophisticated sea-ice component, which includes an ice-thickness distribution model and multilayer thermodynamics as in [Bitz *et al.*, 2001], will affect the ocean surface salinity, heat fluxes, ice-thickness and sea-ice growth rates and thus could influence the magnitude of the results presented here. I note however that the standard sea-ice configuration of the UVic model does reproduce the sea-ice trends seen in the original CMIP5 models, when time-evolving wind forcing is applied (Fig. 5.16). The regional pattern of sea-ice response to inhomogeneous freshwater forcing, the additive influence of transient-wind changes and choice of sea-ice model are topics requiring further research.

The absence of freshwater forcing from dynamic ice-sheet mass loss is a feature of the CMIP5 ensemble. The CMIP5 multi-model ensemble mean produces a negative sea-ice area trend in contrast to the observed positive trend. However, my statistical test which accounts for internal variability and uses all available CMIP5 runs suggests the CMIP5 sea-ice area trends are consistent with the observed trend at the 10% significance level. I have shown that the additional effect of dynamic ice sheet derived freshwater forcing, with a magnitude constrained by observations, has little effect on Antarctic sea-ice trends simulated by the CMIP5 models over the historical period.

Chapter 7

Thesis Conclusions

Drawing together the key conclusions from Chapters 3 through 6, I have shown that

1. The Southern Hemisphere westerlies simulated by the CMIP3 and CMIP5 models have systematic biases in their climatologies over the pre-industrial and satellite eras, relative to reanalyses. The models simulate a strengthening of the westerlies over the 20th and 21st centuries, but the simulated trends are underestimates over the satellite era relative to some reanalyses.

    - There is no fully-reliable observationally based estimate of the pre-1950 global wind-field. This restricts our ability to run model simulations to constrain the behaviour of the ocean carbon cycle over the 20th century, and to fully constrain climate model biases.

2. The climate model pre-industrial wind-bias in a coarse resolution model:

    - significantly reduces the carbon content of the simulated pre-industrial ocean, relative to simulations using observationally based winds, when using a constant eddy diffusivity.
    - does not significantly change the simulated pre-industrial ocean carbon content when using a variable formulation for the eddy diffusivity.
    - significantly influences the simulated vertical and horizontal distribution of carbon within the pre-industrial ocean under either a constant or a variable eddy diffusivity.

.

3. The pre-industrial bias effect influences simulations of historical and future ocean carbon uptake.

    - This occurs because the pre-industrial control runs are used to initialize transient climate change simulations, thereby introducing a bias into the initial conditions.
    - The effect of the pre-industrial wind-bias on ocean carbon uptake is a relatively small fraction of total ocean carbon uptake (around 2.5% by 2100 for the ensemble mean, but up to 10%).

4. Time-evolving changes in the Southern Hemisphere westerlies may not significantly feedback on the ocean-carbon cycle.

    - For the CMIP5 model winds used in my experiments, the effect of the pre-industrial bias was larger than the effect of transient wind changes.
    - When introducing a variable coefficient of eddy diffusivity into the Gent-McWilliam eddy parameterization scheme, the effect of simulated transient wind changes was near zero. This occurred because with variable eddies, the in and out-gassing regions of the Southern Ocean largely compensate for each other.
    - The CMIP5 models underestimate wind-changes relative to reanalyses, which could affect this conclusion. However, a similar effect was seen in simulations using the 20th Century Reanalysis version 2 winds. This reanalysis based simulation also showed enhanced net ocean carbon uptake due to transient wind-forcing, in contrast to previous studies using different reanalysis forcing products [Le Quéré *et al.*, 2010; Lovenduski *et al.*, 2008].

5. Fresh water forcing from recent dynamic Antarctic Ice Sheet mass loss works to increase sea-ice area.

    - Observationally constrained rates of ice-sheet derived fresh-water forcing drive a positive trend in sea-ice area in idealized simulations with the UVic model, relative to simulations with no fresh water forcing.
    - The fresh-water forcing is not represented in the CMIP5 models, which have large negative sea-ice area trends on average, in contrast to the observed positive trend. But the effect of the fresh water forcing on the

CMIP5 sea-ice area trends is small over the historical era, and cannot reconcile the CMIP5 ensemble mean trend with the observations.

- A statistical test indicates that the difference in historical sea-ice area trends between the CMIP5 ensemble mean and observations could simply be due to internal climate variability.

Appendix A

Additional Information

A.1 Transformed Eulerian Mean

The steady-state, zonally averaged momentum and buoyancy equations (following Vallis [2006] and Nikurashin and Vallis [2011]) can be written as

$$-f\overline{v} = -\frac{\Delta p}{L_x} - \frac{\partial}{\partial y}\overline{u'v'} + \frac{\partial \overline{\tau}}{\partial z} \tag{A.1}$$

$$\overline{v}\frac{\partial \overline{b}}{\partial y} + \overline{w}\frac{\partial \overline{b}}{\partial z} + \frac{\partial}{\partial y}\overline{v'b'} + \frac{\partial}{\partial z}\overline{w'b'} = \overline{S} \tag{A.2}$$

The eddy terms in equations (A.1) and (A.2), play a leading order role in the dynamical balances of the Southern Hemisphere mid-latitude ocean and atmosphere. The two equations themselves are dynamically linked through the thermal wind balance

$$f\frac{\partial \overline{u}}{\partial z} = -\frac{\partial \overline{b}}{\partial y} \tag{A.3}$$

where $\overline{u}$ is the Eulerian mean zonal velocity. It remains unclear whether the eddy momentum or buoyancy flux (or both) influence the mean zonal flow and stratification [Vallis, 2006]. The transformed Eulerian mean (TEM) approach addresses this issue by removing the effects of eddies from the buoyancy equation and collecting them in a simple expression in the momentum equation. The total, or residual, streamfunction is expressed as the sum of the Eulerian mean streamfunction and eddy induced streamfunction

$$\Psi^{\dagger} = \overline{\Psi} + \Psi^{*} \tag{A.4}$$

To do so we first separate the eddy buoyancy fluxes in (A.2) into the along-$\overline{b}$ ($\overline{v'b'}$, $\overline{v'b'}\,S_b$) and across-$\overline{b}$ (0, $\overline{w'b'} - \overline{v'b'}\,S_b$) components, where S_b is the mean slope of the buoyancy surfaces, as in Spence *et al.* [2009] and Marshall and Radko [2003]. The divergence of the along-$\overline{b}$ component is

$$\begin{aligned} \nabla \cdot (\overline{v'b'},\ \overline{v'b'}\,S_b) &= -\frac{\partial}{\partial z}\left(\frac{\overline{v'b'}}{\partial_z \overline{b}}\right)\partial_y \overline{b} + \frac{\partial}{\partial y}\left(\frac{\overline{v'b'}}{\partial_z \overline{b}}\right)\partial_z \overline{b} \\ &= v^* \partial_y \overline{b} + w^* \partial_z \overline{b} \end{aligned} \tag{A.5}$$

where the advective eddy velocities (v^*, w^*) satisfy $\partial_y v^* + \partial_z w^* = 0$ and are related to the eddy streamfunction by

$$(v^*, w^*) = \left(-\frac{\partial \Psi^*}{\partial z},\ \frac{\partial \Psi^*}{\partial y}\right) \tag{A.6}$$

where Ψ^* is given by

$$\Psi^* = \frac{\overline{v'b'}}{\partial_z \overline{b}} \tag{A.7}$$

Here, we will make the assumption that the eddy fluxes are adiabatic (a good assumption in the interior), which is to say the across-$\overline{b}$ component of the eddy flux is zero. Of the eddy-flux terms in (A.2), we will retain only the along-$\overline{b}$ component, represented by the eddy advective velocities in (A.5). Now using (A.7) in (A.4) we can write the residual streamfunction as

$$\Psi^\dagger = \overline{\Psi} + \frac{\overline{v'b'}}{\partial_z \overline{b}} \tag{A.8}$$

and the residual velocities $(v^\dagger, w^\dagger)$ are therefore given by

$$v^\dagger = \overline{v} - \frac{\partial}{\partial z}\left(\frac{\overline{v'b'}}{\partial_z \overline{b}}\right),\ w^\dagger = \overline{w} + \frac{\partial}{\partial y}\left(\frac{\overline{v'b'}}{\partial_z \overline{b}}\right) \tag{A.9}$$

Now we can substitute (A.9) into (A.1) and (A.5) into (A.2) to derive transformed Eulerian mean equations

$$-fv^\dagger = -\frac{\Delta p}{L_x} + \overline{v'q'} + \frac{\partial \overline{\tau}}{\partial z} \tag{A.10}$$

$$v^\dagger \partial_y \overline{b} + w^\dagger \partial_z \overline{b} = \overline{S} \tag{A.11}$$

Now the eddy terms have been collected together in the momentum equation, and are given by the potential vorticity flux $\overline{v'q'}$. This is stated in terms of the eddy momentum and buoyancy fluxes, given by the divergence of the Eliassen-Palm vector:

$$\overline{v'q'} = -\frac{\partial}{\partial y}\left(\overline{u'v'}\right) + f\frac{\partial}{\partial z}\left(\frac{\overline{v'b'}}{\partial_z \bar{b}}\right) \tag{A.12}$$

Together with continuity and the thermal wind balance (A.3), the TEM equations, (A.10) and (A.11), form a closed system, which can be solved for the meridional overturning circulation of the mid-latitude atmosphere and the circumpolar ocean.

A.2 Influence of climate change on the westerly winds

Any processes which alter the character of upper-tropospheric eddies will have an influence of the surface westerly wind jet. In general the Rossby wave phase speed is [Barry and Chorley, 1998]:

$$c = u - \beta\left(\frac{L}{2\pi}\right)^2 \tag{A.13}$$

where $\beta = df/dy$, u is the background flow speed, and L is an appropriate length scale, often considered to be the Rossby Radius:

$$Lr = \frac{NH}{f} \tag{A.14}$$

where N is the buoyancy frequency, and H is a scale height and f is the Coriolis frequency. Other length scales, such as the Rhines scale may also be considered [Vallis, 2006; Kidston *et al.*, 2010b].

Climate forcing by greenhouse-gases warms the troposphere and cools the stratosphere [Santer *et al.*, 2003]. This has important consequences for the mid-latitude winds because 1) it raises the tropopause, increasing the scale height, H; 2) because the tropopause slopes downwards from the equator to the pole, a warming troposphere and cooling statosphere increases the meridional temperature gradient and therefore increases the thermal-wind-shear and zonal velocity, u [Kushner *et al.*, 2001] and 3) changes in the thermal-structure and moisture content of the atmosphere due to greenhouse-gas forcing can alter the static-stability, N [Kidston *et al.*, 2010a].

Under greenhouse gas forcing we therefore expect an increase in the strength of

the westerlies, u, owing to thermal-wind balance. The reasons for the poleward shift in the position of the jet are less well known. It has been proposed that an absolute speed up of tropospheric Rossby waves, owing to increases in u, causes the mid-latitude westerly jet to move poleward, because the faster moving eddies are being dissipated further away from their source region on the poleward side of the jet [Chen and Held, 2007]. However it has also been proposed that an increase in the Rossby-radius and eddy-length-scale through increases in N slows the waves relative to the mean flow, similarly leading to a poleward shifting jet [Kidston *et al.*, 2010b]. It may be noted that ozone destruction, which cools the polar stratosphere and raises the tropopause may have a similar effect. Indeed, coupled models suggest ozone forcing exerted stronger control over the westerly jet than greenhouse forcing in the Austral summer months over the 20th century [Son *et al.*, 2010].

A.3 Two box carbon cycle model

A.3.1 The formulation for uptake of anthropogenic emissions

To formulate the model with respect to emissions, we assume conservation of carbon within the atmosphere–ocean system. The atmosphere–ocean carbon inventory is given by

$$I_{OA} = M \cdot CO_2^a + \rho V C^o \tag{A.15}$$

where M is the number of moles of gas in the atmosphere (1.8×10^{20}), CO_2^a is the atmospheric CO_2 mixing ratio in mol mol $^{-1}$ (equivalent to parts per million, ppmv, and related to the partial pressure by $CO_2^a \cdot P = pCO_2^a$, where P is total atmospheric pressure = 1 atm), ρ is a reference ocean density (1025 kg m^{-3}), V is the volume of the ocean (1.4×10^{18} m^3) and C^o is the ocean inorganic carbon concentration in mol kg^{-1} (uniform in our one well mixed box ocean). Now, the change in atmospheric pCO_2^a due to human emissions, S_0 (mol), is given by

$$\frac{\Delta pCO_2^a}{P} = \frac{S_0 - \rho V C_{\text{ant}}}{M} \tag{A.16}$$

which is a statement that the change in atmospheric CO_2 is set by total emissions minus the carbon uptake by the ocean (recalling that C_{ant} is the concentration of anthropogenic carbon in the ocean). Now, using this formulation for the change in

atmospheric partial pressure of CO_2 we can rewrite (2.14) as

$$\frac{\partial C_{\text{ant}}}{\partial t} = \frac{k_o k_g P}{hM}\left(S_0 - \rho V C_{\text{ant}}\right) - \frac{\alpha R_B k_g}{h} C_{\text{ant}} \tag{A.17}$$

This equation can be solved using the integrating factor $\mu(t) = e^{\gamma t}$, where

$$\gamma = \frac{k_o k_g P \rho V + \alpha M R_B k_g}{hM} \tag{A.18}$$

yielding the solution (for a constant S_0)

$$\begin{aligned} C_{\text{ant}}(t) &= \left[\int \frac{k_o k_g P S_0}{hM} \cdot e^{\gamma t}\, \partial t\right] \Bigg/ e^{\gamma t} \\ &= \frac{1}{\gamma}\frac{k_o k_g P S_0}{hM} + a_1 e^{-\gamma t} \end{aligned} \tag{A.19}$$

Now applying the boundary condition that $C_{\text{ant}} = 0$ at $t = 0$, the constant a_1 is given by

$$a_1 = -\frac{k_o P S_0}{k_o P \rho V + \alpha M R_B} \tag{A.20}$$

which has units mol kg^{-1} as it should. Now, we must recognize that this expression is related to the oceanic fraction of emissions uptake, O_f by

$$\frac{O_f}{\rho V} = \frac{k_o P}{k_o P \rho V + \alpha M R_B} \tag{A.21}$$

which by rearranging and multiplying the numerator and denominator by the pre-industrial atmospheric mixing ratio, $CO^a_{2(eq)}$, yields

$$\begin{aligned} O_f &= \frac{(\rho V k_o P CO^a_{2(eq)})/\alpha R_B}{(\rho V k_o P CO^a_{2(eq)})/\alpha R_B + M \cdot CO^a_{2(eq)}} \\ &= \frac{C^o_{eq} \cdot \dfrac{m^o}{R_B}}{C^o_{eq} \cdot \dfrac{m^o}{R_B} + M \cdot CO^a_{2(eq)}} \end{aligned} \tag{A.22}$$

where we have used the definition of the pre-industrial DIC concentration, C^o_{eq}, from Section A.3.2 and the fact that the ocean mass is given by $m^o = \rho V$. Here,

$(m^o C^o_{eq})/R_B$ is the buffered ocean carbon inventory and $M \cdot CO^a_{2(eq)}$ is the atmospheric carbon inventory in the pre-industrial period as is appropriate [Archer, 2005]. Using a solubility $k_o = 0.033$ mol kg^{-1} atm^{-1} and other values listed above, the oceanic fraction is $O_f = 0.78$, which is quite reasonable and in line with more comprehensive estimates [Marinov and Sarmiento, 2004; Sarmiento and Gruber, 2006].

Now using the definition of O_f and $\tau = 1/\gamma$ we can express the solution as in (2.18)

$$C_{\text{ant}}(t) = \frac{S_0 \cdot O_f}{\rho V}\left(1 - \mathrm{e}^{-t/\tau}\right) \tag{A.23}$$

A.3.2 The formulation for specified atmospheric CO_2

Here we re-write (2.14) for the oceanic DIC concentration, C^o, as

$$\frac{\partial C^o}{\partial t} = \frac{k_o k_g}{h}\left(\, pCO^a_2(t) - pCO^o_2(t)\,\right) \tag{A.24}$$

Now recognizing that total ocean carbon concentration can be decomposed into an equilibrium concentration, C^o_{eq} (in equilibrium with an intial atmospheric partial pressure, $pCO^a_{2(eq)}$), and a perturbation concentration, ΔC^o, occurring due to changes in the atmospheric partial pressure (ΔpCO^a_2), we have $C^o = C^o_{eq} + \Delta C^o$ [similar to Oeschger *et al.*, 1975]. We use this separation to re-write (A.24) as

$$\frac{\partial (C^o_{eq} + \Delta C^o)}{\partial t} = \frac{k_o k_g}{h}\left(\, pCO^a_{2(eq)} + \Delta pCO^a_2\,\right) - \frac{k_g}{h}\left(\,\alpha C^o_{eq} + \alpha R_B \Delta C^o\,\right) \tag{A.25}$$

where we have related the oceanic partial pressure to the DIC concentration using the ionization fraction, α, and recognized that the response to perturbations is scaled by the buffer factor, R_B, as in (2.15). Now since $\partial C^o_{eq}/\partial t = 0$ by definition, at equilibrium the total ocean carbon concentration is balance with the atmospheric CO_2 concentration, which is given by the relation

$$C^o_{eq} = \frac{k_o}{\alpha} pCO^a_{2(eq)} \tag{A.26}$$

which we exploit in the main text. In this simple formulation, the DIC concentration is controlled by the specified model parameter, α, which in the real ocean and complex ESMs is a complex function of temperature, salinity and pH which determines the relative partitioning between the species of DIC [Sarmiento and Gruber, 2006]. In other words, in ESMs, the partitioning of DIC is computed by the solution of the

carbonate chemistry system.

Furthermore, it is possible to determine the response of ocean carbon, ΔC^o, to perturbations in atmospheric CO_2 concentrations (rather than emissions), by solving for the non-equilibrium terms of (A.25) using the integrating factor $\mu(t) = exp(t/\tau)$, where $\tau = h/(\alpha R_B k_g)$, yielding

$$\Delta C^o(t) = \left[\mathrm{e}^{t/\tau} \frac{k_o k_g}{h} \Delta pCO_2^a(t)\ \partial t \right] \Big/ \mathrm{e}^{t/\tau} \tag{A.27}$$

which for a simple CO_2 perturbation that is an instantaneous jump such that $\Delta pCO_2^a(t) = 0$ at $t = 0$ and is held constant at ΔpCO_2^a for $t \geq 0$, has the solution

$$\Delta C^o(t) = \frac{k_o \Delta pCO_2^a}{\alpha R_B} \left(1 - e^{-t/\tau} \right) \tag{A.28}$$

Note that $\Delta C^o(t)$ is equivalent to $C_{\mathrm{ant}}(t)$ in (2.18), except that here we have used specified atmospheric CO_2 concentrations, rather than specifying anthropogenic emissions as in (2.18). For a doubling of atmospheric CO_2 from pre-industrial values, $\Delta pCO_2^a = 280$ μatm, and our simple model predicts an increase in oceanic DIC, $\Delta C^o = 123$ μmol kg^{-1}, which is surprisingly in-line from estimates from the Ocean Carbon Intercomparison Project 3 models [Raven, 2005], given the simplicity of our model.

A.3.3 Model pre-industrial biases and carbon conservation

Using a biased parameter, α, in the model to determine the pre-industrial equilibrium DIC concentration, C^o_{eq}, effectively changes the amount of carbon in the atmosphere ocean system. To see this, consider two versions of the model, version V1 has the default parameter value $\alpha = 0.005$ and version V2 has a biased value $\alpha = 0.004$. In our simple model we chose this parameter, but in a complex ESM α will be controlled by the temperature, salinity and pH (and any factors that influence those variables). Now from (2.20) and using $CO_2^a = 280$ ppmv

$$C^o_{eq\,(V1)} = 1848\ \mu\text{mol kg}^{-1}, \qquad C^o_{eq\,(V2)} = 2310\ \mu\text{mol kg}^{-1} \tag{A.29}$$

The total inventory of carbon in the atmosphere-ocean system is given by (see A.3.1 above)

$$I_{OA} = M \cdot CO_2^a + \rho V C_{eq}^o \tag{A.30}$$

Thus we can see that model V2 has a far higher inventory of carbon in the pre-industrial ocean-atmosphere system than model V1. I also note that for our chosen values near $\alpha = 0.005$, the predicted mean ocean DIC concentration is quite reasonable relative to observed mean ocean values [Sarmiento and Gruber, 2006, e.g.], given the simplicity of the model.

Some spread in model parameters is consistent with our uncertainty in the amount of carbon in the pre-industrial ocean. However, when an ensemble of models has systematically biased parameters (relative to known values), it implies those models will have systematically biased amounts of carbon in their ocean–atmosphere systems. This is the case for systematic wind–biases in the CMIP3 and CMIP5 pre-industrial winds, which influence the ocean temperature and DIC concentration (see Chapters 3, 4 and 5).

A.4 Chapter 3 Appendix

List of models used

I acknowledge the modeling groups, the Program for Climate Model Diagnosis and Intercomparison (PCMDI) and the WCRP's Working Group on Coupled Modelling (WGCM) for their roles in making available the WCRP CMIP3 and CMIP5 multi-model datasets. Support of this dataset is provided by the Office of Science, U.S. Department of Energy.

Table A.1: CMIP3 and CMIP5 models used in Chapter 3

List of CMIP3 and CMIP5 models used in Chapter 3. The full set of models listed was for the historical period (1979 to 2010) and for the CMIP3 SRES A1B scenario, except for the last four CMIP5 models marked with a $^{+}$. Superscripts denote the subset of models used in the RCP 2.6[2], RCP 4.5[4], RCP 6.0[6], RCP 8.5[8], the SRES A2[A2] and the 1% per year increase in atmospheric CO_2* comparisons. CMIP5 Models with a $^{+}$ were used only for the 1% per year comparison.

CMIP3	**CMIP5**
CCCMA-CGCM3-1-t47[A2]*	BCC-CSM1-1[4,8]
CCCMA-CGCM3-1-t63	BNU-ESM[2,4,8]*
CNRM-CM3[A2]*	CanESM2[2,4,8]*
CSIRO-MK3-0[A2]*	CCSM4[2,4,6,8]*
CSIRO-MK3-5[A2]*	CSIRO-Mk3-6-0[2,4,6,8]*
GFDL-CM2-0[A2]*	GFDL-CM3[2,4,6,8]
GFDL-CM2-1[A2]*	GFDL-ESM2G[2,4,6,8]*
GISS-AOM	GFDL-ESM2M[2,4,6,8]*
GISS-MODEL-E-H*	GISS-E2-R[2,4,6,8]
GISS-MODEL-E-R[A2]*	HadCM3
IAP-FGOALS1-0-g*	HadGEM2-CC[4,8]
INGV-ECHAM4[A2]*	HadGEM2-ES[2,4,6,8]*
INMCM3-0[A2]*	INMCM4[4,8]*
IPSL-CM4[A2]*	IPSL-CM5A-LR[2,4,6,8]*
MIROC3-2-HIRES*	MIROC4h
MIROC3-2-MEDRES[A2]*	MIROC-ESM-CHEM[2,4,6,8]
MIUB-ECHO-G[A2]*	MIROC-ESM[2,4,6,8]*
MPI-ECHAM5[A2]*	MPI-ESM-LR[2,4,8]
MRI-CGCM2-3-2a[A2]*	MRI-CGCM3[2,4,6,8]*
NCAR-CCSM3-0[A2] *	NorESM1-ME[4]*
NCAR-PCM1[A2]*	NorESM1-M[2,4,6,8]*
UKMO-HADCM3[A2]*	IPSL-CM5A-MR^{+}
UKMO-HADGEM1[A2]*	IPSL-CM5B-LR^{+}
	MIROC5^{+}
	MPI-ESM-P^{+}

Trends in individual reanalyses, including MERRA and CFSR

The NASA MERRA, NCEP CFSR and ERA-Int reanalyses assimilate various satellite surface wind data, including from ERS-1, ERS-2 and QuikSCAT, which is not assimilated by the other reanalysis products (R1, R2 and 20CR). Visual inspection suggests that the SH westerly wind stress in MERRA and CFSR experienced a downward shift in 1991 and around 1996, coincident with the introduction of ERS-1 and ERS-2 data respectively, and larger than smaller downward shifts seen in the other reanalyses at the same times (Fig. A.1). As a result of these abrupt downward shifts the MERRA and CFSR reanalyses exhibit negative strength trends (not significant for MERRA) over the historical period from 1979–2010 (Fig. A.2), in contrast to the other four reanalyses and station based observational data [Hande *et al.*, 2012; Yang *et al.*, 2007] which show positive trends. The conspicuous disagreement of the strength trends in MERRA and CFSR with the other reanalyses and observations, together with the possibility that the negative trends maybe associated with shocks to the reanalysis system by the introduction of new satellite surface wind data in 1991 and 1996, lead me to exclude the MERRA and CFSR reanalyses from my analysis in the main text.

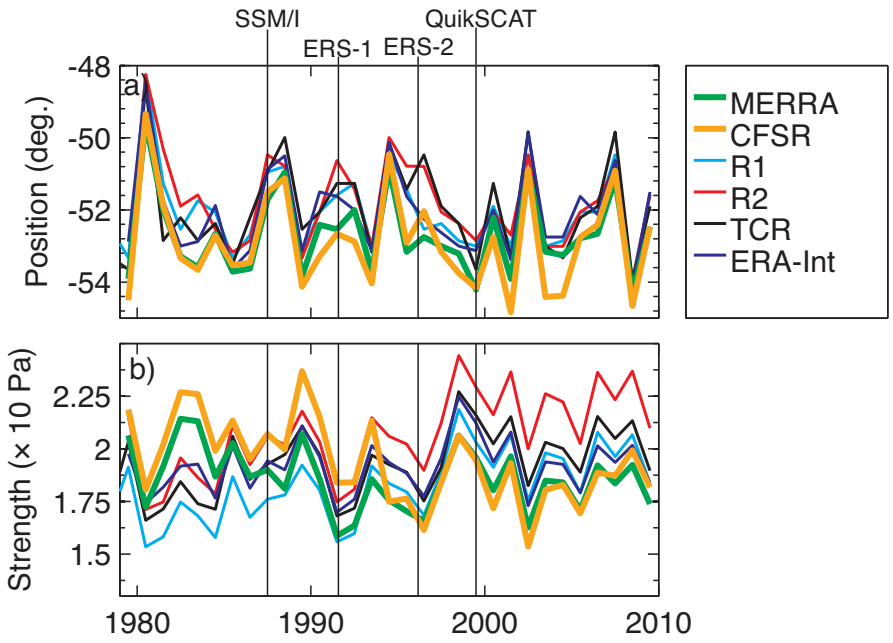

Figure A.1: Historical changes in the annual mean SH surface westerly wind-stress latitudinal position, a) and strength, b) of the zonal-mean zonal wind-stress. Changes are shown for NASA MERRA and NCEP CFSR reanalyses in addition to the four reanalysis products in the main text. Solid vertical lines show the dates when different satellite surface wind products began to be assimilated in the MERRA, CFSR and ERA-Int reanalyses.

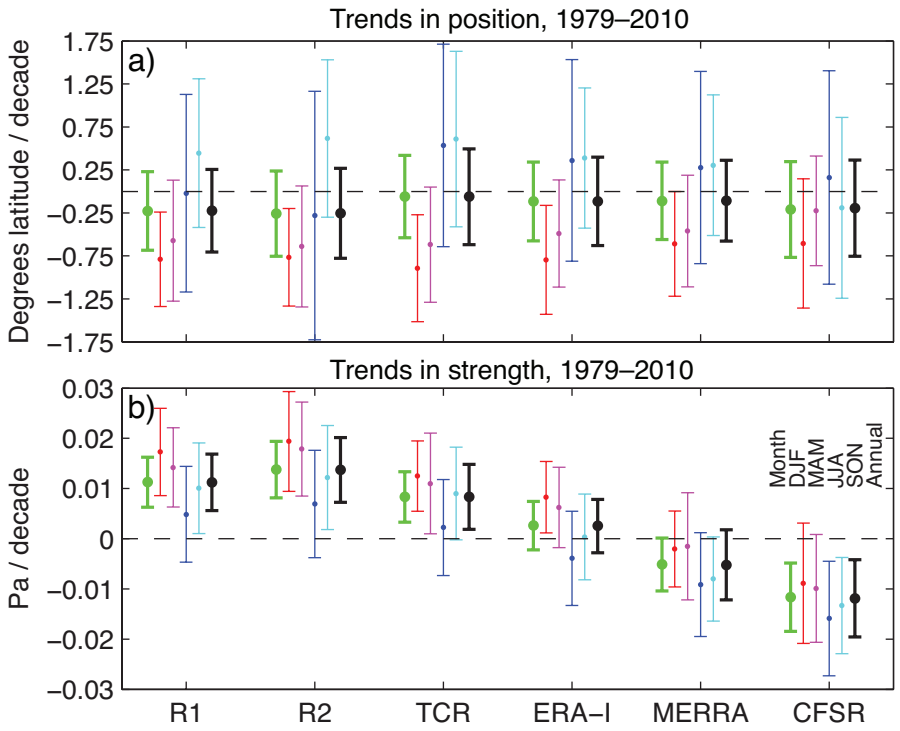

Figure A.2: Historical trends in the SH surface westerly wind-stress position, a) and strength, b). Trends are computed over the period 1979–2010 from six reanalysis products, including NASA MERRA and NCEP CFSR that were not included in the main text. The error bars show the 95% confidence interval of the trends, where auto-correlation has been accounted for. For each ensemble, trends are computed for monthly means, seasonal means and annual means of the zonal-mean zonal wind-stress.

Changes under CMIP3 SRES scenarios

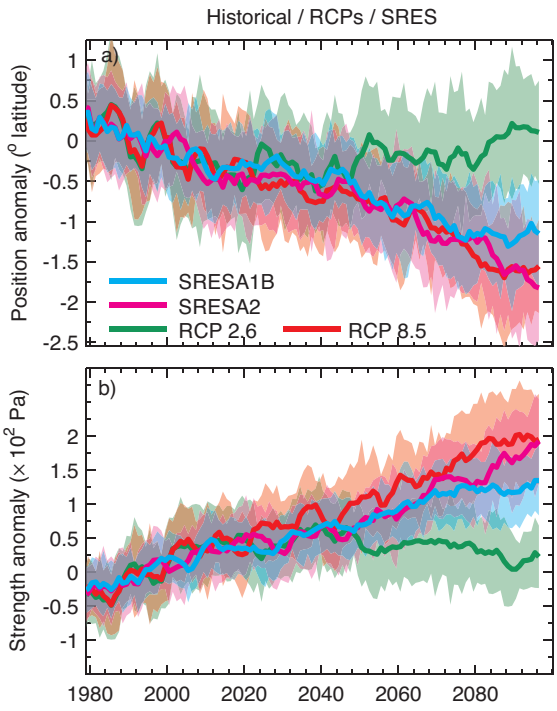

Figure A.3: Simulated changes in the annual mean SH surface westerly wind-stress position, a) and strength, b). The CMIP3 ensemble mean jet position and strength anomalies under historical (1979–2000) and SRES A2 and SRES A1B forcing scenarios (2001–2100) are shown together with the CMIP5 ensemble under historical (1979–2005) and RCP2.6 and RCP8.5 forcing scenarios (2006–2100). ; Anomalies are relative to the 1979–2010 base-period, and data have been smoothed with a 5–year wide boxcar.

A.5 The UVic Earth System Climate Model

For all my simulations I used version 2.9 of the intermediate complexity University of Victoria Earth System Climate Model (UVic ESCM) [Weaver *et al.*, 2001]. All the model components share a global domain with a horizontal resolution of 3.6° longitude by 1.8° latitude. The UVic ESCM has a fully dynamic 3-D ocean general circulation model based on the Modular Ocean Model version 2 [Pacanowski, 1995] with 19

vertical levels and a full explicit scheme for vertical convection [Pacanowski, 1995]. Horizontal diffusivity is set to a constant of 800 $m^2\ s^{-1}$, while vertical diffusivity is specified as a profile following Bryan and Lewis [1979] with values of $0.3 \times 10^{-4}\ m^2\ s^{-1}$ in the pycnocline increasing to $1.3 \times 10^{-4}\ m^2\ s^{-1}$ at depth. I note here that the diffusivities specified in the upper ocean are higher than observed and will lead to a significant upwelling of waters through the low-latitude thermocline (around 10 Sv), thereby reducing upwelling in the Southern Ocean [Schmittner *et al.*, 2005]. The Bryan–Lewis diffusivity profile was used here because it is widely employed in coarse resolution models, including the default version of the UVic ESCM, wherein it produces a reasonable tracer distribution and water mass ages [Eby *et al.*, 2009; Schmittner *et al.*, 2005]. The Gent-McWilliams (GM) parameterization of sub-grid scale eddy mixing [Gent and McWilliams, 1990] is included with the along-isopycnal diffusivity and the thickness diffusivity both set to a constant value in space and time of 800 $m^2\ s^{-1}$, unless otherwise stated.

The ocean model is coupled to a one layer energy-moisture balance (EMB) atmosphere model and a thermodynamic-dynamic sea ice model, which are described by Weaver *et al.* [2001]. The standard sea-ice model is used here, which has thermodynamics based on the zero layer model of Semtner [1976] with the lateral growth and melt paramterization of Hibler [1979] and with the dynamics incorporating the elastic viscous ice rheology of Hunke and Dukowicz [1997]. The UVic model has an option for including an ice-thickness distribution model with multiple categories and multilayer thermodynamics based on Bitz *et al.* [2001], but this option is not used here.

Surface wind-stress, surface wind-speed and vertically integrated atmospheric advective winds are specified due to the simplified nature of the model's atmosphere. The UVic model includes an option for a dynamic wind-feedback, computed as a geostrophic wind-anomaly based on sea-level pressure anomalies which are themselves derived from surface air temperature anomalies Weaver *et al.* [2001], but this option turned off here, unless explicitly stated.

The UVic model incorporates a state of the art carbon cycle. In the ocean the inorganic carbon cycle follows the Ocean Carbon-Cycle Model Intercomparison Project (OCMIP) protocols for air-sea gas exchange and carbon chemistry [Weaver *et al.*, 2001; Ewen *et al.*, 2004]. Specifically, the DIC concentration is given by:

$$[DIC] = [CO_2^*] + [HCO_3^-] + [CO_3^{2-}] \tag{A.31}$$

where CO_2^* is given by

$$CO_2^* = CO_{2(aq)} + H_2CO_{3(aq)} \tag{A.32}$$

Within the ocean CO_2 rapidly dissociates according to

$$H_2O + CO_2 + CO_3^{2-} = 2HCO3^- \tag{A.33}$$

where the concentrations of the carbonate and bicarbonate species depend on the concentrations of DIC and alkalinity. The air-sea flux is given by

$$F = k_g(k_o \cdot pCO_2^a - CO_{2\ (\mathrm{surf})}^*) \tag{A.34}$$

where k_o is the temperature dependent solubility derived from Henry's Law, pCO_2^a is the total atmospheric partial pressure of CO_2 and $CO_{2\ (\mathrm{surf})}^*$ is a function of surface temperature, salinity, alkalinity and DIC concentration. The piston velocity, k_g, is given by

$$k_g = (1 - \gamma_{\mathrm{ice}})\ 0.337\ w_s^2\ \left(\frac{Sc}{600}\right)^{-0.5} \tag{A.35}$$

where γ_{ice} is the sea-ice fraction, w_s is the surface wind-speed and Sc is the Sea-Surface Temperature dependent Schmidt number, and the numerical value of 0.337 represents a tuning constant chosen to give a reasonable ocean radiocarbon distribution [Ewen *et al.*, 2004].

The ocean ecosystem is represented by an improved Nutrient-Phytoplankton-Zooplankton-Detritus (NPZD) model, which includes interactive cycling of oxygen, phosphorous and nitrogen with prognostic denitrification and nitrogen fixation [Schmittner *et al.*, 2008; Schmittner *et al.*, 2005]. There are two classes of phytoplankton, grouped as nitrogen-fixing diazotrophs and all other phytoplankton. Particulate matter also occurs in the form of zooplankton and detritus, the latter of which results from plankton mortality and sloppy zooplankton feeding. Dissolved Organic Matter and the microbial loop are represented by a fast remineralization process, and representations of calcium carbonate production and dissolution are also included [Schmittner *et al.*, 2008]. The ocean sediments are represented by an oxic-only model of sediment respiration [Archer, 1996]. Terrestrial weathering is diagnosed from the net sediment flux during spin-up and held fixed at the equilibrium pre-industrial value for transient simulations, following Eby *et al.* [2013]. The terrestrial biosphere is represented by the dynamic vegetation model, TRIFFID, which is coupled to the land-surface scheme,

MOSES. The latter calculates the land carbon fluxes, distributes carbon between the vegetation and soil carbon pools and is coupled to the EMB atmosphere and ocean models [Meissner *et al.*, 2003-12-01; Matthews *et al.*, 2004].

Twentieth century simulations of the UVic ESCM produce realistic distributions of zonal mean temperature and salinity in the ocean, and surface air temperatures in the atmosphere [Weaver *et al.*, 2001]. The UVic ESCM was evaluated as part of the Coupled Carbon Cycle Climate Model Intercomparison Project [Friedlingstein *et al.*, 2006], the Paleoclimate Modeling Intercomparison Project [Weber *et al.*, 2007], and as part the recent EMIC intercomparison by Eby *et al.* [2013]. The characteristics of the coupled climate-carbon cycle system, including the air sea flux of CO_2, the distribution of ocean dissolved inorganic carbon (DIC) and alkalinity have previously been extensively evaluated for the UVic ESCM, and found to be in good agreement with observations [Eby *et al.*, 2009; Schmittner *et al.*, 2008]. The evolution of atmospheric CO_2, surface air-temperatures, the ocean and land carbon uptake and diagnosed emissions in previous transient simulations by the UVic ESCM over the 20th century also generally match observational estimates within uncertainty [Eby *et al.*, 2013; Eby *et al.*, 2009].

A.6 Chapter 4 Appendix

Table A.2: **CMIP3 Southern Hemisphere wind-stresses.** The pre-industrial (P.I.) observed wind-stress we derived is compared with the 18 CMIP3 models used in this study. The position gives the zonally-average position of the maximum westerly wind-stress. The strength gives zonally-averaged wind-stress, averaged over latitudes 35° – 60°S. The position and strength calculations were performed on the UVic ESCM grid, and represent a time-mean. The order the models are listed in corresponds to the magnitude of carbon anomaly in Figure 1. The 95% confidence interval is given for the CMIP3 ensemble mean, and the observations. The CMIP3 ensemble mean, and many of the individual models have a statistically different strength and position to the observations.

	Position (°S)	Strength (Pa)
UKMO.hadcm3	51.17	0.118
GFDL.cm2.1	51.48	0.120
CSIRO.mk3.5	53.41	0.146
MRI.cgcm2.3.2a	49.79	0.121
NCAR.pcm1	51.48	0.149
MIUB.echo.g	45.56	0.109
INGV.echam4	53.95	0.146
UKMO.hadgem1	51.79	0.139
CCCma.cgcm3.1.t63	50.29	0.138
CSIRO.mk3.0	51.19	0.144
MPI.echam5	49.52	0.139
CCCma.cgcm3.1	47.75	0.124
MIROC.3.2.hires	47.97	0.136
INMCM.3.0	48.8	0.131
GFDL.2.0	46.44	0.115
NCAR.ccsm3.0	51.68	0.161
GISS.aom	43.13	0.097
IPSL.cm4	42.59	0.090
Ens. mean	49.33 ± 1.61	0.129 ± 0.009
P.I. observations	52.31 ± 0.38	0.102 ± 0.015

A.7 Chapter 5 Appendix

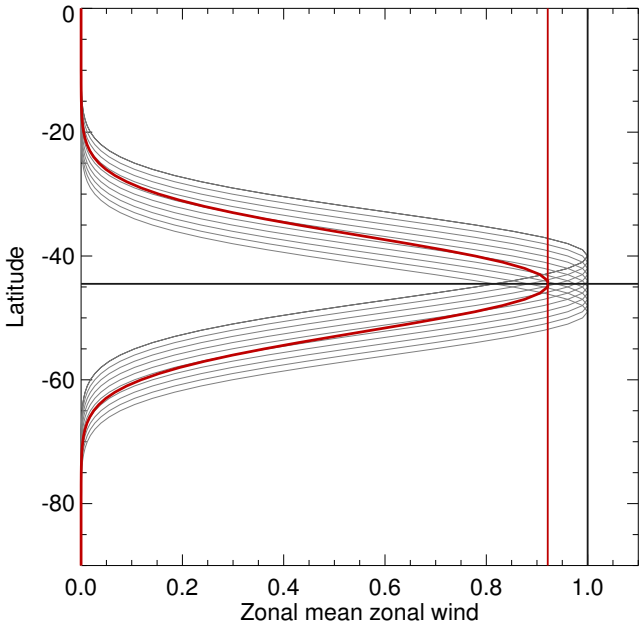

Figure A.4: Illustrative example of Gaussian westerly wind jets (grey) with their peaks, of magnitude 1, offset around a central latitude near 44°S. Computing an ensemble average over all the jets produces an ensemble mean jet (red), with the correct latitudinal position, but a peak strength that is weaker than any of the constituents.

Table A.3: List of CMIP5 models used in Chapter 5, including winds and sea-ice area. The full 28 models were used over the historical period, but the 4 models indicated were not used over the RCP4.5 period (2006–2100) because these simulations were not available. In all cases data correspond to run 1 of the model. Data were downloaded from the Coupled Model Intercomparison Project database (http://cmip-pcmdi.llnl.gov).

Model	RCP4.5
ACCESS1-0	yes
ACCESS1-3	yes
bcc-csm1-1	yes
CanESM2	yes
CMCC-CM	yes
CNRM-CM5	yes
CSIRO-Mk3-6-0	yes
FGOALS-s2	yes
GFDL-CM3	yes
GFDL-ESM2G	yes
GFDL-ESM2M	yes
GISS-E2-H	no
GISS-E2-R	yes
HadCM3	no
HadGEM2-AO	yes
HadGEM2-CC	yes
HadGEM2-ES	yes
inmcm4	yes
IPSL-CM5A-LR	yes
IPSL-CM5A-MR	yes
IPSL-CM5B-LR	no
MIROC5	yes
MIROC-ESM-CHEM	yes
MIROC-ESM	yes
MPI-ESM-LR	yes
MPI-ESM-MR	yes
MPI-ESM-P	no
MRI-CGCM3	yes

A.7.1 The 20CR winds and their uncertainty

The 20th Century Reanalysis is an ensemble reanalysis [Compo *et al.*, 2011], which means that in addition to the 'best guess' or ensemble mean field the ensemble spread (standard deviation) is available and this provides a measure of the uncertainty in the reanalysis fields. Here I analyze the 20CR monthly wind-speed (w_s, and its zonal (U) and meridional (V) components. The U and V components of the 20CR ensemble mean surface winds averaged by decade and longitude show little change outside the region of the Southern Hemisphere westerlies over the 140 years since 1871 (Fig. A.5). In marked contrast, the surface wind-speeds show a significant increase in time at all latitudes away from the equator. Since $w_s = (U^2 + V^2)^{0.5}$, the increase in monthly-mean wind-speed, but unchanging U and V components at many latitudes appears contradictory. In fact, the increase in w_s reflects a large increase in the variability of the daily U and V components even though the monthly-mean winds have remained approximately constant (Fig. A.6). That is to say increased variability in the daily winds is preserved in the monthly wind-speed field because of the squared terms, but for the U and V components increased daily variability averages to nearly zero in the monthly means.

The magnitude of the wind speed increase appears linearly related to latitude, with near zero change at the equator, and a maximum change near the poles. North of 80°N for example, wind speeds more than triple between the decades starting in 1871 and 2001. Such wind-speed changes would have had significant climate implications if they occurred.

However, several features of the 20CR wind-speeds suggest the increases may be at least partly spurious. Firstly, the decadal averages shows two periods (decades starting 1951 and 1981) where significant jumps in wind-speed occurred, most obvious when looking at the SH westerly jet near 50°S. Secondly, the ensemble spread is of a similar magnitude to the ensemble mean wind speed prior to the 1980's (Fig. A.5). The ensemble spread suggests that the ensemble mean wind-speed is highly uncertain, particularly at high latitudes and in the westerly jets. The 20CR experiences these large uncertainties due to data sparsity, which is most problematic in the Southern Hemisphere prior to 1940's [Compo *et al.*, 2011].

The U and V components of the 20CR surface wind also have significant uncertainties at high latitudes, but the ensemble mean of these quantities does not show a significant trend in time, except for in the Southern Hemisphere westerlies. Examina-

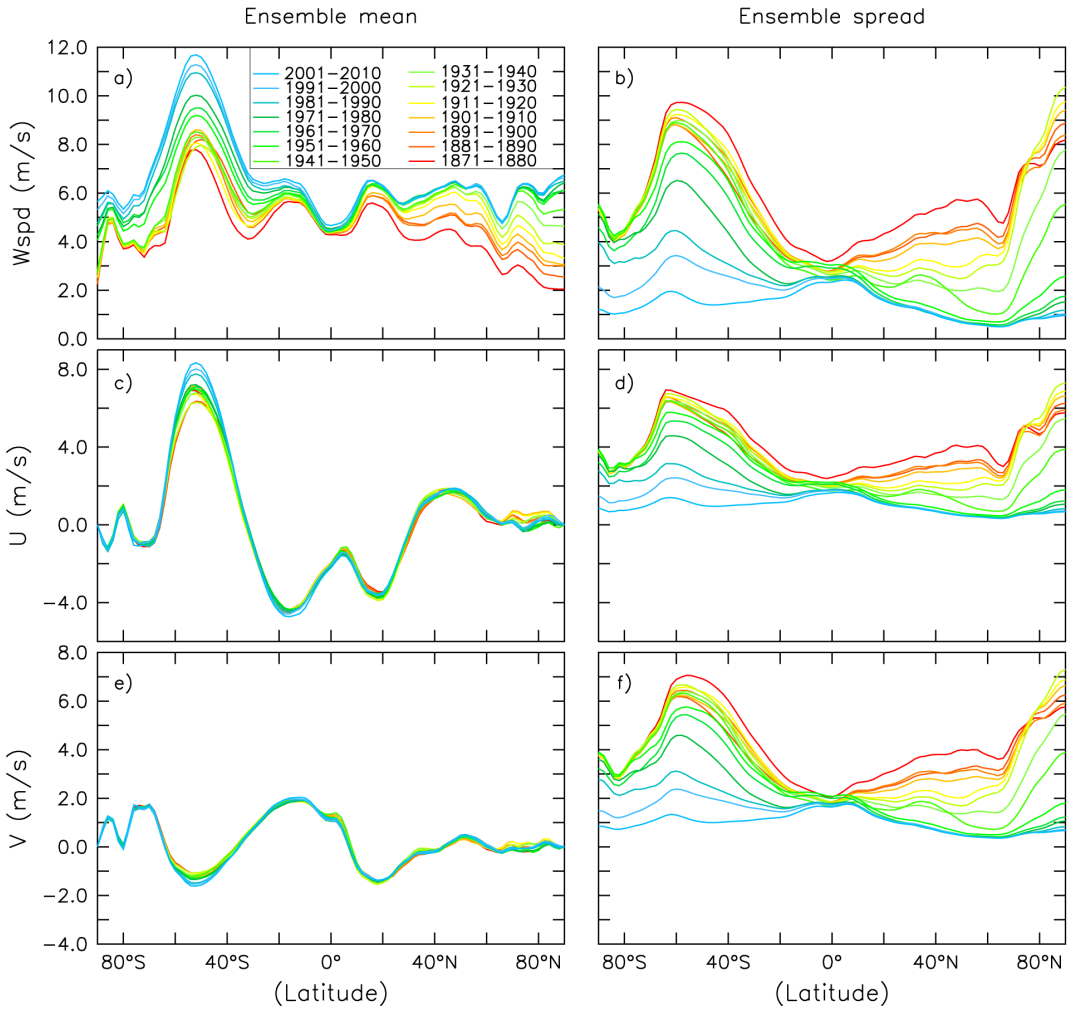

Figure A.5: The ensemble mean (left) and spread (right) of the wind-speed and U, V wind components from 20CR (at $\sigma = 0.995$), averaged zonally and by decade from 1871.

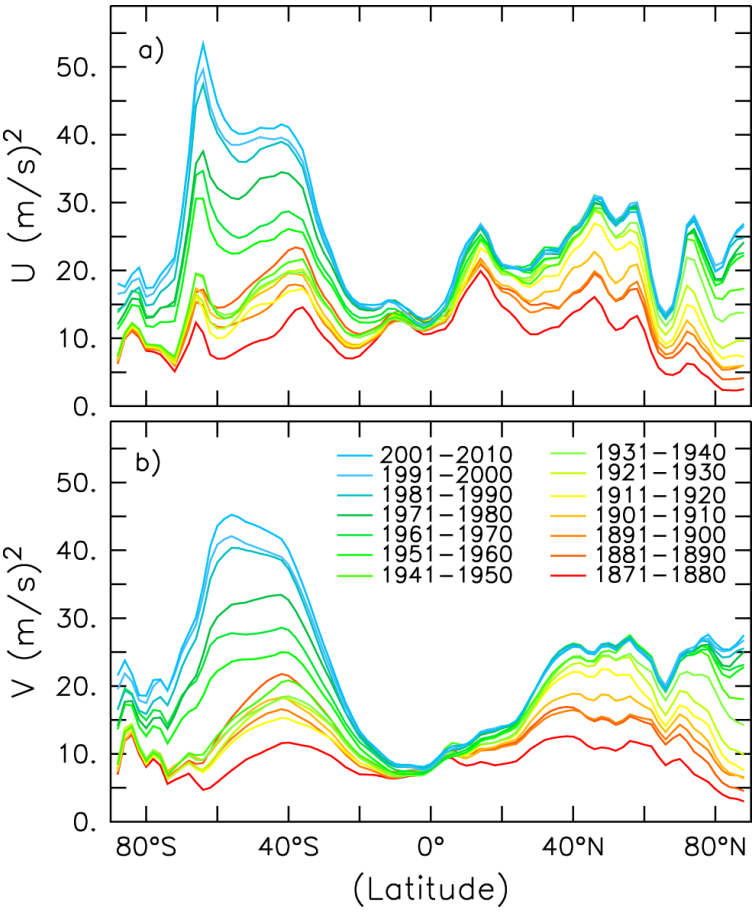

Figure A.6: The variance of the daily zonal-mean U and V wind components from 20CR by decade from 1871.

tion of the U-component of the 20CR wind suggests it may also experience the jumps referred to previously for wind-speed (i.e. 20CR may overestimate the strengthening of the jet over the 20th Century). Despite this uncertainty in the 20CR trend over the 20th century, I note that the CMIP5 models underestimate the strengthening of the SH westerly jet relative to several reanalyses over the more reliable satellite era (but there is also significant uncertainty in the trends amongst the reanalyses as discussed in Appendix A.4).

At this point there seems sufficient evidence to suggest caution in using the pre-1980 winds in 20CR. There is effectively no reliable estimate of the pre-satellite era global wind-fields, despite the huge importance of the wind field for ocean circulation and climate. Further research into this area is required, but beyond the scope of this thesis. For now, despite its high uncertainties 20CR remains the best estimate of the global wind-field available. To account for the uncertainty in observed winds, I will use both the pre-industrial 20CR climatology and the modern R1 based climatology to assess model performance in simulations of ocean carbon storage and uptake.

A.7.2 Supplementary Figures

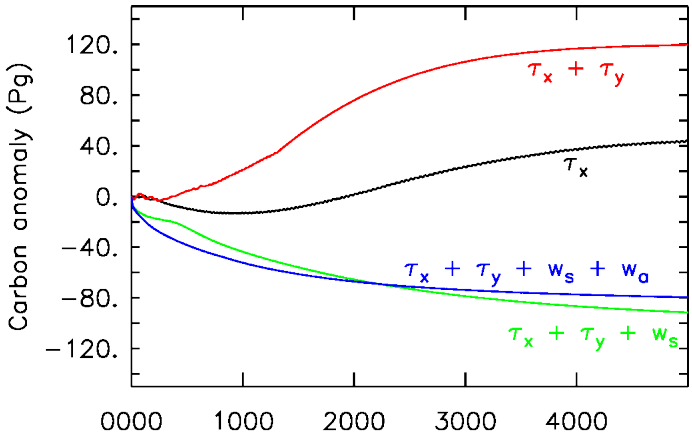

Figure A.7: The total ocean carbon anomaly under different components of the 20CR wind, relative to the simulation (C2) with all R1 winds. In each simulation, a component of the R1 winds was replaced by the corresponding component from 20CR, similar to the treatment of the CMIP5 winds in experiments discussed in the text, except that here an additional case was done where the advective winds were also replaced by 20CR. It can be seen that the change from R1 to 20CR winds for each of the surface wind components (τ_x, τ_y and w_s) significantly influences the result, but the change from R1 to 20CR advective winds (w_a, blue) has a relatively small effect.

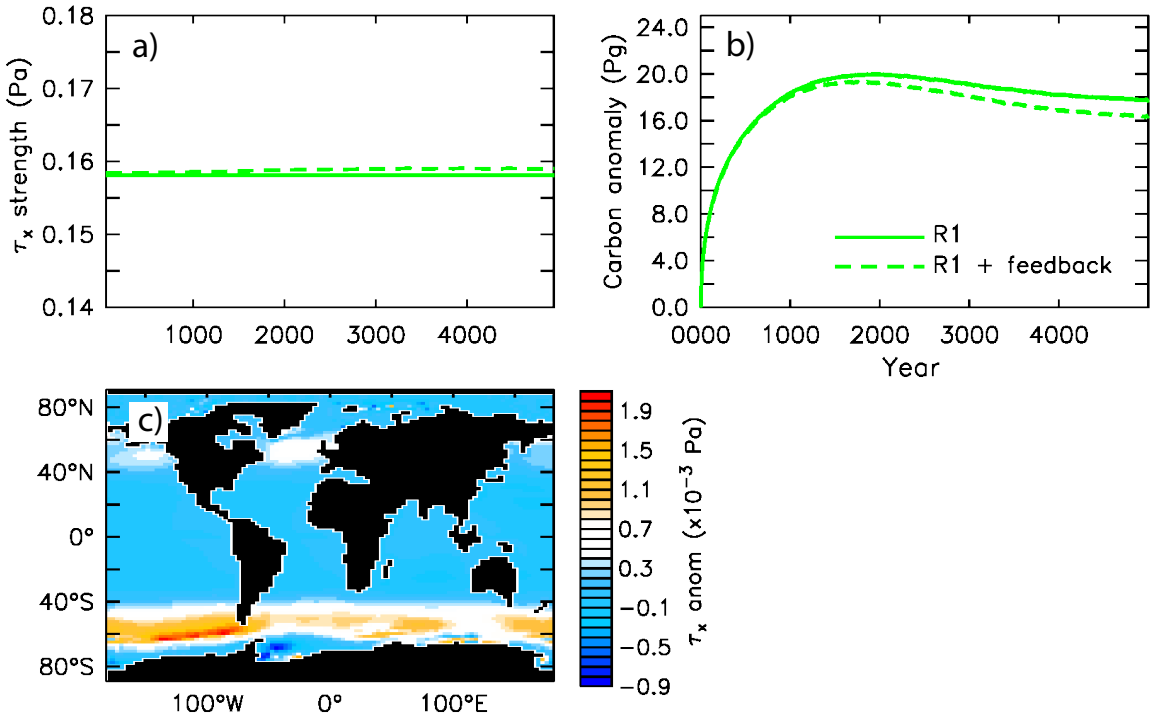

Figure A.8: a) The change in the strength of the Southern Hemisphere jet under the UVic model's dynamic wind-feedback (dashed); b) the influence of the feedback on total ocean carbon; c) map of the difference between the R1 wind climatology plus the feedback and the pure R1 climatology without the feedback. Note the differences in jet strength and ocean carbon due to the feedback are very small compared to the spread and temporal changes seen in the CMIP5 models.

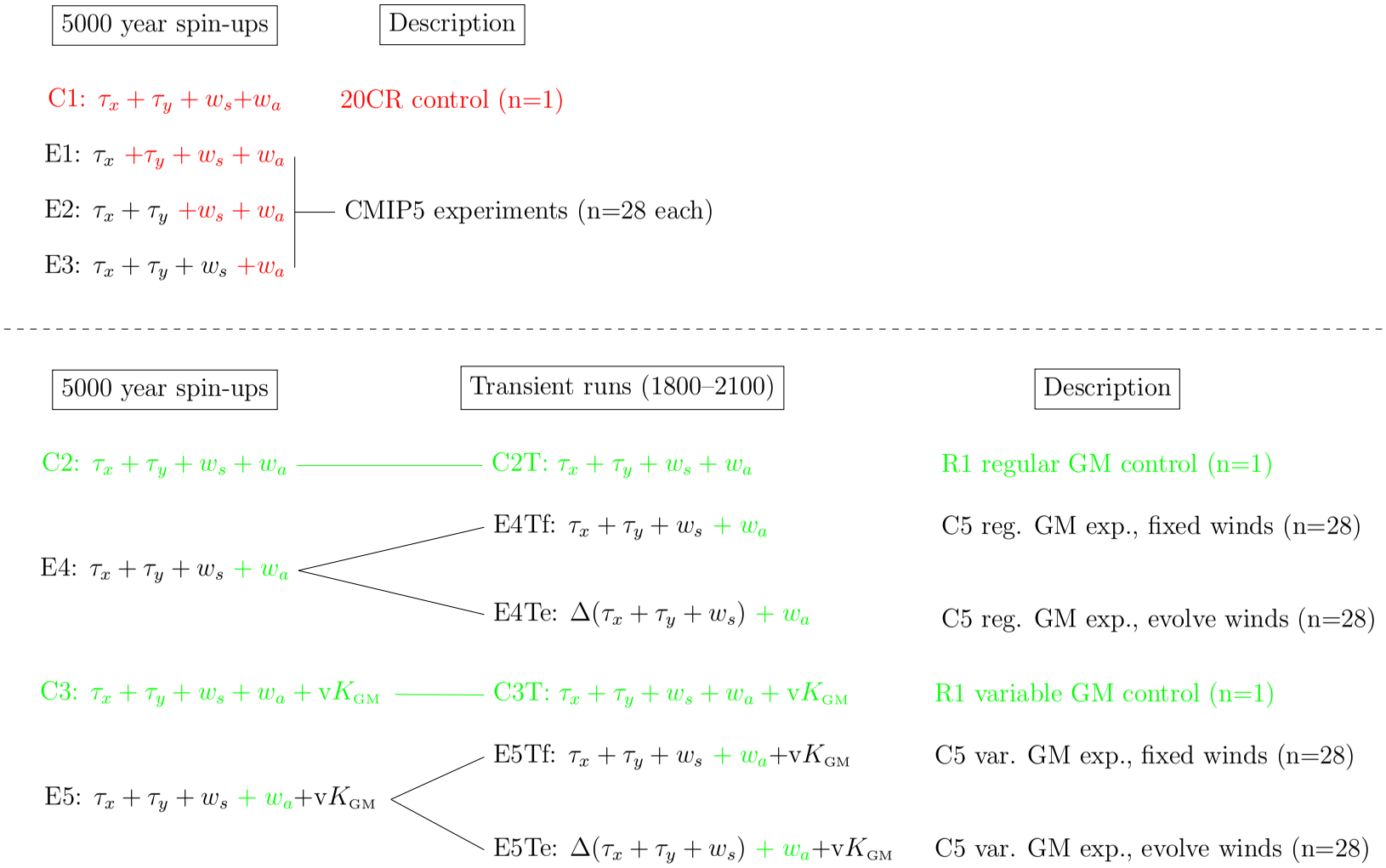

Figure A.9: Experimental design. The colour of the surface wind symbols indicates if they are taken from 20CR (red), R1 (green) or the CMIP5 models (black). Also indicated is whether a variable GM coefficient ($\mathrm{v}K_{\mathrm{GM}}$) is used. In the transient runs a Δ before the wind fields indicates that they are evolving in time from 1871–2100.

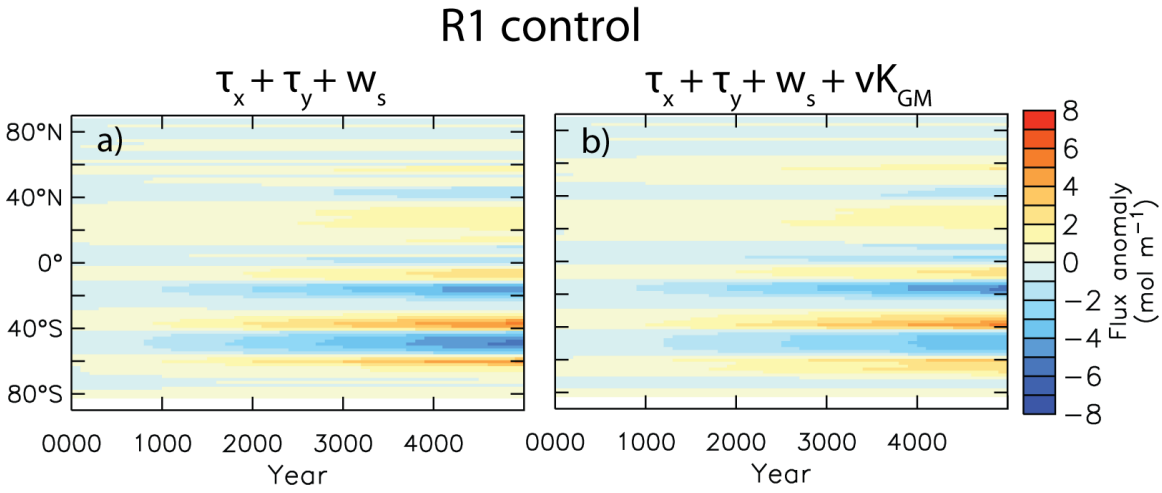

Figure A.10: The zonally-integrated, surface carbon fluxes in the regular GM and variable GM experiments, relative to the R1 control, and cumulated in time (mol m $^{-1}$).

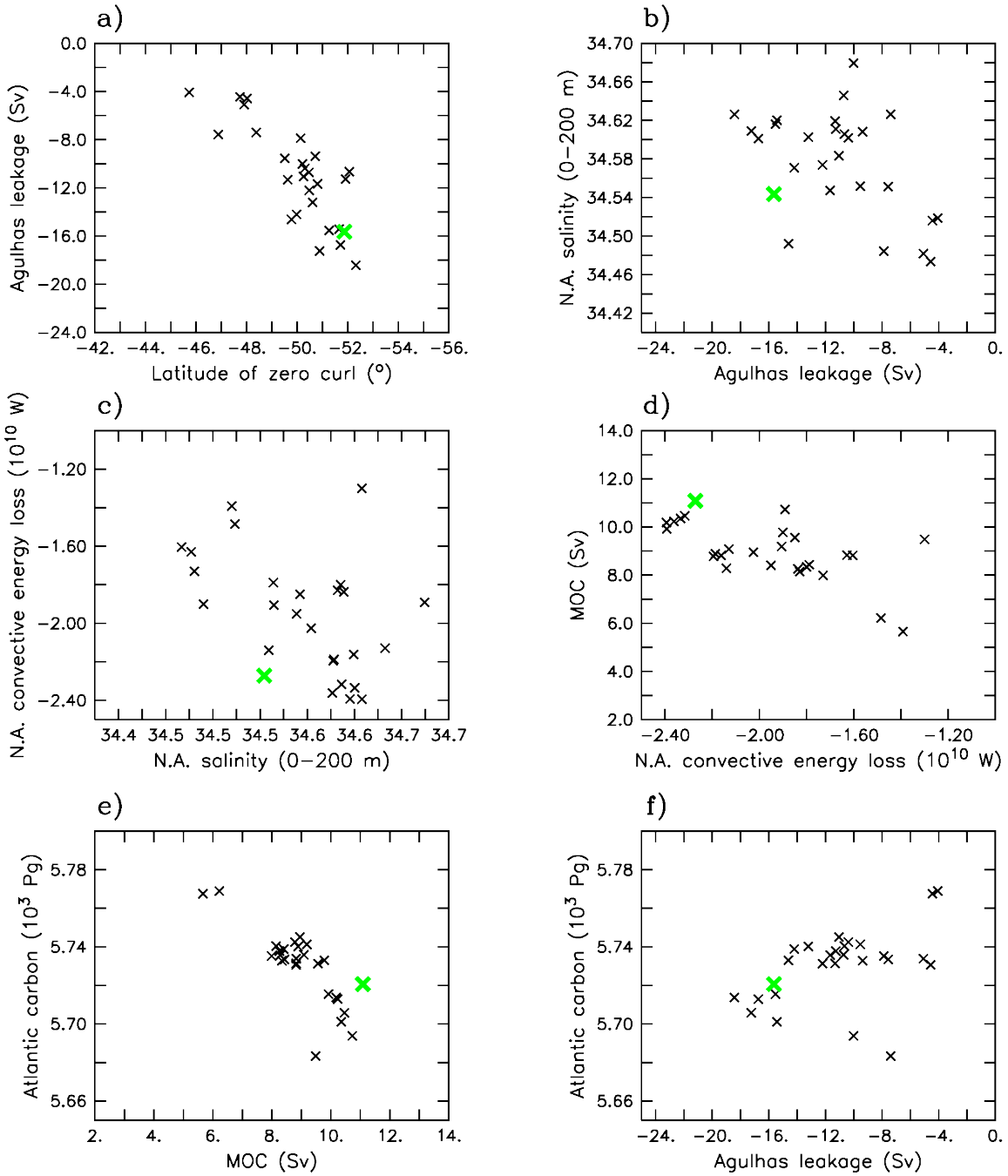

Figure A.11: **Equilibrium carbon-circulation relations.** **a,** Latitude of zero wind-stress-curl over the Indian Ocean (mean 20 – 40°E) vs. Agulhas Leakage at 20°E; **b,** Agulhas Leakage (20°E) vs. mean North Atlantic salinity in the upper 200 m; **c,** Mean North Atlantic salinity (0 – 200 m) vs. Energy loss from convection in the North Atlantic; **d,** Energy loss from convection in the North Atlantic vs. global Meridional Overturning stream-function (mean 500 – 2000 m, 30°S – 60°N); **e,** Mean MOC steam-function (500 – 2000 m, 30°S – 60°N) vs. Atlantic carbon (30°S – 60°N); **f,** Atlantic carbon (30°S – 60°N) vs. Agulhas Leakage (20°E). All variables are plotted based on the equilibrium experiment year 4900–5000 mean. The green markers show the R1 control, and all runs use the variable GM scheme.

A.8 Chapter 6 Appendix

A.8.1 Statistical analysis of sea-ice area trends

Here I follow Fyfe *et al.* [2013]. A representation of the trends can be written as

$$M_{ij} = u^m + Eint_{ij} + Emod_i,\ i = 1, ..., N^m,\ j = 1, ..., N_i \tag{A.36}$$

$$O = u^o + Eint^o \tag{A.37}$$

where M_{ij} and O are trends calculated from single runs or the observations; u^m and u^o are the true, unknown, deterministic trends due to external forcing in the modelled and observed worlds, where u^m is the trend component that is common to all models (in the limit, as the collection of exchangeable models grows infinitely large). $Eint_{ij}$ and $Eint^o$ are perturbations to M_{ij} and O respectively due to internal variability, and for the models this is different for each run. $Emod_i$ is the perturbation to M_{ij} that is introduced by model error in model i. We assume that these perturbations are exchangeable. N^m is the number of models, and N_i is the number of realizations for model i.

An estimator of $u^o - u^m$ is $O - M_{\cdot\cdot}$, where "$\cdot$" replacing the subscripts represents averaging over that subscript. The null hypothesis is

$$H_0 : u^m = u^o \tag{A.38}$$

which can be tested using an empirical distribution that includes the sources of uncertainty in (A.36) and (A.37). The empirical distribution is constructed as follows:

a) Compute the observed trend, O

b) Select a sample of N^m models with replacement and for each selection, draw one run at random from that model's available ensemble of realizations, and then average over those N^m runs to obtain a version of $M_{\cdot\cdot}$.

c) Select, at random, a single model i from models with multiple simulations, and then select, at random, a single run j from that model's ensemble. Calculate the difference $M_{ij} - M_{i\cdot}$ between the trend in that single run and the mean of the trends from that model's ensemble.

This difference is an estimate of the deviation in the j-th trend for model i that is induced by internal variability. Since the model i ensemble is generally small, the deviations are smaller than would be representative of an infinitely large replication of runs for model i, and so to compensate for that loss of variance, multiply the difference $M_{ij} - M_{i.}$ by $[N_i/(N_i - 1)]^{0.5}$.

d) Calculate a − b + c, as computed in the steps above, and repeat many times to build a distribution for a − b + c.

From this distribution we ascertain whether the observed trend is inside the 5–95% range of individual model trends, and therefore whether we accept or reject the null hypothesis.

For the rational for this procedure see Fyfe *et al.* [2013].

Table A.4: CMIP5 models used in this study, and the number of runs for each model.

Model	# of runs
ACCESS1-0	1
ACCESS1-3	3
bcc-csm1-1	3
bcc-csm1-1-m	3
BNU-ESM	1
CanCM4	10
CanESM2	5
CCSM4	6
CESM1-BGC	1
CESM1-CAM5	3
CESM1-WACCM	4
CMCC-CM	1
CMCC-CMS	1
CNRM-CM5	10
CSIRO-Mk3-6-0	10
FGOALS-s2	3
FIO-ESM	3
GFDL-CM3	5
GFDL-ESM2G	1
GFDL-ESM2M	1
GISS-E2-H	5
GISS-E2-R	5
HadCM3	10
HadGEM2-AO	1
HadGEM2-CC	2
HadGEM2-ES	4
inmcm4	1
IPSL-CM5A-LR	6
IPSL-CM5A-MR	3
IPSL-CM5B-LR	1
MIROC5	5
MIROC-ESM-CHEM	1
MIROC-ESM	3
MPI-ESM-LR	3
MPI-ESM-MR	3
MRI-CGCM3	3
NorESM1-ME	1
NorESM1-M	3

Table A.5: Ice-sheet mass loss acceleration and freshwater fluxes. Note 1 Sv $= 1 \times 10^6$ $m^3 s^{-1}$.

Experiment		mass loss acceleration (Gt yr^{-2})	Fresh-water flux acceleration (Sv yr^{-1})
WAIS	1	3.15	0.0001
	2	6.31	0.0002
	3	9.46	0.0003
	4	12.61	0.0004
	5	15.77	0.0005
AIS	1	3.15	0.0001
	2	6.31	0.0002
	3	9.46	0.0003
	4	12.61	0.0004
	5	15.77	0.0005
	6	18.92	0.0006
	7	22.08	0.0007
	8	25.23	0.0008
	9	28.38	0.0009
	10	31.54	0.001

Bibliography

Aiken, C. M. and M. H. England (2008), Sensitivity of the Present-Day Climate to Freshwater Forcing Associated with Antarctic Sea Ice Loss, *Journal of Climate*, **21,** pp. 3936–3946, DOI: 10.1175/2007JCLI1901.1 (see pp. 87, 90).

Archer, D. (1996), A data-driven model of the global calcite lysocline, *Global Biogeochemical Cycles*, **10,** pp. 511–526, DOI: 10.1029/96GB01521 (see p. 113).

— (2010), *The global carbon cycle*, Princeton University Press, New Jersey (see p. 6).

Archer, D. (2005), Fate of fossil fuel CO2 in geologic time, *Journal of Geophysical Research: Oceans*, **110,** n/a–n/a, DOI: 10.1029/2004JC002625 (see pp. 10, 20, 104).

Archer, D., M. Eby, V. Brovkin, A. Ridgwell, L. Cao, U. Mikolajewicz, K. Caldeira, K. Matsumoto, G. Munhoven, A. Montenegro, and K. Tokos (2009), Atmospheric Lifetime of Fossil Fuel Carbon Dioxide, English, *Annual Review of Earth and Planetary Sciences*, Annual Review of Earth and Planetary Sciences **37,** 117–134, DOI: 10.1146/annurev.earth.031208.100206 (see p. 10).

Ballantyne, A., C. Alden, J. Miller, P. Tans, and J. White (2012), Increase in observed net carbon dioxide uptake by land and oceans during the past 50 years, *Nature*, **488,** pp. 70–72, DOI: 10.1038/nature11299 (see p. 6).

Barry, R. and R. Chorley (1998), *Atmosphere, Weather and Climate*, 7th ed., London: Routledge, p. 409 (see p. 101).

Beal, L., W. P. M. de Ruijter, A. Biastoch, R. Zahn, M. Cronin, J. Hermes, J. Lutjeharms, G. Quartly, T. Tozuka, S. Baker-Yeboah, T. Bornman, P. Cipollini, H. Dijkstra, I. Hall, W. Park, F. Peeters, P. Penven, H. Ridderinkhof, and J. Zinke (2011), On the role of the Agulhas system in ocean circulation and climate, *Nature*, **472,** pp. 429–436, DOI: 10.1038/nature09983 (see pp. 25, 43).

Biastoch, A., C. W. Boning, and J. R. E. Lutjeharms (2008), Agulhas leakage dynamics affects decadal variability in Atlantic overturning circulation, *Nature*, **456,** pp. 489–492 (see p. 45).

Biastoch, A., C. W. Boning, F. U. Schwarzkopf, and J. R. E. Lutjeharms (2009), Increase in Agulhas leakage due to poleward shift of Southern Hemisphere westerlies, *Nature*, **462,** pp. 495–498, DOI: 10.1038/nature08519 (see pp. 33, 43, 45, 50).

Bintanja, R., G. J. van Oldenborgh, S. S. Drijfhout, B. Wouters, and C. A. Katsman (2013), Important role for ocean warming and increased ice-shelf melt in Antarctic sea-ice expansion, *Nature Geosci*, **advance online publication,** pp. – (see pp. 90, 92, 94).

Bitz, C. M., M. M. Holland, A. J. Weaver, and M. Eby (2001), Simulating the ice-thickness distribution in a coupled climate model, *Journal of Geophysical Research: Oceans*, **106,** pp. 2441–2463, DOI: 10.1029/1999JC000113 (see pp. 95, 112).

Bitz, C. and L. Polvani (2012), Antarctic climate response to stratospheric ozone depletion in a fine resolution ocean climate model, *Geophysical Research Letters*, **39,** p. L20705, DOI: 10.1029/2012GL053393 (see p. 87).

Böning, C., A. Dispert, M. Visbeck, S. Rintoul, and F. Schwarzkopf (2008), The response of the Antarctic Circumpolar Current to recent climate change, *Nature Geoscience*, **1,** pp. 864–869, DOI: 10.1038/ngeo362 (see pp. 53, 59, 60).

Bryan, K. and L. Lewis (1979), A water mass model of the world ocean, *J. Geophys. Res.*, **84,** pp. 2503–2517, DOI: 10.1029/JC084iC05p02503 (see p. 112).

Chen, G. and I. M. Held (2007), Phase speed spectra and the recent poleward shift of Southern Hemisphere surface westerlies, *Geophys. Res. Lett.*, **34,** DOI: 10.1029/2007GL031200 (see p. 102).

Compo, G. P., J. S. Whitaker, P. D. Sardeshmukh, N. Matsui, R. J. Allan, X. Yin, B. E. Gleason, R. S. Vose, G. Rutledge, P. Bessemoulin, S. Brönnimann, M. Brunet, R. I. Crouthamel, A. N. Grant, P. Y. Groisman, P. D. Jones, M. C. Kruk, A. C. Kruger, G. J. Marshall, M. Maugeri, H. Y. Mok, Ø. Nordli, T. F. Ross, R. M. Trigo, X. L. Wang, S. D. Woodruff, and S. J. Worley (2011), The Twentieth Century Reanalysis Project, *Q. J. Roy. Meteor. Soc.*, **137,** pp. 1–28, DOI: 10.1002/qj.776 (see pp. 27, 37, 54, 89, 118).

De Szoeke, R. and M. Levine (1981), The advective flux of heat by mean geostrophic motions in the Southern Ocean, *Deep Sea Research*, **28A,** DOI: 10.1016/0198-0149(81)90048-0 (see p. 13).

Dee, D. P., S. M. Uppala, A. J. Simmons, P. Berrisford, P. Poli, S. Kobayashi, U. Andrae, M. A. Balmaseda, G. Balsamo, P. Bauer, P. Bechtold, A. C. M. Beljaars,

L. van de Berg, J. Bidlot, N. Bormann, C. Delsol, R. Dragani, M. Fuentes, A. J. Geer, L. Haimberger, S. B. Healy, H. Hersbach, E. V. Hólm, L. Isaksen, P. Kållberg, M. Köhler, M. Matricardi, A. P. McNally, B. M. Monge-Sanz, J.-J. Morcrette, B.-K. Park, C. Peubey, P. de Rosnay, C. Tavolato, J.-N. Thépaut, and F. Vitart (2011), The ERA-Interim reanalysis: configuration and performance of the data assimilation system, *Q. J. Roy. Meteor. Soc.*, **137,** pp. 553–597, DOI: 10.1002/qj.828 (see p. 27).

d'Orgeville, M., W. P. Sijp, M. H. England, and K. J. Meissner (2010), On the control of glacial-interglacial atmospheric CO2 variations by the Southern Hemisphere westerlies, *Geophys. Res. Lett.*, **37,** DOI: 10.1029/2010GL045261 (see p. 73).

Eby, M., K. Zickfeld, A. Montenegro, D. Archer, K. J. Meissner, and A. J. Weaver (2009), Lifetime of Anthropogenic Climate Change: Millennial Time Scales of Potential CO_2 and Surface Temperature Perturbations, *J. Climate*, **22,** pp. 2501–2511 (see pp. 7, 10, 37, 112, 114).

Eby, M., A. J. Weaver, K. Alexander, K. Zickfeld, A. Abe-Ouchi, A. A. Cimatoribus, E. Crespin, S. S. Drijfhout, N. R. Edwards, A. V. Eliseev, G. Feulner, T. Fichefet, C. E. Forest, H. Goosse, P. B. Holden, F. Joos, M. Kawamiya, D. Kicklighter, H. Kienert, K. Matsumoto, I. I. Mokhov, E. Monier, S. M. Olsen, J. O. P. Pedersen, M. Perrette, G. Philippon-Berthier, A. Ridgwell, A. Schlosser, T. Schneider von Deimling, G. Shaffer, R. S. Smith, R. Spahni, A. P. Sokolov, M. Steinacher, K. Tachiiri, K. Tokos, M. Yoshimori, N. Zeng, and F. Zhao (2013), Historical and idealized climate model experiments: an intercomparison of Earth system models of intermediate complexity, *Climate of the Past*, **9,** pp. 1111–1140, DOI: 10.5194/cp-9-1111-2013 (see pp. 7, 18, 61, 89, 113, 114).

Ewen, T. L., A. J. Weaver, and M. Eby (2004), Sensitivity of the inorganic ocean carbon cycle to future climate warming in the UVic coupled model, *Atmosphere-Ocean*, **42,** pp. 23–42, DOI: 10.3137/ao.420103 (see pp. 112, 113).

Farneti, R. and P. R. Gent (2011), The effects of the eddy-induced advection coefficient in a coarse-resolution coupled climate model, *Ocean Modelling*, **39,** pp. 135–145, DOI: 10.1016/j.ocemod.2011.02.005 (see p. 60).

Follows, M. and R. Williams (2004), *The ocean carbon cycle and climate*. In: ed. by M. Follows and T. Oguz, vol. 40, NATO Science Series, Kluwer, chap. Mechanisms controlling the air-sea flux of CO_2 in the North Atlantic (see p. 20).

Friedlingstein, P., P. Cox, R. Betts, L. Bopp, W. von Bloh, V. Brovkin, P. Cadule, S. Doney, M. Eby, I. Fung, G. Bala, J. John, C. Jones, F. Joos, T. Kato, M.

Kawamiya, W. Knorr, K. Lindsay, H. D. Matthews, T. Raddatz, P. Rayner, C. Reick, E. Roeckner, K. G. Schnitzler, R. Schnur, K. Strassmann, A. J. Weaver, C. Yoshikawa, and N. Zeng (2006), Climate–Carbon Cycle Feedback Analysis: Results from the C4MIP Model Intercomparison, *Journal of Climate*, **19,** pp. 3337–3353, DOI: 10.1175/JCLI3800.1 (see pp. 7, 37, 114).

Fyfe, J. C., N. Gillet, and Z. Zwiers (2013), The recent hiatus in global warming, *Nature Climate Change*, **(Submitted),** (see pp. 92, 126, 127).

Fyfe, J. and O. Saenko (2006), Simulated changes in the extratropical Southern Hemisphere winds and currents, *Geophys. Res. Lett.*, **33,** DOI: 10.1029/2005GL025332 (see pp. 25, 37, 50).

Fyfe, J., S. O.A., K. Zickfeld, M. Eby, and A. Weaver (2007), The role of poleward intensifying winds on Southern Ocean warming, *J. Climate*, **20,** DOI: 10.1175/2007JCLI1764.1 (see p. 60).

Gent, P. R. and G. Danabasoglu (2011), Response to Increasing Southern Hemisphere Winds in CCSM4, *Journal of Climate*, **24,** pp. 4992–4998, DOI: 10.1175/JCLI-D-10-05011.1 (see p. 59).

Gent, P. and J. McWilliams (1990), Isopycnal mixing in ocean circulation models, *J. Phys. Oceanogr.*, **20,** pp. 150–155, DOI: 10.1175/1520-0485(1990)020<0150:IMIOCM>2.0.CO;2 (see pp. 13, 48, 59, 89, 112).

Gent, P., J. Willebrand, T. J. McDougall, and J. McWilliams (1995), Parameterizing Eddy-induced tracer transports in Ocean circulation models, *J. Phys. Oceanogr.*, **25,** pp. 463–474, DOI: 10.1175/1520-0485(1995)025<0463:PEITTI>2.0.CO;2 (see pp. 59, 89).

Gill, A. (1982), *Atmosphere-Ocean Dynamics*, International Geophysics Series, Academic Press (see pp. 16, 17).

Gille, S. T. (2008), Decadal-Scale Temperature Trends in the Southern Hemisphere Ocean, *J. Climate*, **21,** pp. 4749–4765, DOI: 10.1175/2008JCLI2131.1 (see p. 33).

Gloor, M., J. L. Sarmiento, and N. Gruber (2010), What can be learned about carbon cycle climate feedbacks from CO_2 airborne fraction?, *Atmospheric Chemistry and Physics Discussions*, **10,** pp. 9045–9075, DOI: 10.5194/acp-10-7739-2010 (see p. 7).

Gnanadesikan, A. (1999), A Simple Predictive Model for the Structure of the Oceanic Pycnocline, *Science*, **283,** pp. 2077–2079, DOI: 10.1126/science.283.5410.2077 (see pp. 14, 15).

Gnanadesikan, A. and R. W. Hallberg (2000), On the Relationship of the Circumpolar Current to Southern Hemisphere Winds in Coarse-Resolution Ocean Models, *Journal of Physical Oceanography*, **30,** pp. 2013–2034, DOI: 10.1175/1520-0485(2000)030<2013:OTROTC>2.0.CO;2 (see pp. 14, 73).

Gnanadesikan, A., K. W. Dixon, S. M. Griffies, V. Balaji, M. Barreiro, J. A. Beesley, W. F. Cooke, T. L. Delworth, R. Gerdes, M. J. Harrison, I. M. Held, W. J. Hurlin, H.-C. Lee, Z. Liang, G. Nong, R. C. Pacanowski, A. Rosati, J. Russell, B. L. Samuels, Q. Song, M. J. Spelman, R. J. Stouffer, C. O. Sweeney, G. Vecchi, M. Winton, A. T. Wittenberg, F. Zeng, R. Zhang, and J. P. Dunne (2006), GFDL's CM2 Global Coupled Climate Models. Part II: The Baseline Ocean Simulation, *Journal of Climate*, **19,** pp. 675–697, DOI: 10.1175/JCLI3630.1 (see pp. 60, 89).

Gruber, N., M. Gloor, S. Mikaloff Fletcher, S. Doney, S. Dutkiewicz, M. Follows, M. Gerber, A. Jacobson, F. Joos, K. Lindsay, D. Menemenlis, A. Mouchet, S. Muller, J. Sarmiento, and T. Takahashi (2009), Oceanic sources, sinks, and transport of atmospheric CO_2, *Global Biogeochemical Cycles*, **23,** DOI: 10.1029/2008GB003349 (see pp. 10, 11, 53).

Hallberg, R. W. and A. Gnanadesikan (2006), The Role of Eddies in Determining the Structure and Response of the Wind-Driven Southern Hemisphere Overturning: Results from the Modeling Eddies in the Southern Ocean (MESO) Project, *J. Phys. Oceanogr.*, **36,** pp. 2232–2252, DOI: 10.1175/JPO2980.1 (see pp. 15, 53, 59).

Hande, L. B., S. T. Siems, and M. J. Manton (2012), Observed Trends in Wind Speed over the Southern Ocean, *Geophys. Res. Lett.*, **39,** DOI: 10.1029/2012GL051734 (see pp. 32, 56, 108).

Hellmer, H. H. (2004), Impact of Antarctic ice shelf basal melting on sea ice and deep ocean properties, *Geophysical Research Letters*, **31,** n/a–n/a, DOI: 10.1029/2004GL019506 (see p. 90).

Hibbard, K., G. A. Meehl, P. M. Cox, and P. Friedlingstein (2007), A Strategy for Climate Change Stabilization Experiments, *EOS*, **88,** pp. 217–221, DOI: 10.1029/2007EO200002 (see p. 37).

Hibler, W. D. (1979), A Dynamic Thermodynamic Sea Ice Model, *Journal of Physical Oceanography*, **9,** pp. 815–846, DOI: 10.1175/1520-0485(1979)009<0815:ADTSIM>2.0.CO;2 (see p. 112).

Holland, P. R. and R. Kwok (2012), Wind-driven trends in Antarctic sea-ice drift, *Nature Geosci*, **5,** pp. 872–875, DOI: 10.1038/ngeo1627 (see pp. 83, 87, 94).

Hunke, E. C. and J. K. Dukowicz (1997), An Elastic–Viscous–Plastic Model for Sea Ice Dynamics, *Journal of Physical Oceanography*, **27,** pp. 1849–1867, DOI: 10.1175/1520-0485(1997)027<1849:AEVPMF>2.0.CO;2 (see p. 112).

Ito, T. and J. Marshall (2008), Control of Lower-Limb Overturning Circulation in the Southern Ocean by Diapycnal Mixing and Mesoscale Eddy Transfer, *J. Phys. Oceanogr.*, **38,** pp. 2832–2845 (see p. 15).

Ito, T., M. Woloszyn, and M. Mazloff (2010), Anthropogenic carbon dioxide transport in the Southern Ocean driven by Ekman flow, *Nature*, **463,** pp. 80–84, DOI: 10.1038/nature08687 (see pp. 25, 42).

Ito, T. and M. J. Follows (2003), Upper ocean control on the solubility pump of CO2, *Journal of marine research*, **61,** pp. 465–489, DOI: 10.1357/002224003322384898 (see pp. 8, 73).

Jacobs, S. S., C. F. Giulivi, and P. A. Mele (2002), Freshening of the Ross Sea During the Late 20th Century, *Science*, **297,** pp. 386–389, DOI: 10.1126/science.1069574 (see p. 90).

Jacobs, S. S. and C. F. Giulivi (2010), Large Multidecadal Salinity Trends near the Pacific–Antarctic Continental Margin, *Journal of Climate*, **23,** pp. 4508–4524 (see p. 90).

Johnson, G. and H. Bryden (1989), On the size of the Antarctic Circumpolar Current, *Deep Sea Research Part I: Oceanographic Research Papers*, **36,** pp. 39–53, DOI: 10.1016/0198-0149(89)90017-4 (see pp. 13, 14).

Johnson, G. C. (2008), Quantifying Antarctic Bottom Water and North Atlantic Deep Water volumes, *Journal of Geophysical Research: Oceans*, **113,** n/a–n/a, DOI: 10.1029/2007JC004477 (see p. 9).

Joughin, I., R. B. Alley, and D. M. Holland (2012), Ice-Sheet Response to Oceanic Forcing, *Science*, **338,** pp. 1172–1176, DOI: 10.1126/science.1226481, eprint: http://www.sciencemag.org/content/338/6111/1172.full.pdf (see pp. 87, 90, 95).

Kalnay, E., M. Kanamitsu, R. Kistler, W. Collins, D. Deaven, L. Gandin, M. Iredell, S. Saha, G. White, J. Woollen, Y. Zhu, A. Leetmaa, R. Reynolds, M. Chelliah, W. Ebisuzaki, W. Higgins, J. Janowiak, K. C. Mo, C. Ropelewski, J. Wang, R. Jenne, and D. Joseph (1996), The NCEP/NCAR 40-Year Reanalysis Project, *B. Am. Meteorol. Soc.*, **77,** pp. 437–471, DOI: 10.1175/1520-0477(1996)077<0437:TNYRP>2.0.CO;2 (see pp. 27, 37, 54).

Kanamitsu, M., W. Ebisuzaki, J. Woollen, S.-K. Yang, J. J. Hnilo, M. Fiorino, and G. L. Potter (2002), NCEP–DOE AMIP-II Reanalysis (R-2), *B. Am. Meteorol. Soc.*, **83,** pp. 1631–1643, DOI: 10.1175/BAMS-83-11-1631 (see p. 27).

Keeling, C., S. Piper, R. Bacastow, M. Wahlen, T. Whorf, M. Heimann, and H. Meijer (2005), *A history of atmospheric CO_2 and its effects on plants, animals and ecosystems*. In: ed. by J. Ehleringer, T. Cerling, and M. Dearing, New York: Springer, chap. 5, pp. 83–113 (see p. 6).

Khatiwala, S., T. Tanhua, S. Mikaloff Fletcher, M. Gerber, S. C. Doney, H. D. Graven, N. Gruber, G. A. McKinley, A. Murata, A. F. Ríos, C. L. Sabine, and J. L. Sarmiento (2012), Global ocean storage of anthropogenic carbon, *Biogeosciences Discussions*, **9,** pp. 8931–8988, DOI: 10.5194/bgd-9-8931-2012 (see pp. 7, 10).

Kidston, J. and E. Gerber (2010), Intermodel variability of the poleward shift of the austral jet stream in the CMIP3 integrations linked to biases in 20th century climatology, *Geophys. Res. Lett.*, **37,** DOI: 10.1029/2010GL042873 (see pp. 25, 50).

Kidston, J., S. M. Dean, J. A. Renwick, and G. K. Vallis (2010a), A robust increase in the eddy length scale in the simulation of future climates, *Geophys. Res. Lett.*, **37,** DOI: 10.1029/2009GL041615 (see p. 101).

Kidston, J., G. K. Vallis, S. M. Dean, and J. A. Renwick (2010b), Can the Increase in the Eddy Length Scale under Global Warming Cause the Poleward Shift of the Jet Streams?, *Journal of Climate*, **24,** pp. 3764–3780, DOI: 10.1175/2010JCLI3738.1 (see pp. 16, 101, 102).

King, M. A., R. J. Bingham, P. Moore, P. L. Whitehouse, M. J. Bentley, and G. A. Milne (2012), Lower satellite-gravimetry estimates of Antarctic sea-level contribution, *Nature*, **491,** pp. 586–589 (see pp. 87, 89).

Knorr, W. (2009), Is the airborne fraction of anthropogenic CO2 emissions increasing?, *Geophysical Research Letters*, **36,** n/a–n/a, DOI: 10.1029/2009GL040613 (see p. 7).

Knutti, R. and J. Sedláček (2012), Robustness and uncertainties in the new CMIP5 climate model projections, *Nature Climate Change*, DOI: 10.1038/nclimate1716 (see p. 19).

Kuhlbrodt, T., A. Griesel, M. Montoya, A. Levermann, M. Hofmann, and S. Rahmstorf (2007), On the driving processes of the Atlantic meridional overturning circulation, *Rev. Geophys.*, **45,** DOI: 10.1029/2004RG000166 (see p. 12).

Kushner, P., I. Held, and T. Delworth (2001), Southern Hemisphere Atmospheric Circulation Response to Global Warming, *J. Climate*, **14,** pp. 2238–2249, DOI: 10.1175/1520-0442(2001)014<0001:SHACRT>2.0.CO;2 (see pp. 39, 101).

Large, W. and S. Yeager (2009), The global climatology of an interannually varying air–sea flux data set, *Clim. Dynam.*, **33,** (2), pp. 341–364, DOI: 10.1007/s00382-008-0441-3 (see p. 37).

Le Quéré, C., C. Rödenbeck, E. T. Buitenhuis, T. J. Conway, R. Langenfelds, A. Gomez, C. Labuschagne, M. Ramonet, T. Nakazawa, N. Metzl, N. Gillett, and M. Heimann (2007), Saturation of the Southern Ocean CO_2 Sink Due to Recent Climate Change, *Science*, **316,** pp. 1735–1738, DOI: 10.1126/science.1136188 (see pp. 7, 11, 25, 33, 53, 77, 79–82).

Le Quéré, C., C. Rödenbeck, E. T. Buitenhuis, T. J. Conway, R. Langenfelds, A. Gomez, C. Labuschagne, M. Ramonet, T. Nakazawa, N. Metzl, N. P. Gillett, and M. Heimann (2008), Response to Comments on "Saturation of the Southern Ocean CO2 Sink Due to Recent Climate Change", *Science*, **319,** p. 570, DOI: 10.1126/science.1147315 (see p. 7).

Le Quéré, C., M. R. Raupach, J. G. Canadell, and G. Marland et al. (2009), Trends in the sources and sinks of carbon dioxide, *Nature Geoscience*, **2,** pp. 831–836, DOI: 10.1038/ngeo689 (see p. 7).

Le Quéré, C., T. Takahashi, E. T. Buitenhuis, C. Rödenbeck, and S. C. Sutherland (2010), Impact of climate change and variability on the global oceanic sink of CO2, *Global Biogeochemical Cycles*, **24,** n/a–n/a, DOI: 10.1029/2009GB003599 (see pp. 7, 11, 77, 80–82, 97).

Lefebvre, W. and H. Goosse (2008), An analysis of the atmospheric processes driving the large-scale winter sea ice variability in the Southern Ocean, *J. Geophys. Res.*, **113,** p. C02004, DOI: 10.1029/2006JC004032 (see p. 94).

Lin, J.-L. (2007), The Double-ITCZ Problem in IPCC AR4 Coupled GCMs: Ocean–Atmosphere Feedback Analysis, *Journal of Climate*, **20,** pp. 4497–4525, DOI: 10.1175/JCLI4272.1 (see p. 65).

Liu, J. and J. Curry (2010), Accelerated warming of the Southern Ocean and its impacts on the hydrological cycle and sea ice, *Proceedings of the National Academy of Sciences*, **107,** pp. 14987–14992, DOI: 10.1073/pnas.1003336107 (see p. 87).

Liu, J., J. Curry, and D. Martinson (2004), Interpretation of recent Antarctic sea ice variability, *Geophysical Research Letters*, **31,** p. L02205, DOI: 10.1029/2003GL018732 (see p. 94).

Lovenduski, N. S., N. Gruber, S. C. Doney, and I. D. Lima (2007), Enhanced CO_2 outgassing in the Southern Ocean from a positive phase of the Southern Annular Mode, *Global Biogeochemical Cycles*, **21,** n/a–n/a, DOI: 10.1029/2006GB002900 (see pp. 53, 82).

Lovenduski, N. S., N. Gruber, and S. C. Doney (2008), Toward a mechanistic understanding of the decadal trends in the Southern Ocean carbon sink, *Global Biogeochemical Cycles*, **22,** n/a–n/a, DOI: 10.1029/2007GB003139 (see pp. 7, 11, 53, 77, 79–82, 97).

Lüthi, D., M. Le Floch, B. Bereiter, T. Blunier, J. Barnola, U. Siegenthaler, D. Raynaud, J. Jouzel, H. Fischer, K. Kawamura, *et al.* (2008), High-resolution carbon dioxide concentration record 650,000–800,000 years before present, *Nature*, **453,** pp. 379–382, DOI: 10.1038/nature06949 (see p. 6).

Marinov, I. and J. L. Sarmiento (2004), *The ocean carbon cycle and climate*. In: ed. by M. Follows and T. Oguz, vol. 40, NATO Science Series, Kluwer, chap. THE ROLE OF THE OCEANS IN THE GLOBAL CARBON CYCLE: AN OVERVIEW (see pp. 8–11, 104).

Marinov, I., A. Gnanadesikan, J. Toggweiler, and J. Sarmiento (2006), The Southern Ocean biogeochemical divide, *Nature*, **441,** pp. 964–967, DOI: 10.1038/nature04883 (see p. 8).

Marinov, I., A. Gnanadesikan, J. L. Sarmiento, J. R. Toggweiler, M. Follows, and B. K. Mignone (2008), Impact of oceanic circulation on biological carbon storage in the ocean and atmospheric pCO2, *Global Biogeochemical Cycles*, **22,** n/a–n/a, DOI: 10.1029/2007GB002958 (see pp. 8, 9).

Marshall, G. J. (2003), Trends in the Southern Annular Mode from Observations and Reanalyses, *J. Climate*, **16,** pp. 4134–4143, DOI: 10.1175/1520-0442(2003)016<4134:TITSAM>2.0.CO;2 (see pp. 25–27).

Marshall, J. and T. Radko (2003), Residual-mean solutions for the Antarctic Circumpolar Current and its associated overturning circulation, *J. Phys. Oceanogr.*, **33,** pp. 2341–2354, DOI: 10.1175/1520-0485(2003)033<2341:RSFTAC>2.0.CO;2 (see pp. 13, 14, 100).

Marshall, J. and K. Speer (2012), Closure of the meridional overturning circulation through Southern Ocean upwelling, *Nature Geosci*, **5,** pp. 171–180, DOI: 10.1038/ngeo1391 (see pp. 12, 25).

Matthews, H., A. Weaver, K. Meissner, N. Gillett, and M Eby (2004), Natural and anthropogenic climate change: incorporating historical land cover change, vegeta-

tion dynamics and the global carbon cycle, *Climate Dynamics*, **22,** pp. 461–479, DOI: 10.1007/s00382-004-0392- (see p. 114).

McAvaney, B., C Covey, S Joussaume, V Kattsov, A Kitoh, W Ogana, A. Pitman, A. Weaver, R. Wood, Z. Zhao, *et al.* (2001), *Climate change 2001: the scientific basis*. In: Cambridge University Press, Cambridge, United Kingdom and New York, NY, USA, chap. Model evaluation, pp. 471–521 (see p. 18).

Meehl, G. A., T. Stocker, W. Collins, P. Friedlingstein, A. Gaye, J. Gregory, A Kitoh, R. Knutti, J. Murphy, A. Nda, S. Raper, I. Watterson, A. Weaver, and Z. Zhoa (2007a), *IPCC Climate Change 2007: The Physical Science Basis*. In: ed. by S. Solomon *et al.*, Cambridge University Press, pp. 747–845 (see pp. 7, 46).

Meehl, G. A., C. Covey, T. Delworth, M. Latif, B. McAvaney, J. F. B. Mitchell, R. J. Stouffer, and K. E. Taylor (2007b), The WCRP CMIP3 multi-model dataset: A new era in climate change research, *B. Am. Meteorol. Soc.*, **88,** pp. 1383–1394 (see pp. 18, 37, 39).

Meinshausen, M., S. J. Smith, K. Calvin, J. S. Daniel, M. L. T. Kainuma, J.-F. Lamarque, K. Matsumoto, S. A. Montzka, S. C. B. Raper, K. Riahi, A. Thomson, G. J. M. Velders, and D. P. P. Vuuren (2011), The RCP greenhouse gas concentrations and their extensions from 1765 to 2300, *Climatic Change*, **109,** pp. 213–241, DOI: 10.1007/s10584-011-0156-z (see pp. 73, 89).

Meissner, K. J., A. J. Weaver, H. D. Matthews, and P. M. Cox (2003-12-01), The role of land surface dynamics in glacial inception: a study with the UVic Earth System Model, *Clim. Dynam.*, **21,** pp. 515–537, DOI: 10.1007/s00382-003-0352-2 (see p. 114).

Meissner, K. J., M. Eby, A. J. Weaver, and O. A. Saenko (2008), CO2 threshold for millennial-scale oscillations in the climate system: implications for global warming scenarios, *Clim. Dynam.*, **30,** pp. 161–174, DOI: 10.1007/s00382-007-0279-0 (see p. 66).

Meredith, M. P., A. C. Naveira Garabato, A. M. Hogg, and R. Farneti (2011), Sensitivity of the Overturning Circulation in the Southern Ocean to Decadal Changes in Wind Forcing, *Journal of Climate*, **25,** pp. 99–110, DOI: 10.1175/2011JCLI4204.1 (see pp. 37, 48, 50).

Munk, W. and C. Wunsch (1998), Abyssal recipes II: energetics of tidal and wind mixing, *Deep-Sea Research Part I*, **45,** pp. 1977–2010, DOI: 10.1016/S0967-0637(98)00070-3 (see p. 12).

Munk, W. H. (1966), "Abyssal recipes", in: *Deep Sea Research and Oceanographic Abstracts*, vol. 13, 4, Elsevier, pp. 707–730, DOI: 10.1016/0011-7471(66)90602-4 (see p. 12).

Nikurashin, M. and G. Vallis (2011), A Theory of Deep Stratification and Overturning Circulation in the Ocean, *Journal of Physical Oceanography*, **41,** pp. 485–502, DOI: 10.1175/2010JPO4529.1 (see pp. 11, 15, 99).

— (2012), A Theory of the Interhemispheric Meridional Overturning Circulation and Associated Stratification, *Journal of Physical Oceanography*, **42,** pp. 1652–1667, DOI: 10.1175/JPO-D-11-0189.1 (see pp. 9, 13, 14, 17).

Nikurashin, M., G. K. Vallis, and A. Adcroft (2013), Routes to energy dissipation for geostrophic flows in the Southern Ocean, *Nature Geosci*, **6,** pp. 48–51, DOI: 10.1038/ngeo1657 (see p. 15).

Oeschger, H., U. Siegenthaler, U. Schotterer, and A. Gugelmann (1975), A box diffusion model to study the carbon dioxide exchange in nature, *Tellus*, **27,** pp. 168–192, DOI: 10.1111/j.2153-3490.1975.tb01671.x (see p. 104).

Pacanowski, R. (1995), *MOM 2 documentation, user's guide and reference manual.* GFDL Ocean group Tech. Rep. 3, NOAA/GFDL (see pp. 111, 112).

Peeters, F., R. Acheson, G. Brummer, W. de Ruijter, R. Schneider, G. Ganssen, E. Ufkes, and D. Kroon (2004), Vigorous exchange between the Indian and Atlantic oceans at the end of the past five glacial periods, *Nature*, **430,** pp. 661–665, DOI: 10.1038/nature02785 (see p. 43).

Petit, J., J. Jouzel, D. Raynaud, N. Barkov, J. Barnola, I. Basile, M. Bender, J. Chappellaz, M. Davis, G. Delaygue, M. Delmotte, V. Kotlyakov, M. Legrand, V. Lipenkov, C. Lorius, L. Pépin, C. Ritz, E. Saltzman, and M. Stievenard (1999), Climate and atmospheric history of the past 420, 000 years from the Vostok ice core, Antarctica, *Nature*, **399,** pp. 429–436, DOI: 10.1038/20859 (see p. 6).

Pritchard, H. D., S. R. M. Ligtenberg, H. A. Fricker, D. G. Vaughan, M. R. van den Broeke, and L. Padman (2012), Antarctic ice-sheet loss driven by basal melting of ice shelves, *Nature*, **484,** pp. 502–505, DOI: 10.1038/nature10968 (see pp. 87, 90).

Purkey, S. and G. Johnson (2013), Antarctic Bottom Water warming and freshening: Contributions to sea level ruse, ocean frshwater budgets and global heat gain, *J. Climate*, DOI: 10.1175/JCLI-D-12-00834.1 (see p. 90).

Raven, J. e. a. (2005), *Ocean acidification due to increasing atmospheric carbon dioxide*, Policy Document 12/05, The Royal Society (see p. 105).

Raven, J. and P. Falkowski (1999), Oceanic sinks for atmospheric CO_2, *Plant, Cell and Environment*, **22,** pp. 741–755 (see p. 7).

Rignot, E., I. Velicogna, M. R. van den Broeke, A. Monaghan, and J. Lenaerts (2011), Acceleration of the contribution of the Greenland and Antarctic ice sheets to sea level rise, *Geophys. Res. Lett.*, **38,** DOI: 10.1029/2011GL046583 (see pp. 87, 89, 90).

Rignot, E., J. L. Bamber, M. R. van den Broeke, C. Davis, Y. Li, W. J. van de Berg, and E. van Meijgaard (2008), Recent Antarctic ice mass loss from radar interferometry and regional climate modelling, *Nature Geosci*, **1,** pp. 106–110, DOI: 10.1038/ngeo102 (see pp. 89, 95).

Rintoul, S. R., C. Hughes, and D. Olbers (2001), *Ocean Circulation and Climate*. In: ed. by G. Siedler, J. Chruch, and J. Gould, Academic Press, chap. The Antarctic Circumpolar Current System (see p. 8).

Rintoul, S. R. (2007), Rapid freshening of Antarctic Bottom Water formed in the Indian and Pacific oceans, *Geophys. Res. Lett.*, **34,** DOI: 10.1029/2006GL028550 (see p. 90).

Rogner, H.-H., R. F. Aguilera, R. Bertani, S. C. Bhattacharya, M. B. Dusseault, L. Gagnon, H. Haberl, M. Hoogwijk, A. Johnson, M. L. Rogner, H. Wagner, and V. Yakushev (2012), *Chapter 7 - Energy Resources and Potentials*. In: *Global Energy Assessment - Toward a Sustainable Future*, Cambridge University Press, Cambridge, UK, New York, NY, USA, and the International Institute for Applied Systems Analysis, Laxenburg, Austria, pp. 423–512 (see p. 6).

Royer, D., R. Berner, I. Montañez, N. Tabor, and D. Beerling (2004), CO_2 as a primary driver of Phanerozoic climate, *GSA Today*, **14,** pp. 4–10, DOI: 10.1130/1052-5173(2004)014<4:CAAPDO>2.0.CO;2. (see p. 6).

Russell, J., R. J. Stouffer, and K. Dixon (2006a), Intercomparison of the Southern Ocean Circulations in IPCC Coupled Model Control Simulations, *J. Climate*, **19,** pp. 4560–4575, DOI: 10.1175/JCLI3869.1 (see pp. 25, 37).

Russell, J., K. Dixon, A. Gnanadesikan, R. Stouffer, and J. Toggweiler (2006b), The Southern Hemisphere Westerlies in a warming world: Propping open the door to the deep ocean, *J. Climate*, **19,** pp. 6382–6390, DOI: 10.1175/JCLI3984.1 (see pp. 9, 25, 37).

Sabine, C. L., R. A. Feely, N. Gruber, R. M. Key, K. Lee, J. L. Bullister, R. Wanninkhof, C. S. Wong, D. W. R. Wallace, B. Tilbrook, F. J. Millero, T.-H. Peng,

A. Kozyr, T. Ono, and A. F. Rios (2004), The Oceanic Sink for Anthropogenic CO_2, *Science*, **305,** pp. 367–371, DOI: 10.1126/science.1097403 (see pp. 7, 10).

Saenko, O. (2012), *On 2D(x,y) structure of mesoscale eddy diffusivity in the ocean*, tech. rep., Canadian Centre for Climate Modelling and Analysis, p. 4 (see pp. 60, 89).

Sagan, C. and G. Mullen (1972), Earth and Mars: Evolution of Atmospheres and Surface Temperatures, *Science*, **177,** pp. 52–56, DOI: 10.1126/science.177.4043.52, eprint: http://www.sciencemag.org/content/177/4043/52.full.pdf (see p. 6).

Santer, B. D., R. Sausen, T. M. L. Wigley, J. S. Boyle, K. AchutaRao, C. Doutriaux, J. E. Hansen, G. A. Meehl, E. Roeckner, R. Ruedy, G. Schmidt, and K. E. Taylor (2003), Behavior of tropopause height and atmospheric temperature in models, reanalyses, and observations: Decadal changes, *J. Geophysical Research-atmospheres*, **108,** p. 4002, DOI: 10.1029/2002JD002258 (see p. 101).

Santer, B., T. Wigley, J. Boyle, D. Gaffen, J. Hnilo, D. Nychka, D. Parker, and K. E. Taylor (2000), Statistical significance of trends and trend differences in layer-average atmospheric temperature time series, *J. Geophys. Res.*, **105,** pp. 7337–7356, DOI: 10.1029/1999JD901105 (see p. 28).

Sarmiento, J. L. and N. Gruber (2006), *Ocean Biogeochemical Dynamics*, Princeton University Press, New Jersey (see pp. 7, 8, 10, 19, 20, 22, 104, 106).

Sarmiento, J., M Gloor, N Gruber, C Beaulieu, A. Jacobson, S. Fletcher, S Pacala, and K Rodgers (2010), Trends and regional distributions of land and ocean carbon sinks, *Biogeosciences*, **7,** pp. 2351–2367, DOI: 10.5194/bg-7-2351-2010 (see pp. 2, 7, 77).

Schmittner, A., A. Oschlies, X. Giraud, M. Eby, and H. L. Simmons (2005), A global model of the marine ecosystem for long-term simulations: Sensitivity to ocean mixing, buoyancy forcing, particle sinking, and dissolved organic matter cycling, *Global Biogeochem. Cycles*, **19,** DOI: 10.1029/2004GB002283 (see pp. 112, 113).

Schmittner, A., A. Oschlies, H. D. Matthews, and E. D. Galbraith (2008), Future changes in climate, ocean circulation, ecosystems, and biogeochemical cycling simulated for a business-as-usual CO2 emission scenario until year 4000 AD, *Global Biogeochemical Cycles*, **22,** n/a–n/a, DOI: 10.1029/2007GB002953 (see pp. 113, 114).

Semtner, A. (1976), A Model for the Thermodynamic Growth of Sea Ice in Numerical Investigations of Climate, *Journal of Physical Oceanography*, **6,** pp. 379–389, DOI: 10.1175/1520-0485(1976)006<0379:AMFTTG>2.0.CO;2 (see p. 112).

Shakun, J. D., P. U. Clark, F. He, S. A. Marcott, A. C. Mix, Z. Liu, B. Otto-Bliesner, A. Schmittner, and E. Bard (2012), Global warming preceded by increasing carbon dioxide concentrations during the last deglaciation, *Nature*, **484,** pp. 49–54, DOI: 10.1038/nature10915 (see p. 6).

Shepherd, A., E. R. Ivins, G. A, V. R. Barletta, M. J. Bentley, S. Bettadpur, K. H. Briggs, D. H. Bromwich, R. Forsberg, N. Galin, M. Horwath, S. Jacobs, I. Joughin, M. A. King, J. T. M. Lenaerts, J. Li, S. R. M. Ligtenberg, A. Luckman, S. B. Luthcke, M. McMillan, R. Meister, G. Milne, J. Mouginot, A. Muir, J. P. Nicolas, J. Paden, A. J. Payne, H. Pritchard, E. Rignot, H. Rott, L. S. Sørensen, T. A. Scambos, B. Scheuchl, E. J. O. Schrama, B. Smith, A. V. Sundal, J. H. van Angelen, W. J. van de Berg, M. R. van den Broeke, D. G. Vaughan, I. Velicogna, J. Wahr, P. L. Whitehouse, D. J. Wingham, D. Yi, D. Young, and H. J. Zwally (2012), A Reconciled Estimate of Ice-Sheet Mass Balance, *Science*, **338,** pp. 1183–1189, DOI: 10.1126/science.1228102 (see pp. 87, 89, 90, 94).

Siegenthaler, U. and J. Sarmiento (1993), Atmospheric carbon dioxide and the ocean, *Nature*, **365,** pp. 119–125, DOI: 10.1038/365119a0 (see p. 6).

Sigman, D. M., M. P. Hain, and G. H. Haug (2010), The polar ocean and glacial cycles in atmospheric CO2 concentration, *Nature*, **466,** pp. 47–55, DOI: 10.1038/nature09149 (see pp. 8, 9).

Sigmond, M. and J. C. Fyfe (2010), Has the ozone hole contributed to increased Antarctic sea ice extent?, *Geophysical Research Letters*, **37,** n/a–n/a, DOI: 10.1029/2010GL044301 (see p. 87).

Sijp, W. and M. England (2008), The effect of a northward shift in the Southern Hemisphere westerlies on the global ocean, *Prog. Oceanogr.*, **79,** pp. 1–19, DOI: 10.1016/j.pocean.2008.07.002 (see p. 45).

— (2009), Southern Hemisphere westerly wind control over the ocean's thermohaline circulation, *J. Climate*, **22,** pp. 1277–1286, DOI: 10.1175/2008JCLI2310.1 (see p. 45).

Silva, T. A. M., G. R. Bigg, and K. W. Nicholls (2006), Contribution of giant icebergs to the Southern Ocean freshwater flux, *Journal of Geophysical Research: Oceans*, **111,** n/a–n/a, DOI: 10.1029/2004JC002843 (see p. 95).

Simpkins, G., L. Ciasto, D. Thompson, and M. England (2012), Seasonal Relationships between Large-Scale Climate Variability and Antarctic Sea Ice Concentration, *Journal of Climate*, **25,** pp. 5451–5469, DOI: 10.1175/JCLI-D-11-00367.1 (see p. 94).

Sloyan, B. M. and S. R. Rintoul (2001), The Southern Ocean Limb of the Global Deep Overturning Circulation, *Journal of Physical Oceanography*, **31,** pp. 143–173, DOI: 10.1175/1520-0485(2001)031<0143:TSOLOT>2.0.CO;2 (see p. 9).

Solomon, S., D. Qin, M. Manning, R. Alley, T. Berntsen, N. Bindoff, Z. Chen, A. Chidthaisong, J. Gregory, G. Hegerl, M. Heimann, B. Hewitson, B. Hoskins, F. Joos, J. Jouzel, V. Kattsov, U. Lohmann, T. Matsuno, M. Molina, N. Nicholls, J. Overpeck, G. Raga, V. Ramaswamy, J. Ren, M. Rusticucci, R. Somerville, T. Stocker, P. Whetton, R. Wood, and D. Wratt (2007), *Climate Change 2007: The Physical Science Basis. Contribution of Working Group I to the Fourth Assessment Report of the Intergovernmental Panel on Climate Change*. In: ed. by D Solomon S. and. Qin, M. Manning, Z. Chen, M. Marquis, K. Averyt, M. Tignor, and H. Miller, Cambridge and New York: Cambridge University Press, chap. Technical Summary (see p. 6).

Son, S.-W., E. P. Gerber, J. Perlwitz, L. M. Polvani, N. P. Gillett, K.-H. Seo, V. Eyring, T. G. Shepherd, D. Waugh, H. Akiyoshi, J. Austin, A. Baumgaertner, S. Bekki, P. Braesicke, C. Brühl, N. Butchart, M. P. Chipperfield, D. Cugnet, M. Dameris, S. Dhomse, S. Frith, H. Garny, R. Garcia, S. C. Hardiman, P. Jöckel, J. F. Lamarque, E. Mancini, M. Marchand, M. Michou, T. Nakamura, O. Morgenstern, G. Pitari, D. A. Plummer, J. Pyle, E. Rozanov, J. F. Scinocca, K. Shibata, D. Smale, H. Teyssèdre, W. Tian, and Y. Yamashita (2010), Impact of stratospheric ozone on Southern Hemisphere circulation change: A multimodel assessment, *Journal of Geophysical Research: Atmospheres*, **115,** n/a–n/a, DOI: 10.1029/2010JD014271 (see pp. 33, 35, 56, 102).

Spence, P., O. Saenko, M. Eby, and A. Weaver (2009), The Southern Ocean overturning: Parameterized versus permitted eddies, *J. Phys. Oceanogr.*, **39,** pp. 1634–1651, DOI: 10.1175/2009JPO4120.1 (see pp. 60, 100).

Spence, P., J. Fyfe, A. Montenegro, and A. Weaver (2010), Southern Ocean response to strengthening winds in an eddy-permitting global ocean model, *J. Climate*, **23,** DOI: 10.1175/2010JCLI3098.1 (see p. 60).

Stanley, G. and O. Saenko (2013), Bottom-enhanced diapycnal mixing driven by mesoscale eddies: sensitivity to wind energy supply, *J. Phys. Oceanogr.*, **(submitted),** (see p. 15).

Stephens, B. B. and R. F. Keeling (2000), The influence of Antarctic sea ice on glacial-interglacial CO_2 variations, *Nature*, **404,** pp. 171–174, DOI: 10.1038/35004556 (see p. 8).

Stommel, H. (1958), The abyssal circulation, *Deep Sea Research Part II: Topical Studies in Oceanography*, **5,** pp. 80–82, DOI: 10.1016/S0146-6291(58)80014-4 (see p. 12).

Stommel, H. and A. B. Arons (1960), On the abyssal circulation of the world ocean—II. An idealized model of the circulation pattern and amplitude in oceanic basins, *Deep Sea Research (1953)*, **6,** pp. 217–233, DOI: 10.1016/0146-6313(59)90075-9 (see p. 12).

Stouffer, R. J., D. Seidov, and B. J. Haupt (2007), Climate Response to External Sources of Freshwater: North Atlantic versus the Southern Ocean, *Journal of Climate*, **20,** pp. 436–448, DOI: 10.1175/JCLI4015.1 (see pp. 87, 90).

Stroeve, J. (2003), *Sea Ice Trends and Climatologies from SMMR and SSM/I-SSMIS. [NASA TEAM monthly area]*, tech. rep., Boulder, Colorado USA: National Snow and Ice Data Center (see p. 89).

Swart, N. C. and J. C. Fyfe (2012a), Observed and simulated changes in the Southern Hemisphere surface westerly wind-stress, *Geophys. Res. Lett.*, **39,** DOI: 10.1029/2012GL052810 (see p. 24).

— (2012b), Ocean carbon uptake and storage influenced by wind bias in global climate models, *Nature Clim. Change*, **2,** pp. 47–52, DOI: 10.1038/nclimate1289 (see pp. 25, 36).

— (2013), The influence of recent Antarctic ice-sheet retreat on sea-ice area trends, *Geophys. Res. Lett.*, (submitted) (see p. 86).

Swart, N. C. and A. J. Weaver (2012), The Alberta oil sands and climate, *Nature Climate Change*, DOI: 10.1038/nclimate1421 (see p. 6).

Swingedouw, D., T. Fichefet, P. Huybrechts, H. Goosse, E. Driesschaert, and M. F. Loutre (2008), Antarctic ice-sheet melting provides negative feedbacks on future climate warming, *Geophys. Res. Lett.*, **35,** DOI: 10.1029/2008GL034410 (see p. 87).

Taylor, K. E., R. J. Stouffer, and G. A. Meehl (2011), An Overview of CMIP5 and the Experiment Design, *Bulletin of the American Meteorological Society*, **93,** pp. 485–498, DOI: 10.1175/BAMS-D-11-00094.1 (see pp. 18, 89).

Toggweiler, J. R. and B. Samuels (1995), Effect of drake passage on the global thermohaline circulation, *Deep Sea Res. PT I*, **42,** pp. 477 –500, DOI: DOI:10.1016/0967-0637(95)00012-U (see p. 13).

Toggweiler, J., J. Russell, and S. Carson (2006), Midlatitude westerlies, atmospheric CO_2, and climate change during the ice ages, *Paleoceanography*, **21,** (see p. 9).

Trenberth, K. (2010), More knowledge, less certainty, *Nature Reports Climate Change*, pp. 20–21, DOI: 10.1038/climate.2010.06 (see p. 19).

Turner, J., J. C. Comiso, G. J. Marshall, T. A. Lachlan;Cope, T. Bracegirdle, T. Maksym, M. P. Meredith, Z. Wang, and A. Orr (2009–), Non-annular atmospheric circulation change induced by stratospheric ozone depletion and its role in the recent increase of Antarctic sea ice extent, *Geophys. Res. Lett.*, **36,** DOI: 10.1029/2009GL037524 (see p. 87).

Turner, J., T. Bracegirdle, T. Phillips, G. J. Marshall, and J. S. Hosking (2012), An Initial Assessment of Antarctic Sea Ice Extent in the CMIP5 Models, *Journal of Climate*, DOI: 10.1175/JCLI-D-12-00068.1 (see p. 92).

Uppala, S. M., P. W. KÅllberg, A. J. Simmons, U. Andrae, V. D. C. Bechtold, M. Fiorino, J. K. Gibson, J. Haseler, A. Hernandez, G. A. Kelly, X. Li, K. Onogi, S. Saarinen, N. Sokka, R. P. Allan, E. Andersson, K. Arpe, M. A. Balmaseda, A. C. M. Beljaars, L. V. D. Berg, J. Bidlot, N. Bormann, S. Caires, F. Chevallier, A. Dethof, M. Dragosavac, M. Fisher, M. Fuentes, S. Hagemann, E. Hólm, B. J. Hoskins, L. Isaksen, P. A. E. M. Janssen, R. Jenne, A. P. Mcnally, J.-F. Mahfouf, J.-J. Morcrette, N. A. Rayner, R. W. Saunders, P. Simon, A. Sterl, K. E. Trenberth, A. Untch, D. Vasiljevic, P. Viterbo, and J. Woollen (2005), The ERA-40 re-analysis, *Q. J. Roy. Meteor. Soc.*, **131,** pp. 2961–3012, DOI: 10.1256/qj.04.176 (see p. 37).

Vallis, G. (2006), *Atmospheric and oceanic fluid dynamics*, Cambridge, U.K.: Cambridge University Press, p. 745 (see pp. 11, 12, 14, 16, 99, 101).

Walker, J. C. G., P. B. Hays, and J. F. Kasting (1981), A NEGATIVE FEEDBACK MECHANISM FOR THE LONG-TERM STABILIZATION OF EARTH'S SURFACE TEMPERATURE, *J. Geophys. Res.*, **86,** pp. 9776–9782, DOI: 10.1029/JC086iC10p09776 (see p. 6).

Wang, X. L., V. R. Swail, and F. W. Zwiers (2006), Climatology and Changes of Extratropical Cyclone Activity: Comparison of ERA-40 with NCEP–NCAR Reanalysis for 1958–2001, *Journal of Climate*, **19,** pp. 3145–3166, DOI: 10.1175/JCLI3781.1 (see p. 80).

Weaver, A., M. Eby, C. Wiebe, M. Bitz, C. Duffy, E. T.L., A. Fanning, H. M.M., A. MacFadyen, H. Matthews, K. Meissner, S. O.A., A. Schmittner, H. Wang, and M. Yoshimori (2001), The UVic Earth System Climate Model: Model Description, Climatology, and Applications to Past, Present and Future Climates, *Atmos. Ocean*, **39,** pp. 1–68, DOI: 10.1080/07055900.2001.9649686 (see pp. 39, 59, 89, 95, 111, 112, 114).

Weber, S. L., S. S. Drijfhout, A. Abe-Ouchi, M. Crucifix, M. Eby, A. Ganopolski, S. Murakami, B. Otto-Bliesner, and W. R. Peltier (2007), The modern and glacial overturning circulation in the Atlantic ocean in PMIP coupled model simulations, *Clim. Past*, **3,** pp. 51–64, DOI: 10.5194/cp-3-51-2007 (see p. 114).

Weijer, W., W. de Ruijter, H. Dijkstra, and P. van Leeuwen (1999), Impact of Interbasin Exchange on the Atlantic Overturning Circulation, *J. Phys. Oceanogr.*, **29,** pp. 2266–2284, DOI: 10.1175/1520-0485(1999)029<2266:IOIEOT>2.0.CO;2 (see p. 45).

Wetzel, P., A. Winguth, and E. Maier-Reimer (2005), Sea-to-air CO2 flux from 1948 to 2003: A model study, *Global Biogeochemical Cycles*, **19,** n/a–n/a, DOI: 10.1029/2004GB002339 (see p. 7).

Wolfe, C. L. and P. Cessi (2010), What Sets the Strength of the Middepth Stratification and Overturning Circulation in Eddying Ocean Models?, *Journal of Physical Oceanography*, **40,** pp. 1520–1538, DOI: 10.1175/2010JPO4393.1 (see pp. 14, 15, 17).

Wu, L., W. Cai, L. Zhang, H. Nakamura, A. Timmermann, T. Joyce, M. J. McPhaden, M. Alexander, B. Qiu, M. Visbeck, P. Chang, and B. Giese (2012), Enhanced warming over the global subtropical western boundary currents, *Nature Clim. Change*, **2,** pp. 161–166, DOI: 10.1038/nclimate1353 (see p. 33).

Yang, X.-Y., R. X. Huang, and D. X. Wang (2007), Decadal Changes of Wind Stress over the Southern Ocean Associated with Antarctic Ozone Depletion, *Journal of Climate*, **20,** pp. 3395–3410, DOI: 10.1175/JCLI4195.1 (see pp. 32, 56, 108).

Zhang, J. (2007), Increasing Antarctic sea ice under warming atmospheric and oceanic conditions, *Journal of Climate*, **20,** pp. 2515–2529, DOI: 10.1175/JCLI4136.1 (see p. 87).

Zickfeld, K., J. Fyfe, O. Saenko, M. Eby, and A. Weaver (2007), Response of the global carbon cycle to human-induced changes in Southern Hemisphere winds, *Geophys. Res. Lett.*, **34,** DOI: 10.1029/2006GL028797 (see pp. 25, 35, 46, 50, 53).

Zickfeld, K., J. Fyfe, M. Eby, and A. Weaver (2008), Comment on "Saturation of the Southern Ocean CO_2 Sink Due to Recent Climate Change", *Science*, **319,** DOI: 10.1126/science.1146886 (see pp. 7, 33, 53).